Assessing the performances and optimizing the radar sounder design parameters for the EJSM mission (Ganymede and Europa)

Yann Berquin

UNIVERSITÉ DE GRENOBLE

THÈSE

Pour obtenir le grade de

DOCTEUR DE L'UNIVERSITÉ DE GRENOBLE

Spécialité : **Terre, Univers, Environnement**

Arrêté ministériel : 7 août 2006

Présentée par

Yann Berquin

Thèse dirigée par **Wlodek Kofman**

préparée au sein de **l'Institut de Planétologie et d'Astrophysique de Grenoble**
et de **l'école doctorale Terre, Univers, Environnement**

Assessing the performance and optimizing the radar sounder design parameters for the JUICE mission

Thèse soutenue publiquement le **27 février 2014**,
devant le jury composé de :

Pr., Jean-Louis Monin
Président de l'Institut de Planétologie et d'Astrophysique de Grenoble, Président

Pr. Jean-Pierre Barriot
Directeur du laboratoire GEPASUD, Directeur de l'Observatoire Géodésique de Tahiti, Rapporteur

Dr., Amélie Litman
Maître de Conférence, Insitut Fresnel, Rapporteur

Dr., Roberto Orosei
Istituto di Radioastronomia Istituto Nazionale di Astrofisica, Examinateur

Dr., Essam Heggy
Jet Propulsion Laboratory, Examinateur

Dr., Wlodek Kofman
Directeur de Recherche Emérite, Institut de Planétologie et d'Astrophysique de Grenoble, Directeur de thèse

Dr., Alain Hérique
Maître de Conférence, Institut de Planétologie et d'Astrophysique de Grenoble, Examinateur

ASSESSING THE PERFORMANCES AND OPTIMIZING THE RADAR SOUNDER DESIGN PARAMETERS FOR THE JUICE MISSION

YANN BERQUIN

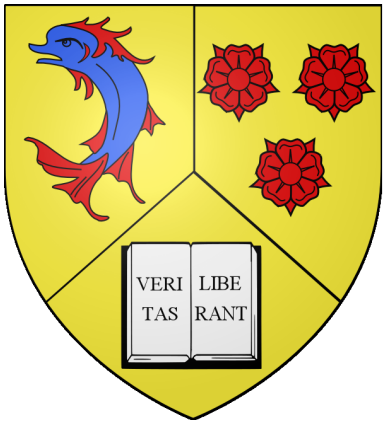

In Partial Fulfilment of the Requirements for the Degree of
Doctor of Philosophy

A Dissertation Submitted to the
Ecole Doctorale Terre Univers Environnement
Université de Grenoble

ABSTRACT

The manuscript details the work performed in the course of my PhD on planetary sounding radar. The main goal of the study is to help designing and assessing the sounding radar performances. This instrument will be embarked on the European Space Agency (ESA)'s large class mission JUpiter ICy moons Explorer (JUICE) to probe Jupiter's environment and Jupiter's icy moons Callisto, Ganymede and Europa. As an introduction to the problem, a study on Ganymede's surface Digital Elevation Model (DEM) and its implications with regard to the radar performances was performed. The results of this work put forward issues due to a hostile environment with important surface clutter which eventually lead to a decrease in the radar signal bandwidth to 8–10 MHz. A first section is then dedicated to the formulation of the direct problem of sounding radar with a focus on surface formulations. This section eventually leads to a novel algorithm for radar surface echo computation from meshed surfaces which proves to be both efficient and accurate. A second section studies the possibility to use surface formulation to recover geophysical surface parameters from sounding radar data. For that purpose, three main approaches are discussed namely (i) a linear approach, (ii) a gradient-based approach and (iii) a statistical approach. These techniques rely on a probabilistic view of the inverse problem at hand and yield good result with different setups. Although we mainly focus on surface reflectivity, we also discuss surface topography inversion. Finally, a last section discusses the work presented in the manuscript and provides perspectives for future work.

Le manuscrit détail des travaux portant sur les performances du radar sondeur planétaire. Ces études ont été conduites dans le cadre de ma thèse qui vise au dimensionnement et à l'évaluation des performances du radar sondeur de la mission JUICE de l'ESA. Dans un premier temps (c.f. section 2), une étude des jeux de données topographiques a été conduite sur la lune glacée de Jupiter Ganymède. Les résultats de cette étude ont fait l'objet d'un article qui met en évidence des conditions particulièrement hostiles au sondage radar, notamment à cause de terrains fortement accidentés. Cette étude a notamment conduit à une reévaluation des caractéristiques du radar sondeur avec une bande en fréquence du signal abaissée à 8–10 MHz. Reprenant les travaux menés dans l'équipe quelques années plus tôt (c.f. [Nouvel et al., 2004]), je me suis attaché par la suite à réimplémenter et à améliorer un algorithme performant pour simuler les échos de surface en y apportant des améliorations conséquentes (c.f. section 4).

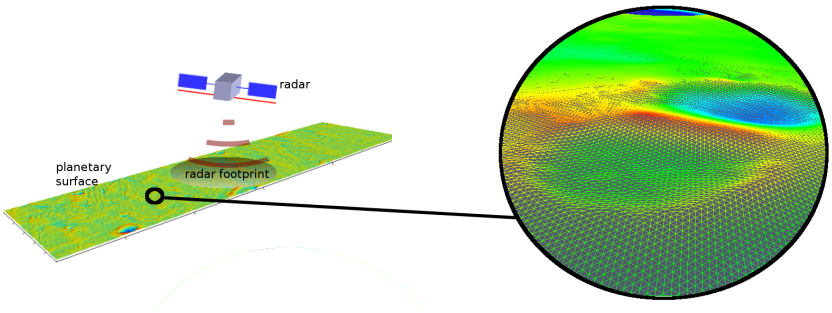

Figure 1: Schéma du principe du sondage radar planétaire monostatique. Une antenne dipolaire située sur le satellite en orbite émet un signal électromagnétique vers l'objet planétaire. Cette même antenne enregistre ensuite les signaux électromagnétiques diffusés et réfléchis par les milieux planétaires (échos de surfaces et de sous-sol). Le maillage utilisé pour la simulation de surface est mis en évidence sur le schéma. Ce maillage forme un réseau de facettes triangulaires. L'échelle des couleurs indique la topographie de la surface.

L'algorithme repose sur le principe de Huygens-Fresnel. La surface planétaire est alors décrite comme un maillage composés de facettes triangulaires. La forme analytique des champs électromagnétiques pour une facette triangulaire quelconque est dérivée en utilisant un développement limité de la fonction de phase (c.f. section 4). Le but recherché à l'origine est de modéliser à moindre coût les échos radar résultant de l'interface atmosphère/ sous-sol qui composent la majeure partie des signaux reçus lors des campagnes de sondage planétaire (c.f. figure 2). Le code offre des perpsectives intéressantes en permettant de reproduire les signaux des instruments radar en configuration monostatique ou bistatique.
Ce travail permet également de mieux apprécier l'intéret d'une formulation surfacique du problème. L'absence d'outils performants à notre disposition pour simuler les échos radar dans un milieu complexe en 3D m'a amené à concentrer mes efforts sur les propriétés géophysiques de l'interface atmosphère/ sous-sol. La majeure partie de ma thèse a été dès lors consacrée à l'inversion des paramètres géophysiques dans un cadre probabiliste en utilisant une formulation surfacique. De manière plus spécifique, j'ai essayé d'estimer les coefficients

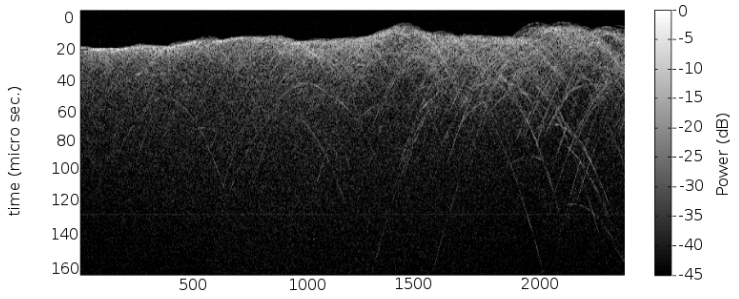

(a) Real data

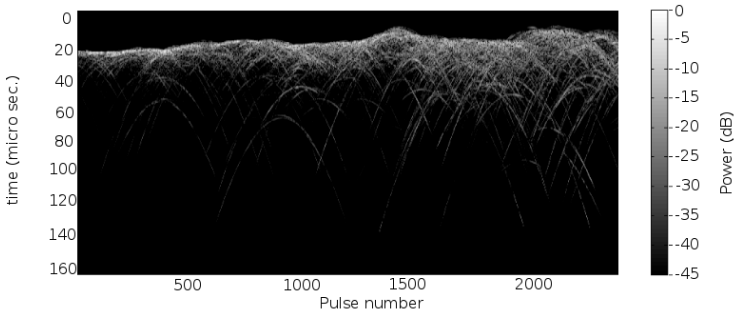

(b) Simulated data

Figure 2: Simulation d'échos radar pour l'instrument LRS. L'échelles des couleurs est en décibels [Berquin et al., 2012].

de réflexion à l'interface atmosphère-sous-sol et de corriger conjointement la topographie de l'interface en utilisant les données radar. La dernière partie des travaux est donc dédiée Ã l'inversion des signaux radar en utilisant le principe de Huygens-Fresnel dans un cadre probabiliste (c.f. section 5). Les travaux détaillent plus particulièrement les stratégies de recouvrement des paramètres diélectriques dans le cas de milieux homogènes en sous-sol avec trois approches différentes: (i) linéarisation du problème, (ii) techniques d'optimisation et (iii) méthodes statistiques. Une discussion sur l'inversion d'autres paramètres est également incluse dans la section 6 avec notamment une étude préliminaire de l'inversion topographique. Les algorithmes présentés sont illustrés avec des données synthétiques dans différentes configurations.

Dans l'ensemble, ce manuscrit met en évidence, je l'espère, l'intérêt des mathématiques appliquées pour le sondage radar. L'exploitation au mieux des données radar ne saurait faire l'économie des progrès dans les domaines des inversions des champs éléctromagnétiques et de la modélisation numériques. L'apport de ce travail repose principalement dans l'analyse quantitative des données radar, mais également dans l'évaluation des performances des radars sondeurs notamment avec les implications en terme de fusion de données (différents instruments et/ou orbites proches).

Seul, j'étais pas assez nombreux.

— Marc Elbichon

ACKNOWLEDGMENTS

Parce que ce manuscrit est avant tout un héritage des travaux de mes glorieux prédécesseurs et parce qu'il est de tradition de rappeler que l'esthétique d'un projet c'est aussi les personnes qui le rendent possible, quelques remerciements s'imposent.

Je tiens tout d'abord à remercier mon directeur de thèse Wlodek Kofman qui a rendu cette thèse réalisable tant d'un point de vue scientifique que logistique. Au-delà de ses précieux conseils et de son temps, je lui suis particulièrement reconnaissant de m'avoir laissé une si grande liberté dans la conduite des travaux. Sa patience aura également été remarquable devant mes entêtements fréquents et ma rédaction peu orthodoxe. Travailler sous sa direction a été une expérience unique et enrichissante. Il laissera l'empreinte d'un idéal scientifique et j'espère réussir à poursuivre sa tradition d'excellence.

Mon travail aura également beaucoup bénéficié de l'encadrement offert par Alain Herique. Ses grandes connaissances techniques et scientifiques (et rédactionnelles !) m'ont énormément aidé et je lui en suis très reconnaissant. Nos longues et passionnées –mais non moins amicales– discussions auront souvent enflammé le couloir et son bureau. Elles me manqueront grandement et j'espère que les nouveaux étudiants sauront relever ses sympathiques défis intellectuels qui en font un grand dueliste scientifique !

Essam Heggy mérite aussi ma reconnaissance la plus profonde pour son accueil chaleureux aux US et pour son encadrement. Sa bienveillance, sa très grande gentillesse et son entrain ont rendu mon séjour beaucoup plus agréable. Ses grandes connaissances en planétologie m'ont permis de mieux comprendre les enjeux des travaux et je garderai les meilleurs souvenirs des cessions de travail le dimanche à Caltech ou le soir où les burritos s'invitaient régulièrement pour alimenter les études radar. J'espère que l'on aura l'occasion de travailler ensemble à nouveau !

Je tiens également à remercier les membres du jury notamment mes rapporteurs Jean-Pierre Barriot et Amélie Litman pour leurs remarques et conseils qui ont permis d'améliorer sensiblement le manuscrit et offrent des perspectives de travail intéressantes. Je remercie aussi Roberto Orosei pour son intérêt dans mes travaux et Jean-Louis Monin qui a accepté de présider mon jury de thèse.

Tout ce travail ne saurait exister sans mes supports financiers. Je remercie donc le CNES pour l'octroiement d'une bourse doctorale et le suivi de mes travaux et le JPL pour sa participation financière lors de mon séjour aux US.

Il me faut aussi remercier l'ensemble des membres du laboratoire et plus particulièrement ceux du bâtiment D qui auront constitué mon environnement de travail au cours de ces quatre années. Une pensée particulière va à Jean Lilenstein avec qui j'aurai partagé mon bureau et qui aura brillé par sa gentillesse. Je remercie aussi Lydie, Pierre, Pop et Roland pour leur présence et leur gentillesse.

Dans un registre plus technique, je tiens à remercier Ludovic Léau-Mercier et Philippe Bollard pour leur aide en informatique et notamment en C++. Je ne

compte plus les fois où ils m'auront débloqués lors de ma première année de thèse. Je tiens aussi à remercier Yves pour son aide en informatique: C++, CIMENT, VTK, Paraview, Eigen, Linux il aura été de tous les combats PC vs homme et je lui dois beaucoup. Il aura également été un excellent co-bureau durant ces derniers mois. Bonne chance pour la suite !

A tous les thésards et stagiaires, compagnons de route et de doutes, je vous dis un grand merci ! Aux anciens qui sont déjà parti vers d'autres destinations, Florence, Jean-Yves, Ratajczak, Cyril ce fut un plaisir of course. A ceux laissés au champ d'honneur des thèses inachevées, à vous qui avez peut-être vu une réalité trop souvent oubliée du monde scientifique, Axel et Stefano, il ne tient qu'à nous de changer ce monde de fous. A Marco, stagiaire hors du commun, capitaine d'une équipe de foot de bras cassés, tu nous auras manqué cette dernière année, mais ton travail restera un socle solide dans l'estimation d'orbites. A Alex, Amir, Johannes, Zara, Mathilde, Maël etc., la liste serait trop longue pour tous vous citer, les paroles s'envolent mais les photos restent!

A Gaël et Simon parce que notre amitié est une invariante.

A mes amis de longue durée que les distances n'ont jamais vraiment séparés, Thomas, Hana, Guillaume, Dongyun et Chris parce que cette thèse j'aurai aimé que vous puissiez y assister.

A toi Jing. This PhD is simply miraculous because you came into my life.

Enfin, même s'ils arrivent en dernier dans ces remerciements, ils seront toujours les premiers et ils le savent. Mes fantastiques parents, mon idiot de frère, ma folle de soeur. Il ont toujours été là et le seront toujours.

This manuscript uses *A Classic Thesis Style: An Homage to The Elements of Typographic Style* by André Miede (*http : //www.miede.de*) as a template.

CONTENTS

ACRONYMS

JUICE JUpiter ICy moons Explorer

RIME Radar for Icy Moons Exploration

MARSIS Mars Advanced Radar for Subsurface and Ionosphere Sounding

SHARAD SHAllow RADar sounder

LRS Lunar Radar Sounder

MRO Mars Reconnaissance Orbiter

ESA European Space Agency

SELENE Selenological and Engineering Explorer

CONSERT COmet Nucleus Sounding Experiment by Radiowave Transmission

GPR Ground Penetrating Radar

SAR Synthetic Aperture Radar

DEM Digital Elevation Model

FDTD Finite Difference in Time Domain

HRSC High Resolution Stereo Camera

HiRISE High Resolution Imaging Science Experiment

NASA National Aeronautics and Space Administration

Part I

INTRODUCTION

This section details the general context of my PhD work and presents a study on the topography of Jupiter's icy moon Ganymede. A foreword is also provided to help the reader understanding the structure of the manuscript.

1

PLANETARY SOUNDING RADAR AND THE JUICE MISSION: AN OVERVIEW

See,
here I'm now sitting by myself,
uh, er, talking to myself.
That's, that's chaos theory.

— Dr. Ian Malcolm

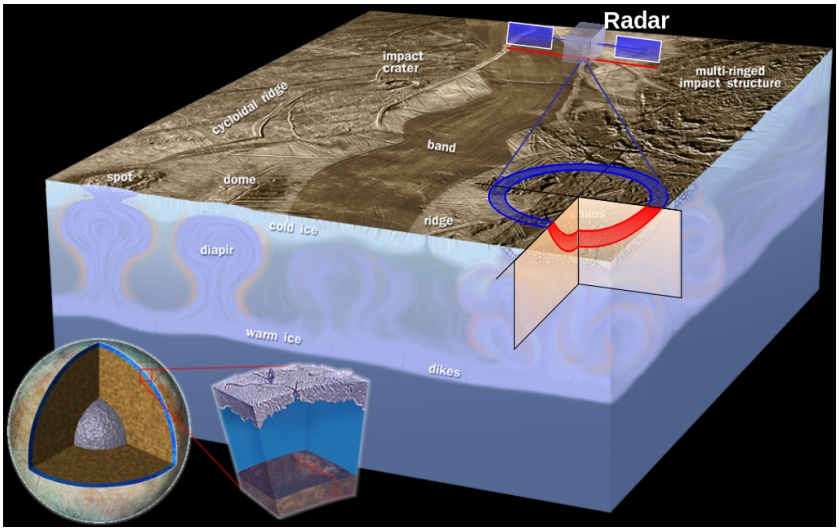

Figure 3: Image representing RIME instrument performing an acquisition over Ganymede. The electromagnetic signal is represented by a smooth wavefront propagating in the subsurface (red) and by the surface reflection (blue). The time delay is identical along the wavefront, hence an ambiguity arises to distinguishes scattering in three dimensions.

Planetary sounding radar is a technique analogous to Ground Penetrating Radar (GPR) (e.g. [Deming and Devaney, 1997; Grimm et al., 2006; Saintenoy et al., 2013]) and Synthetic Aperture Radar (SAR) (e.g. [Cumming and Wong, 2005; Raney et al., 1994]). The basic principle is to perform electromagnetic remote sensing of planetary bodies with active radar measurements targeting mainly subsurface areas. Several experiments have been designed to study planetary bodies. To this day, two of these instruments are used to study Mars' ionosphere and subsurface, namely the Mars Advanced Radar for Subsurface and Ionosphere Sounding (MARSIS) [Picardi et al., 2004] aboard Mars Express (ESA, 2003) and the SHAllow RADar sounder (SHARAD) [Seu et al., 2004] embarked on the Mars Reconnaissance Orbiter (Mars Reconnaissance Orbiter (MRO), National Aeronautics and Space Administration (NASA), 2005) probe. A radar instrument, LRS [Ono and Oya, 2000; Ono et al., 2010] has also been used to study the Moon as part of the Selenological and Engineering Explorer (SELENE) mission. An additional experiment will be conducted [Kofman et al., 2007] – the COmet Nucleus Sounding Experiment by Radiowave Transmission (CONSERT) – to study the interior of the comet 67P/ Churyumov-Gerasimenko (Rosetta, ESA, 2004).

These radar operate at low carrier frequencies and bandwidth ranging from 1 MHz to few 100 MHz depending on the instruments. Transmitted signals are usually *chirps* and antennas used in these experiments are mostly dipoles or cross dipoles (e.g. [Ono et al., 2010; Kofman et al., 2007; Picardi et al., 2004]). Experiment setups include either a single emitter/receiver antenna (monostatic) or two antennas (bistatic) – emitter and receiver respectively – at different locations. Antennas are usually located several hundreds of wavelength away to the planetary body. Furthermore, results at Mars (e.g. [Picardi et al., 2004; Plaut et al., 2009; Seu et al., 2007; Mouginot et al., 2010]) have conclusively demonstrated that this technique is effective in the investigation of planetary bodies. Planetary sounding radar is unique in the sense that it allows to perform remote sensing at structural geology scales (i.e. few hundred meters to few kilometres sounding depth with resolutions varying from a few meters to hundred of meters). In this manuscript, we shall adopt a very large point of view for the problem at hand through considering low frequencies remote electromagnetic sounding techniques with a special attention to JUICE (formerly known as EJSM/Laplace), the first large-class mission in ESA's Cosmic Vision 2015-2025 programme and more specifically to its sounding radar instrument. JUICE is planned for launch in 2022 and arrival at Jupiter in 2030, the probe will spend at least three years making detailed observations of the giant gaseous planet Jupiter and three of its largest moons, Ganymede, Callisto and Europa. These moons are thought to harbour vast water oceans beneath their icy surfaces and JUICE will map their surfaces, sound their interiors and assess their potential for hosting life in their oceans. The spacecraft will perform a dozen flybys of Callisto and will fly past Europa twice in order to make the first measurements of the thickness of its icy crust. JUICE will end up in orbit around Ganymede, where it will study the moon's icy surface and internal structure, including its subsurface ocean. The mission will embark on-board eleven instruments to fulfil its goals,

- JANUS: Jovis, Amorum ac Natorum Undique Scrutator, camera system.
- MAJIS: Moons and Jupiter Imaging Spectrometer. From the yellow book, the instrument should study the composition of the moons' surfaces and the composition, dynamics, structure and morphology of the Jupiter atmosphere.
- UVS: UV Imaging Spectrograph will acquire images to explore the surfaces and atmospheres of Jupiter's icy moons and how they interact with the Jupiter environment.
- SWI: Sub-millimetre Wave Instrument will investigate the structure, composition and dynamics of the middle atmosphere of Jupiter and exospheres of its moons, as well as thermophysical properties of the satellites surfaces
- GALA: Ganymede Laser Altimeter will provide data about the topography, shape and tidal deformation of the icy surfaces.
- RIME: Radar for Icy Moons Exploration will sound the icy crust of Europa, Ganymede, and Callisto.
- J-MAG: Magnetometer for JUICE instrument will characterize the permanent internal/intrinsic magnetic field of Ganymede; establish and characterize magnetic induction signatures in possible subsurface oceans at Ganymede, Europa and Callisto; investigate Ganymede's mini-magnetosphere which is embedded within the Jovian magnetosphere; observe magnetic field signatures within the Jovian magnetosphere and aid in characterizing the dynamics within this magnetosphere.
- PEP: Particle Environment Package will measure the neutral material and plasma in Jupiter's environment.

- RPWI: Radio and Plasma Wave Investigation
- 3GM: Gravity and Geophysics of Jupiter and Galilean Moons dedicated to the characterisation of internal structure and subsurface oceans at Ganymede and Callisto and possibly at Europa by tracking the spacecraft.
- PRIDE: Planetary Radio Interferometer and Doppler Experiment

The science objectives have been defined according to the planetary object studied. The main science objectives for Ganymede – as defined by ESA – are: (i) characterisation of the ocean layers and detection of putative subsurface water reservoirs; (ii) topographical, geological and compositional mapping of the surface; (iii) study of the physical properties of the icy crusts; (iv) characterisation of the internal mass distribution, dynamics and evolution of the interiors; (v) investigation of the exosphere; (vi) study of Ganymede's intrinsic magnetic field and its interactions with the Jovian magnetosphere. Concerning Europa, the focus is on the chemistry essential to life, including organic molecules, and on understanding the formation of surface features and the composition of the non water-ice material. Furthermore, JUICE should provide the first subsurface sounding of the moons, including – hopefully – the first determination of the minimal thickness of the icy crust. Specifically, the radar sounder is expected to acquire information on the different stratigraphic and structural patterns in order to characterize the crustal behavior. As shallow crustal structures are often directly linked with surface features, the process of formation of surface features (and thus of evolution of the moons) would be better understood by investigating subsurface structures. Subsurface structures not directly linked with surface features may also exist in Jupiter moons and can be detected using the radar sounding instrument. The sounding data would also allow an analysis of the material in the subsurface (through proper inference processes) and their metamorphism linked to the burial process. Moreover, the overall information collected by the sounder will also help to understand the large scale geological processes active in the moons at the global scale and to reconstruct their geological evolution. All of these targets are driving the design of the Radar for Icy Moons Exploration (RIME).

2

A STUDY ON GANYMEDE'S SURFACE TOPOGRAPHY: PERSPECTIVES FOR SOUNDING RADAR

From the sounding radar point of view, the strongest natural reflector is the atmosphere/subsurface interface characterized by a sharp permittivity discontinuity. It results in an important signal echo which can become a paramount issue when analysing the data (e.g. [Berquin et al., 2012; Fa et al., 2009]). The complexity of the surface echo – also referred to as surface clutter – mainly depends on the surface topography. Its effects are radar wavefront distortions and overlapping of scattered radar subsurface and surface signals. A study of Ganymede and Europa's topographies unveils challenging sounding environments with important topographic features as presented in the following concise paper. Observed topographic features on Ganymede are similar to those observed in the vicinity of the Olympus Mons on Mars which have raised concerns on the ability to conduct sounding radar experiments with SHARAD-like radar characteristics. Originally, the frequency had been chosen to be in the range 20–50 MHz (chirp signals) due to the important Jovian noise at lower frequencies (e.g. [Cecconi et al., 2012]). However, due to the important surface clutter detailed in the paper, RIME central frequency was eventually set at 9 MHz (1 and 3 MHz bandwidth) as a trade-off between Jovian noise and surface scattering. The instrument will further take advantage of the SHARAD and MARSIS experiments. This should allow to study the subsurface structure of the icy moons down to 9 km depth with vertical resolution of up to 30 m in ice.

Planetary and Space Science 77 (2013) 40–44

Contents lists available at SciVerse ScienceDirect

Planetary and Space Science

journal homepage: www.elsevier.com/locate/pss

A study on Ganymede's surface topography: Perspectives for radar sounding

Y. Berquin [a,*], W. Kofman [a,1], A. Herique [a], G. Alberti [b], P. Beck [a]

[a] UJF-Grenoble 1/CNRS-INSU, Institut de Planétologie et d'Astrophysique de Grenoble (IPAG) UMR 5274, Grenoble F-38041, France
[b] CO.RI.S.T.A., Consorzio di Ricerca su Sistemi di Telesensori Avanzati, Viale Kennedy 5, 80125 Napoli, Italy

ARTICLE INFO

Article history:
Received 8 August 2011
Received in revised form
7 June 2012
Accepted 3 July 2012
Available online 14 July 2012

Keywords:
Ganymede
Surface
Radar sounding
Wave propagation
Mars

ABSTRACT

Radar sounding of Jovian icy satellites has great potential to address specific science questions such as the presence of subsurface liquid water. Radargrams acquired over Mars polar caps allow observing clear echoes up to kilometers depth. However, Jovian icy satellites display dramatically different surface topographies. In order to assess possible issues arising from such surface topographies on radar sounding, we performed a study on different DEMs (Digital Elevation Models) obtained on Ganymede. Topographic data are derived using stereo and photoclinometric analysis of Galileo and Voyager images at resolutions of 16–629 m. Main results are presented in this paper. Overall we found that Ganymede's surface is quite rough, with mean slopes at 630 m scale varying from 3.5° to 8°, smoothest terrains being found within sulcii. This will be a major challenge for the design of radar sounders and parameters should be chosen accordingly in order to correctly sound this planetary body. Previous studies have shown similar concern for Europa.

1. Introduction

Radar sounding has shown great success in the study of terrestrial and extra-terrestrial surfaces. Today, both Mars and the Moon have been probed by mean of ground-penetrating radars, which is one of the very few techniques that can remotely probe subsurfaces. On the Moon, deep interfaces have been observed in the mare which might correspond to the basement of these thick magmatic flows (Ono et al., 2009; Pommerol et al., 2010). On Mars, sounding of the polar caps was achieved with great success by both Marsis and Sharad radars, providing unique information on the structures and formation mechanisms of these deposits (Grima et al., 2011; Plaut et al., 2007, 2009). In the framework of planetary radars, Galilean satellites appear as highly interesting targets given the suspected presence of a superficial water ocean (McCord et al., 2001), with a high habitability potential. Oceans are expected to be as deep as 3–40 km for Europa and 60–80 km for Ganymede (Spohn and Schubert, 2003; Zimmer et al., 2000). Although radar penetration can be quite important in water ice (down to few kilometers in the case of Marsis radar), surface topography can have first order effects on the instrument performance. An important work has already been conducted for Europa and Ganymede to some extent (Schenk, 2009). Our goal in this paper is to characterize Ganymede's surface topography to better understand its surface properties from a radar point of view. These results should help to put constraints on the design of a possible future radar. We use topographic data derived from the Voyager and Galileo missions images to try to constrain the surface structure and to quantify its geometry (in terms of slopes and RMS heights). Scale dependency and its implication on wave propagation are also discussed therein as well as comparison to analog terrains with available radar data.

2. Topographic data

The Ganymedian surface is often described as a mix of two types of terrain: older, moderately cratered to highly cratered, dark regions and somewhat younger, brighter regions marked with an extensive array of grooves and ridges (sulcii) (Head et al., 2002; Oberst et al., 1999; Patterson et al., 2010; Prockter et al., 1998, 2010; Squyres, 1981). The dark terrain covers about one-third of the surface. Analyses of Galileo images have shown that locally, terrains can have surface characteristics which differ noticeably (Pappalardo et al., 2004). In order to investigate the different terrain types observed on Ganymede's surface, three typical examples were selected (Fig. 1). They include both bright and dark regions and should give a fairly good insight of the topography that would be encountered. Vertical resolutions in DEMs range from less than 10–50 m.

2.1. Arbela Sulcus region

A first DEM derived from Galileo images using stereo image analysis techniques (Giese et al., 1998, 2001; Schenk, 2003) was obtained in Arbela Sulcus region (bottom left of Fig. 1).

* Corresponding author. Tel.: +33 47 6514149.
E-mail address: yann.berquin@obs.ujf-grenoble.fr (Y. Berquin).
[1] Visiting professor at Space Research Centre of the Polish Academy of Sciences, ul. Bartycka 18A, Warsaw, Poland.

0032-0633/$ - see front matter © 2012 Elsevier Ltd. All rights reserved.
http://dx.doi.org/10.1016/j.pss.2012.07.004

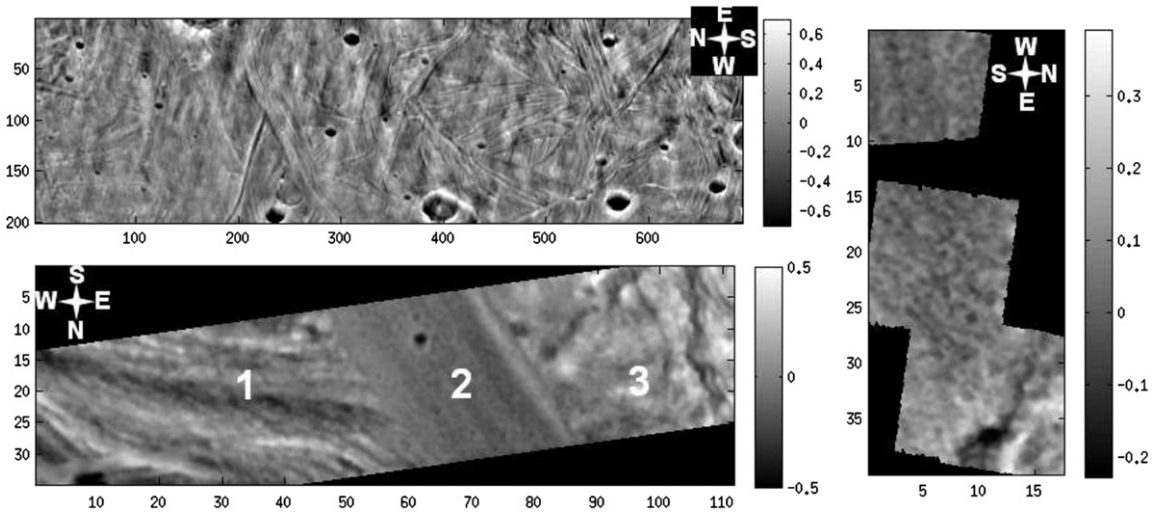

Fig. 1. Top left: raw Ganymede Digital Elevation Model (DEM) data. Note: scale and topography are in kilometers. Bottom left: base Digital Elevation Model (DEM) in the vicinity of Arbela Sulcus. Numbers (1, 2 and 3) correspond to the three data subsets studied. Right: base DEM in the vicinity of Harpagia Sulcus. The small black dots correspond to corrupted data (interpolation was carried out for the study).

The effective resolution of the elevation model (i.e. horizontal resolution of the topography map which is different from the one of the base images) is around 350 m at best. Arbela Sulcus is a prominent SSW–NNE trending smooth, 20 km-wide band (Pappalardo et al., 1998). Most parts of the band are topographically lower than the near surroundings, primarily dark terrain. The band is not smooth but there is lineated topography within. The eastern boundary consists of a ridgelike feature with a top-to-bottom elevation of up to 200 m on its western edge. It stands higher than the surrounding, older dark terrain to the east but does not embay it. The western boundary of the band is not elevated and stands lower than or at about equal topographic level as the surrounding terrain to the west. Grooved terrain is characterized by sub-parallel ridges and troughs at different scales. Such type of terrain is featured by the SW–NE trending band cut by Arbela Sulcus (visible to the west of Arbela in Fig. 1). It has an undulatory topography with a characteristic length of about 6 km and amplitudes reaching 400 m. Rifted terrains can be observed in many places (Pappalardo et al., 1998) but most of these rifts are too small to be resolved by the DEM. Craters with different sizes and degrees of structural deformation are distributed across the study area.

2.2. Harpagia Sulcus region

A second DEM derived from high resolution Galileo images using stereo image analysis techniques as well (Giese et al., 1998; Schenk, 2003) was obtained in Harpagia Sulcus region (right of Fig. 1). The effective resolution of the elevation model is around 350 m at best. This specific bright region appeared as a surprisingly smooth surface on Voyager data (Head et al., 2001). However, observations from Galileo proved this area to be quite rough and heavily pitted by small craters and to contain relatively common but degraded linear elements. This smooth terrain is clearly cut by younger grooved terrain along its eastern margin.

2.3. Bright terrain (Voyager data)

A third and last low resolution DEM (top left of Fig. 1) was derived from Voyager images using photoclinometric techniques (Squyres, 1981). This data set covers a considerably larger area and has an effective resolution of approximately 630 m. It displays typical features (ridges mostly here) observed within bright terrain areas as well as numerous impact craters of different sizes which significantly alter the topography.

3. Methodology

In order to fully characterize terrains (for radar sounding purpose), different parameters were studied. We mainly focused on surface slopes, correlation lengths and height standard deviations. Each of these parameters was computed over DEM square samples of dimension $L \times L$ (L being called hereafter *window length*). Graphics usually display parameters mean for a set of window lengths L for the available DEMs.

At a given point on a surface $z = f(x,y)$, the slope S is defined as a function of gradients at x and y (i.e. WE and NS) directions.

$$S = \arctan(\sqrt{f_x^2 + f_y^2}) \quad (1)$$

where f_x and f_y are the gradients at NS and WE directions, respectively. From the previous equation, it is clear that the key for slope computation is the estimation of f_x and f_y. Since we are interested in surface properties for radar sounding design, slopes are considered over a surface and not over a profile. Furthermore, since we are interested in slope variations with lateral scale L, we subdivide the surface into $L \times L$ planes. We determine the slope and aspect of each plane by fitting it to the surface height point using a least squares method.

Correlation length was defined as the minimum threshold value at which the normalized 2D correlation function of a given DEM sample equals 0.37 (i.e. 37% of its maximum). It is a simplistic definition. However, as mentioned above, we are interested in the possible hampering arising from the surface in radar sounding. Hence, rough estimations are sufficient at the moment. DEM samples are detrended through removing a plan fitted in the least square sense.

We paid extra attention to scale dependency behaviours in surface statistics. Indeed, surface characteristics are functions of scales at which they are observed. One way to deal with it is to assume self-affine behaviour of the surface within a certain range of scales. This topic has been extensively discussed over the last decades and such behaviours have been shown to be well suited to describe natural surfaces (Orosei et al., 2003; Power and Tullis, 1991; Picardi et al., 2004). This approach is particularly

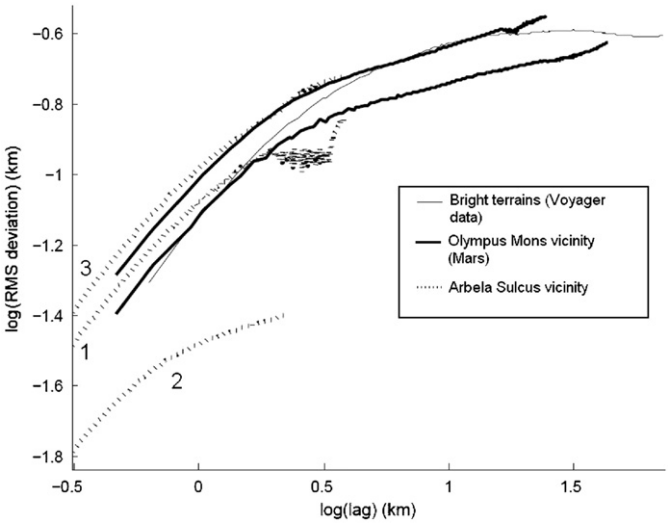

Fig. 2. Allan deviations from different data sets. Log(km)–log(km) scales. Dotted lines correspond to terrains within Arbela Sulcus vicinity numbered according to areas defined in Fig. 1. Large plain lines correspond to MOLA data on Mars and plain line corresponds to the DEM obtained with Voyager images. Allan deviation from MOLA data are very much comparable to those observed on Ganymede except for terrains located in the sulcus which have noticeably smaller height variations (smoother).

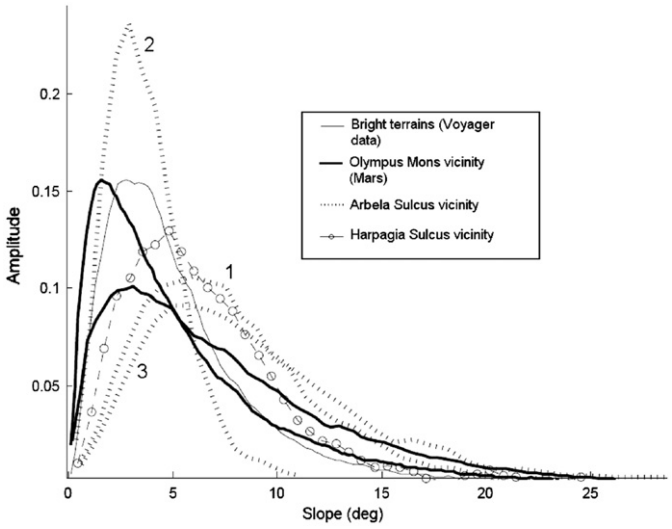

Fig. 3. Slope histograms for major observed terrains. Data are for sites observed at 630 m resolutions roughly (except for MOLA data observed at 463 m). Bright terrains from Voyager images are plotted with a thin plain line, terrains in Arbela Sulcus vicinity are plotted with dotted lines and numbered according to areas defined in Fig. 1. Histogram with large circles corresponds to Harpagia Sulcus area and remaining histograms with large plain lines correspond to MOLA data on Mars (rough area in the Olympus Mons vicinity). Histograms from Mars data are within the range of values observed on Ganymede, expect for terrain in the sulcus (although Mars histograms have larger tails, i.e. more extreme topographic events). Area below the curves are normalized to one.

convenient since it allows an explicit roughness scale dependent formulation (Shepard et al., 1995; Shepard and Campbell, 1999). For a self-affine profile or surface, RMS height variations, RMS slopes are a function of the sample length over which they are measured (Shepard et al., 1995). The surface is fully described through a standardized reference length and its Hurst exponent (Shepard and Campbell, 1999). We report here surface RMS deviations v in Fig. 2 (also referred to as structure function, variogram or Allan deviation). In essence, this parameter is a measure of the difference in height between points separated by a distance Δx.

$$v(\Delta x) = [\langle (z(x+\Delta x) - z(x))^2 \rangle]^{1/2} \quad (2)$$

Unfortunately, as seen in Fig. 2, available DEM cover too limited spatial ranges to build a scale dependent model. Figs. 2 and 4 provide an insight on the scale dependency of surface parameters. Small scales close to DEM resolution are likely affected by DEM resolutions which smooth the surface (attenuation of height variations). This effect probably accounts for slope breaks observed in Fig. 2. At large scales, height variations are usually bounded and reach a plateau. Overall, no typical self-affine behaviour was observed so far over a sufficient range of scales to extract robust Hurst exponents.

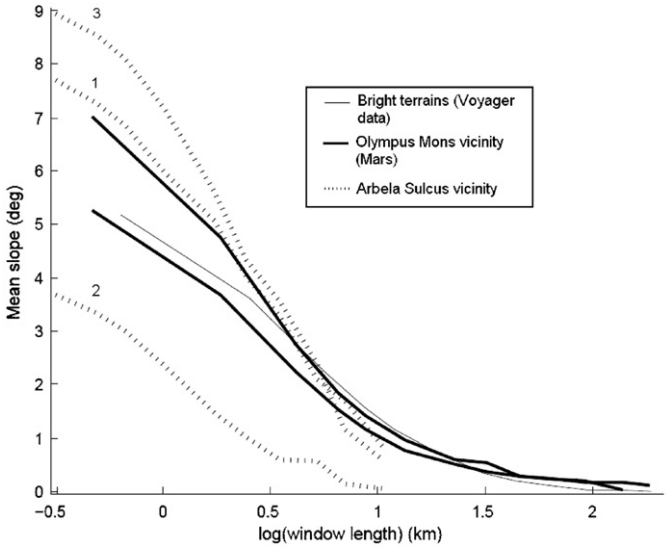

Fig. 4. Mean slopes as a function of window width L. Deg–log(km) scales. Dotted lines correspond to terrains within Arbela Sulcus vicinity numbered according to areas defined in Fig. 1. Large plain lines correspond to MOLA data on Mars and plain line corresponds to the DEM obtained with Voyager images. Mean slopes from MOLA data are comparable to those observed on Ganymede except for terrains located in the sulcus which are noticeably smoother.

4. Results

We mainly differentiated between available data sets and additionally we subdivided the data set in the Arbela region into three sets containing terrains to the west of the sulcus, the sulcus (Arbela band) and terrains to the east of the sulcus due to their obvious morphologic differences as presented in Fig. 1. Each data set obtained was then considered to be spatially stationary (note: this hypothesis solely relies on geological considerations at scales we are interested in). Main results are presented in Figs. 2–4. It is worth noticing that DEM in the Harpagia Sulcus region does not cover sufficient scale ranges to perform scale dependent analysis.

In addition, a comparison was conducted with two sets of surfaces on Mars observed with MOLA (Mars Orbiter Laser Altimeter) at 463 m resolution (Kreslavsky and Head, 1999, 2000). These surfaces are located in the vicinity of Olympus Mons. They display, at these scales similar behaviours to those observed on Ganymede in terms of slopes, correlation lengths and height variations (Figs. 2–4). Radargrams obtained in these areas are available (Fig. 5). This area on Mars is considered as *very rough* in comparison to the rest of the planet. Materials on Ganymede differ noticeably from those on Mars. In terms of scattering this

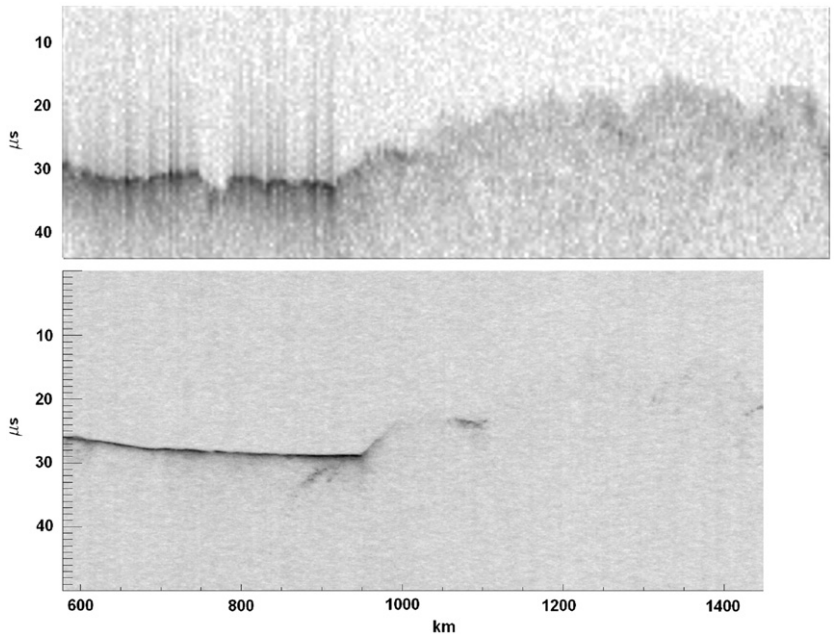

Fig. 5. Radargrams obtained in the Olympus Mons region (MARSIS top and SHARAD bottom). MARSIS operates at 3 MHz central frequency (1 MHz bandwidth) on this radargram. SHARAD operates at 20 MHz central frequency (10 MHz bandwidth). We can clearly see that surface scattering leads to a very signal to noise ratio in rough areas.

will primarily affect the electric permittivity in Eq. (3) (see Discussion).

Terrains on the edges of Arbela Sulcus and terrains observed within Harpagia Sulcus region display surprisingly similar slope histograms (Fig. 3) with large mean values around 7.5° to 8° at 630 m. Such terrains will likely produce important lateral radar echoes when performing radar sounding. In comparison, terrain located in Arbela Sulcus shows gentle slopes averaging 3.5° at 630 m. Slopes from DEM obtained from Voyager images sit in the middle, which may be explained by the presence of both sulcii and cratered/ridged terrains. These observations are very similar to those conducted on Europa (Schenk, 2009).

Variations of mean slopes with window lengths display interesting features (Fig. 4). When window lengths are below 1 km roughly, the behaviour is mainly dictated by DEM limited resolutions (smoothing effect). However, at larger scales, slope variations are probably due to natural terrains roughness. This is true only over a limited range of scales. Once again, terrain in Arbela Sulcus shows much smaller average slopes in comparison to other terrains. Considering the limited range of scales available for each DEM (one order of magnitude roughly), we shall only derive parameters at window lengths of the order of magnitude of DEMs sizes. Through such description, we somehow make the assumption that topography within each set can be considered as stationary (topography could be modelled for instance by Gaussian or exponential correlated surfaces).

Typical correlation lengths observed in terrains to the East and West of Arbela Sulcus are around 1.5 km. However this value does not fully describe correlation functions since terrains are strongly anisotropic. Large structures can be clearly seen on the DEM image (Fig. 1). Correlation lengths associated to the DEM obtained with Voyager data are clearly larger reaching few kilometres (3–4 km) which may indicate larger structures in the area, although the resolution might be too low to resolve smaller features. Structures within Arbela Sulcus are smaller with typical correlation lengths around 800 m. Terrains in Harpagia Sulcus region have correlation lengths ranging from 450 m to 1000 m, increasing towards the east. Smaller structures are most likely present within these terrains but are not resolved by available DEMs.

RMS heights within Harpagia Sulcus region are ranging from 40 m to 75 m increasing towards the east. Terrains to the east and west of Arbela Sulcus have RMS heights around 120 m which corresponds to a value of −0.9 in Fig. 2. Whereas Arbela Sulcus terrain RMS height is much smaller around 30 m (−1.5 in Fig. 2). DEM obtained from Voyager images has an RMS height of 150 m (−0.82 in Fig. 2).

Overall, terrains on Ganymede could be qualified as rough in comparison to what has been observed on Mars (see slope values in Fig. 3). Important lateral surface echoes and surface diffusion of the radar signal are very likely to occur during radar sounding experiments. Smoothest areas are located within sulcii which display obvious topographic differences from the rest. These narrow bands (10–100 s of kilometers wide) highlight the presence of relatively smooth terrains on Ganymede that might allow good radar sounding performances. Galileo and Voyager observations have permitted to build models for these grooved terrains. These models mainly induce rift-like processes with a significant role for tilt-block style normal faulting, high thermal gradient, locally high extensional strain, the potential for tectonism alone to cause resurfacing in some regions, and a generally less prominent role for icy volcanism (Pappalardo et al., 2004).

5. Discussion

Preliminary results indicate Ganymede's surface is quite rough (Schenk, 2009) for lateral scales ranging from few hundred meters up to few kilometers. Hence, performances of radar sounding instrument on Ganymede will likely be affected. There is a high risk that the electromagnetic signal wavefront coherency will be lost as it propagates through Ganymede's surface. This would result in a dramatic decrease in the amplitude of the received signal. This power loss χ_t can be easily expressed for Gaussian correlated surfaces in the Kirchhoff approximation (Ishimaru, 1978; Kong, 2000)

$$\chi_t = \exp(-2(\sqrt{\epsilon_1}-\sqrt{\epsilon_0})^2\sigma_h^2 k^2) \quad (3)$$

σ_h is height standard deviation of the surface, k the wavenumber, ϵ_1 is the dielectric permittivity of the subsurface layer and ϵ_0 is the dielectric permittivity of the atmosphere. Although this formulae is only a first order estimation, it stresses out that if it exists surface structures with height variations within Fresnel zone (i.e. useful radar beamwidth on the surface, which has a radius of $\sqrt{\lambda R_0/2}$ with R_0 being the spacecraft altitude) of the same order of magnitude (or more) than the incident wavelength, there will be no coherent signal that propagates through the subsurface. Hence, it is not possible to receive coherent echoes from the subsurface.

Comparison with SHARAD and MARSIS signals (Mouginot et al., 2010) seem to be in agreement with this analysis. Signal displayed in Fig. 5 – from SHARAD and MARSIS – were obtained in Olympus Mons region which displays similar topography characteristics. For both instruments in these rough areas, power received by the antennas decreases dramatically due to surface scattering. It is worth noticing that MARSIS instrument which operates at lower frequencies seems to perform better in these areas with these specific signal treatment. However, these conclusions rely solely on large scale topographic behaviours obtained through DEMs and the work remains qualitative. Lack of information at smaller scales makes it impossible to have a good assessment of the returned echoes at this stage (i.e. radar sounding performances on icy Jovian satellites is unknown). In order to carry out a finer study, a geological model of the subsurface covering different scales (Chyba et al., 1998; Moore, 2000) should be built as well and converted into a permittivity model of the subsurface.

Clutter effect arising from lateral echoes as well as other sources of noise are also of paramount importance but are not discussed here (Cecconi et al., 2011; Kobayashi et al., 2002; Seu et al., 2004). Typically, one would expect the coherent signal returned from the subsurface to have sufficient power with regard to the noise (clutter and additional sources of noise) to properly image subsurface features.

Overall, considering height variations at available spatial resolutions, it is not possible to validate power loss estimations. Extracting σ_h in the formulae above would require DEMs at finer resolutions. SHARAD-like instruments with frequency ranges over 20 MHz do not seem well adapted to Ganymede's rough surface. Lower frequencies should be more adapted as indicated by preliminary estimations. However, due to Jupiter radio emissions, a limited range of frequencies is available. Different scattering models (i.e. derived from different surface models such as Gaussian correlated model or self-affine model, etc.) can be tested to assess the loss of coherency of the returned signal. However, they should not yield dramatic changes if surface characteristic inputs are chosen according to radar wavelength.

Acknowledgments

We gratefully acknowledge the fundamental work conducted by Dr. Paul Schenk who kindly provided us with the DEM s. This work was performed with financial support from CNES.

References

Cecconi, C., Hess, S., Herique, A., et al., 2011. Natural radio emission of Jupiter as interferences for radar investigations of the icy satellites of Jupiter. Planetary and Space Science 59.
Chyba, C.F., Ostro, S.J., Edwards, B.C., 1998. Radar detectability of a subsurface ocean on Europa. Icarus 134, 292–302.
Giese, J., Oberst, T., Roatsch, G., et al., 1998. The local topography of Uruk Sulcus and Galileo Regio obtained from stereo images. Icarus 135, 303–316.
Giese, J., Wagner, R., Neukum, G., et al., 2001. The topography of Ganymede's Arbela Sulcus. Lunar and Planetary Science Conference XXXII, Abstract 1743.
Grima, C., Costard, F., Kofman, W., et al., 2011. Large asymmetric polar scarps on Planum Australe, Mars: characterization and evolution. Icarus 212, 96–109.
Head, J., Pappalardo, R., Collins, G., et al., 2002. Evidence for Europa-like tectonic resurfacing styles on Ganymede. Geophysical Research Letters 29, 2151.
Head, III, J.W., Pappalardo, R.T., Collins, G.C., et al., 2001. Ganymede: Very High Resolution Data from G28 Reveal New Perspectives on Processes and History, Lunar and Planetary Institute. Technical Report, Lunar and Planetary Institute Science Conference Abstracts 32, 1980.
Ishimaru, A., 1978. Wave Propagation and Scattering in Random Media. Academic Press.
Kobayashi, T., Oya, H., Ono, T., 2002. A-scope analysis of subsurface radar sounding of lunar mare region. Earth, Planets, and Space 54, 973–982.
Kong, J.A., 2000. Electromagnetic Wave Theory. EMW Publishing.
Kreslavsky, M.A., Head, J.W., 1999. Kilometer-scale slopes on Mars and their correlation with geologic units: initial results from Mars Orbiter Laser Altimeter (MOLA) data. Journal of Geophysical Research 104, 21911–21924.
Kreslavsky, M.A., Head, J.W., 2000. Kilometer-scale roughness of Mars: results from MOLA data analysis. Journal of Geophysical Research 105, 26695–26712.
McCord, T.B., Hansen, G.B., Hibbitts, C.A., 2001. Hydrated salt minerals on Ganymede's surface: evidence of an ocean below. Science 292, 1523–1525.
Moore, J.C., 2000. Models of radar absorption in Europan ice. Icarus 147, 292–300.
Mouginot, J., Pommerol, A., Kofman, W., et al., 2010. The 3–5 MHz global reflectivity map of Mars by MARSIS/Mars express: implications for the current inventory of subsurface H_2O. Icarus 210, 612–625.
Oberst, J., Schreiner, B., Giese, B., et al., 1999. The distribution of bright and dark material on Ganymede in relationship to surface elevation and slopes. Icarus 140, 283–293.
Ono, T., Kumamoto, A., Nakagawa, H., et al., 2009. Lunar radar sounder observations of subsurface layers under the nearside maria of the Moon. Science 323, 909.
Orosei, R., Bianchi, R., Coradini, A., et al., 2003. Self-affine behavior of Martian topography at kilometer scale from Mars Orbiter Laser Altimeter data. Journal of Geophysical Research 108, 8023.
Pappalardo, R.T., Head, J.W., Collins, G.C., et al., 1998. Grooved terrain on Ganymede: first results from Galileo high-resolution imaging. Icarus 135, 276–302.
Pappalardo, R.T., Collins, G., Head III, J.W., et al., 2004. Jupiter: The Planet, Satellites and Magnetosphere. Geology of Ganymede. Cambridge University Press. (Chapter 16).
Patterson, G.W., Collins, G.C., Head, J.W., et al., 2010. Global geological mapping of Ganymede. Icarus 207, 845–867.
Picardi, G., Biccari, D., Seu, R., et al., 2004. Performance and surface scattering models for the Mars Advanced Radar for Subsurface and Ionosphere Sounding (MARSIS). Planetary and Space Science 52, 149–156.
Plaut, J.J., Picardi, G., Safaeinili, A., et al., 2007. Subsurface radar sounding of the south polar layered deposits of Mars. Science 316, 92.
Plaut, J.J., Safaeinili, A., Holt, J.W., et al., 2009. Radar evidence for ice in lobate debris aprons in the mid-northern latitudes of Mars. Geophysical Research Letters 36, L02203.
Pommerol, A., Kofman, W., Audouard, J., et al., 2010. Detectability of subsurface interfaces in lunar maria by the LRS/SELENE sounding radar: influence of mineralogical composition. Geophysical Research Letters 37, L03201.
Power, W.L., Tullis, T.E., 1991. Euclidean and fractal models for the description of rock surface roughness. Journal of Geophysical Research 96, 415–424.
Prockter, L.M., Head, J.W., Pappalardo, R.T., et al., 1998. Dark terrain on Ganymede: geological mapping and interpretation of Galileo Regio at high resolution. Icarus 135, 317–344.
Prockter, L.M., Lopes, R.M.C., Giese, B., et al., 2010. Characteristics of icy surfaces. Space Science Reviews 153, 63–111.
Schenk, P.M., 2003. Topographic mapping of icy satellites: new methods and new maps. ISPRS 2003.
Schenk, P.M., 2009. Slope characteristics of Europa: constraints for landers and radar sounding. Geophysical Research Letters 36, L15204.
Seu, R., Biccari, D., Orosei, R., et al., 2004. SHARAD: the MRO 2005 shallow radar. Planetary and Space Science 52, 157–166.
Shepard, M.K., Brackett, R.A., Arvidson, R.E., 1995. Self-affine (fractal) topography: surface parameterization and radar scattering. Journal of Geophysical Research 100, 11709–11718.
Shepard, M.K., Campbell, B.A., 1999. Radar scattering from a self-affine fractal surface: near-nadir regime. Icarus 141, 156–171.
Spohn, T., Schubert, G., 2003. Oceans in the icy Galilean satellites of Jupiter? Icarus 161, 456–467.
Squyres, S.W., 1981. The topography of Ganymede's grooved terrain. Icarus 46, 156–168.
Zimmer, C., Khurana, K.K., Kivelson, M.G., 2000. Subsurface oceans on Europa and Callisto: constraints from Galileo magnetometer observations. Icarus 147, 329–347.

3 A FOREWORD ON THE WORK

Considering the problem at hand, I have dedicated my PhD work to radar sounding in *hostile* environments, to pushing the limits of the technique and to recovering quantitative information on the probed environments. The outline of the manuscript matches the chronology of my PhD. The work is divided in three sections. The first one details the physics of sounding radar with a focus on surface formulation. It allows an overview of electromagnetic wave propagation, of the instrument characteristics and presents an improved algorithm to the one presented in [Nouvel et al., 2004] which allows to efficiently compute radar surface echoes from a known surface. This first sections focuses on surface formulations (Huygens-Fresnel's principle) which are the core of the algorithm presented. The second section is devoted to the inversion of surface parameters from sounding radar measurements. Equations are detailed along with illustrations using synthetic data. Three methods are presented, namely (i) the linear inverse problem, (ii) non-linear reflectivity parameters and (iii) a statistical approach. Discussions on the strategies and parameters to inverse are also included. We chose to present the inverse problem using a probabilistic approach (e.g. [Tarantola, 2005]) and we recall in this second section some theory regarding this approach. A last section is dedicated to the conclusions and discussions of the PhD work. It provides some perspectives on possible future studies. As for the appendices, the first one recalls Maxwell's equations and may come handy to understand some notations. The second appendix is an attempt at giving a modern formulation of the work using differential geometry with a great help from the literature (e.g. [Matias, 2012; Warnick, 1997]).

Part II

DIRECT ELECTROMAGNETIC WAVE PROPAGATION IN PLANETARY SOUNDING RADAR

We propose in this section to derive an algorithm to compute efficiently radar echoes based on the Huygens-Fresnel's principle from meshed surfaces.

4

IMPLEMENTING HUYGENS-FRESNEL'S PRINCIPLE USING A MESHED BOUNDARY SURFACE

Hope it doesn't sound arrogant, when I say that I am the greatest man in the world!

— Denholm Reynholm

We propose in this section a technique to simulate planetary sounding radar surface echoes based on surface formulation presented in the previous sections. This topic has lead to a paper which is the core of this section. The technique offers interesting perspectives to compute any electromagnetic fields in a bounded volume Ω for a given closed surface $\partial\Omega$ with its known surface electromagnetic fields. The algorithm presented in this section has been used to compute the forward and transposed operators when conducting the inversion process. This work was mostly inspired by Dr. Jean-Francois Nouvel's PhD work (see [Nouvel et al., 2004]) although it can be related to the well-known boundary elements method (e.g. [Katsikadelis, 2002; Buffa and Hiptmair, 2003]) where in essence we discard the coupling of the elements.

4.1 DISCRETIZATION OF THE BOUNDARY PROBLEM

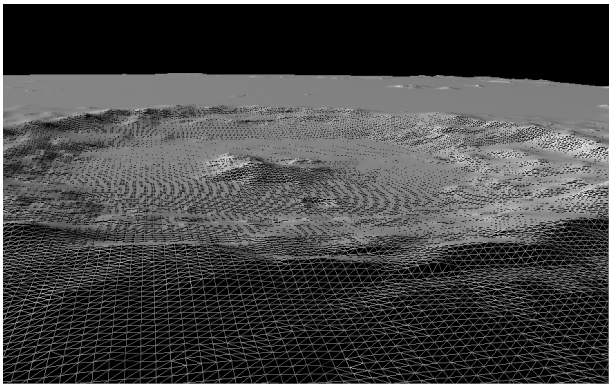

Figure 4: Meshed planetary surface used for simulations showing a crater on Mars. The surface is composed of triangular meshes.

We assume throughout this work the boundary surface $\partial\Omega$ to be correctly described as a contiguous set of $N \in \mathbb{N}$ triangular planar facet elements Δ_α such that $\partial\Omega = \{\Delta_\alpha\}_{\alpha\in N}$. This results in a three dimensional meshed surface (see figure 4). On each facet element, we express the fields as the product of a geometrical term $\mathbf{F}^\alpha(\mathbf{x}_0, \mathbf{x}^\alpha)$ constant over the facet and of a phase term $e^{i\phi_\alpha(\mathbf{x},\mathbf{x}_0)}$. Rewriting equation B.30 accordingly we obtain,

$$\mathbf{E}_s(\mathbf{x}_0, \omega) = \sum_\alpha \mathbf{F}^\alpha(\mathbf{x}_0, \mathbf{x}^\alpha) \int_{\Delta_\alpha} e^{i\phi_\alpha(\mathbf{x},\mathbf{x}_0)} d\sigma(\mathbf{x}) \tag{4.1}$$

Superscript α denotes here the α^{th} facet variables which are constant over each planar facet element while $\mathbf{x}^\alpha$ denotes the geometrical center of mass of the

α^{th} facet. It is worth noting the above equation contains the information on the electric field polarization and is merely the sum of the facet diffracted fields $\mathbf{F}^{\alpha} \int_{\Delta_\alpha} e^{i\phi_\alpha(\mathbf{x},\mathbf{x}_0)} d\sigma(\mathbf{x})$. Computing the the phase integral term $\int_{\Delta_\alpha} e^{i\phi_\alpha(\mathbf{x},\mathbf{x}_0)} d\mathbf{x}$ over a planar facet element is not straightforward. Analytical results can be obtained only in very specific cases. In order to give a generic result for a specified facet element geometry, one has to carry out approximations. We propose to derive a analytical expressions provided conditions in the phase term for triangular facet elements.

Constant phase function

The simplest approximation is to consider a constant phase over a facet element $\phi_\alpha(\mathbf{x}, \mathbf{x}_0) = A_\alpha$ with $A_\alpha \in \mathbb{R}$,

$$\int_{\Delta_\alpha} e^{i\phi(\mathbf{x},\mathbf{x}_0)} d\sigma(\mathbf{x}) = \Delta S_\alpha e^{iA_\alpha} \tag{4.2}$$

Where ΔS_α is the surface of the facet element. Any piecewise $\mathcal{C}^1$ complex function on $\partial\Omega$ can be approached through a set of constant over elementary surface elements. In general this formulation is used to numerically compute Huygens-Fresnel's integral (e.g. [Plettemeier et al., 2009; Kobayashi et al., 2002a,b]).

Linear phase function

We define $\Delta_\alpha = \{\mathbf{x} \mid a.x + b.y + d = z\}$ with $a \in \mathbb{R}$ and $b \in \mathbb{R}$ and $\mathbf{x} = \{x, y, z\}$ where x, y and z are the coordinates in a given Cartesian frame. We assume the phase term can be expressed locally (i.e. over a facet element) as $e^{2jk(-a_0.x - b_0.y + d_0)}$. This amounts to linear variations in the phase function $\phi(\mathbf{x}, \mathbf{x}_0) = 2k\left(-a_0.x - b_0.y + d_0\right)$. In order to compute the analytical phase integral on a triangular facet, we subdivide the integral domain in two right triangle integral domains (see figure 5). This provides rectangular-like integration domains,

$$\begin{aligned} &\int_{\Delta_\alpha} e^{2ik(-a_0.x - b_0.y + d_0)} d\sigma(\mathbf{x}) = J. \\ &\left[\int_{A_x}^{D'_x} \int_{D'_y}^{\alpha_1.x + \beta_1} e^{2ik(-a_0.x - b_0.y + d_0)} dy dx + \right. \\ &\left. \int_{D'_x}^{B_x} \int_{D'_y}^{\alpha_2.x + \beta_2} e^{2ik(-a_0.x - b_0.y + d_0)} dy dx \right] \end{aligned} \tag{4.3}$$

with,

$$\begin{aligned} J &= \sqrt{a^2 + b^2 + 1} \\ \alpha_1 &= \frac{A_y - C_y}{A_x - C_x} \\ \beta_2 &= C_y - \alpha_2 C_x \\ \alpha_2 &= \frac{B_y - C_y}{B_x - C_x} \\ \beta_2 &= C_y - \alpha_2 C_x \end{aligned} \tag{4.4}$$

Where A, B and C are the facet vertices and A_x, A_y and A_z are the coordinates of the vertex A. The coefficient J is the Jacobian that arises when changing the

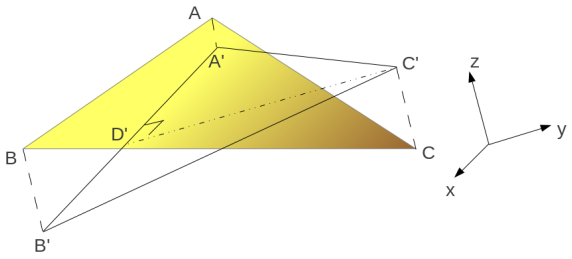

Figure 5: Example of a triangular facet and its associated integration domain in a given frame. The color represents the linear varying phase function over the facet.

integral domain from $\partial\Omega$ (locally Δ_α) to the plane xy. $A'B'C'$ is the integral domain on the plane xy and is built such that primed points A', B' and C' are the projections of the vertices A, B and C on xy through $\mathbf{z}$ respectively. D' is such that $(C'D') \perp (A'B')$ and $C' \in (A'B')$ (see figure 5). The analytical expression of the integral is straightforward given the properties of the exponential function,

$$\begin{aligned}\int_{\Delta_\alpha} e^{2ik(-a_0.x-b_0.y+d_0)} d\sigma(\mathbf{x}) = J.\frac{e^{2.i.k.d_0}}{(2.i.k)^2.b_0}.\\ \left[\frac{e^{-2.i.k.b_0.\beta_1}}{a_0+b_0.\alpha_1}.\left(e^{-2.i.k.D'_x(a_0+b_0.\alpha_1)} - e^{-2.i.k.A_x(a_0+b_0.\alpha_1)}\right) + \right.\\ \frac{e^{-2.i.k.b_0.\beta_2}}{a_0+b_0.\alpha_2}.\left(e^{-2.i.k.B_x(a_0+b_0.\alpha_2)} - e^{-2.i.k.D'_x(a_0+b_0.\alpha_2)}\right)\\ \left. + \frac{e^{-2.i.k.(b_0.D'_y+A_x.a_0)} + e^{-2.i.k.(b_0.D'_y+B_x.a_0)}}{a_0}\right]\end{aligned} \tag{4.5}$$

Should the electromagnetic field vector components be piecewise $\mathcal{C}^1$ complex functions on $\partial\Omega$ with *slow* varying absolute values in comparison to the phase term, they can be written as a sum of analytical functions using equation 4.5 in 4.1.

We have used a unique phase function for all vector field components but the equations can easily be generalized to each individual component with its own phase term.

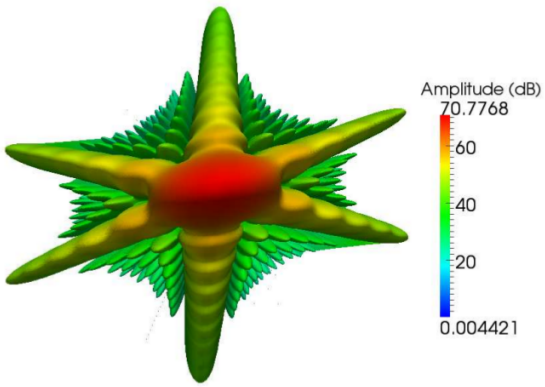

Figure 6: Example of radiated power diagram from a triangular facet element with a linear phase function corresponding to a normal incidence for a given frequency.

4.2 APPLICATION TO PLANETARY SOUNDING RADAR

In the far field approximation, the field radiated by an antenna located at $\mathbf{x}_1$ in a homogeneous medium can be written as $\mathbf{E}_i(\mathbf{x}) = |E_i(\mathbf{x})|e^{ik|\mathbf{x}_1-\mathbf{x}|}\hat{\mathbf{e}}_i$. We shall make use of equations B.43 and B.44 (homogeneous case) and we further define,

$$\begin{aligned}\hat{\mathbf{E}}_{\parallel}(\mathbf{x}) =& \Big((\hat{\mathbf{n}} \times \hat{\mathbf{q}}_i) . \Big[(\hat{\mathbf{e}}_i \cdot \hat{\mathbf{q}}_i) . \left(1 + R^{TE}\right) \Big] + \\ & \hat{\mathbf{q}}_i . \left(\hat{\mathbf{n}} \cdot \hat{\mathbf{k}}_i\right) . \Big[(\hat{\mathbf{e}}_i \cdot \hat{\mathbf{p}}_i) . \left(1 - R^{TM}\right) \Big] \Big)\end{aligned} \tag{4.6}$$

$$\begin{aligned}\hat{\mathbf{H}}_{\parallel}(\mathbf{x}) =& \frac{1}{\eta} . \Big((\hat{\mathbf{n}} \times \hat{\mathbf{q}}_i) . \Big[(\hat{\mathbf{e}}_i \cdot \hat{\mathbf{p}}_i) . \left(1 + R^{TM}\right) \Big] \\ & - \hat{\mathbf{q}}_i . \left(\hat{\mathbf{n}} \cdot \hat{\mathbf{k}}_i\right) . \Big[(\hat{\mathbf{e}}_i \cdot \hat{\mathbf{q}}_i) . \left(1 - R^{TE}\right) \Big] \Big)\end{aligned} \tag{4.7}$$

Replacing $E_i(\mathbf{x})$ with $|E_i(\mathbf{x})|e^{ik|\mathbf{x}_1-\mathbf{x}|}$ in equations B.43 and B.44 we obtain,

$$\mathbf{E}_s(\mathbf{x}_0) = \int_S \left[\bar{\bar{\mathbf{I}}} - \hat{\mathbf{k}}_\mathbf{s}\hat{\mathbf{k}}_\mathbf{s}\right] \left(\eta\hat{\mathbf{H}}_{\parallel}(\mathbf{x}) + \hat{\mathbf{k}}_s \times \hat{\mathbf{E}}_{\parallel}(\mathbf{x})\right) |E_i(\mathbf{x})| \frac{e^{ik(|\mathbf{x}_0-\mathbf{x}|+|\mathbf{x}_1-\mathbf{x}|)}}{4\pi|\mathbf{x}_0-\mathbf{x}|} d\sigma(\mathbf{x}) \tag{4.8}$$

As described in the previous section, we assume the boundary surface $\partial\Omega$ to be correctly described as a contiguous set of $N \in \mathbb{N}$ triangular planar facet elements Δ_α such that $\partial\Omega = \{\Delta_\alpha\}_{\alpha\in N}$. We now have,

$$\mathbf{E}_s(\mathbf{x}_0) = \sum_\alpha \int_{\Delta_\alpha} \left[\bar{\bar{\mathbf{I}}} - \hat{\mathbf{k}}_\mathbf{s}\hat{\mathbf{k}}_\mathbf{s}\right] \left(\eta\hat{\mathbf{H}}_{\parallel}(\mathbf{x}) + \hat{\mathbf{k}}_s \times \hat{\mathbf{E}}_{\parallel}(\mathbf{x})\right) |E_i(\mathbf{x})| \frac{e^{ik(|\mathbf{x}_0-\mathbf{x}|+|\mathbf{x}_1-\mathbf{x}|)}}{4\pi|\mathbf{x}_0-\mathbf{x}|} d\sigma(\mathbf{x}) \tag{4.9}$$

We further assume facet extension to be much smaller than R -with $R = min\{|\mathbf{x}_0 - \mathbf{x}|, |\mathbf{x}_1 - \mathbf{x}|\}$- and field amplitudes to be constant over a facet element. We can now express the field at the surface as the product of a geometrical term $\mathbf{F}^\alpha(\mathbf{x}_0, \mathbf{x}^\alpha)$ constant over the facet and of a phase term $e^{i\phi_\alpha(\mathbf{x},\mathbf{x}_0,\mathbf{x}_1)}$,

$$\mathbf{E}_s(\mathbf{x}_0, \omega) = \sum_\alpha \mathbf{F}^\alpha(\mathbf{x}_0, \mathbf{x}^\alpha) \int_{\Delta_\alpha} e^{i\phi(\mathbf{x},\mathbf{x}_0)} d\sigma(\mathbf{x}) \tag{4.10}$$

$$\mathbf{F}^\alpha(\mathbf{x}_0, \mathbf{x}^\alpha) = \left[\bar{\bar{\mathbf{I}}} - \hat{\mathbf{k}}_\mathbf{s}\hat{\mathbf{k}}_\mathbf{s}\right] \left(\eta\hat{\mathbf{H}}_{\parallel}(\mathbf{x}) + \hat{\mathbf{k}}_s \times \hat{\mathbf{E}}_{\parallel}(\mathbf{x})\right) \frac{|E_i(\mathbf{x}^\alpha)|}{4\pi|\mathbf{x}_0 - \mathbf{x}^\alpha|} \tag{4.11}$$

$$\phi_\alpha(\mathbf{x}, \mathbf{x}_0, \mathbf{x}_1) = k\left(|\mathbf{x}_0 - \mathbf{x}| + |\mathbf{x}_1 - \mathbf{x}|\right) \tag{4.12}$$

We shall now discuss the possibility to express the integral term as an analytical function.

Constant phase function

Assuming the phase term to be constant over the facet element amounts to performing a zero order series expansion (i.e. constant phase term over the facet element) with $\phi_\alpha(\mathbf{x}, \mathbf{x}_0, \mathbf{x}_1) = k\left(|\mathbf{x}_0 - \mathbf{x}^\alpha| + |\mathbf{x}_1 - \mathbf{x}^\alpha|\right)$. In order for this approximation to be valid, facet elements must be small enough with regard to the wavelength. It is equivalent to a numerical integral with each facet elements on the mesh corresponding to an elementary surface element Δ_α. This method is very easy to implement but can be time consuming due to the numerous facet elements needed to describe the surface [Jin, 2012; Plettemeier et al., 2009; Kobayashi et al., 2002a]. Typically, this requires that each element does not exceed $\lambda/10$ in length which can be computationally exhaustive.

Linear phase function

The first step is to provide a linearized form of $\phi_\alpha(\mathbf{x}, \mathbf{x}_0, \mathbf{x}_1)$. We approximate locally the fields -both incident and scattered- as plane waves and we provide each plane with an orthonormal basis $\{\mathbf{d}_1^0, \mathbf{d}_1^1, \mathbf{k}_1\}_\alpha$ and $\{\mathbf{d}_0^0, \mathbf{d}_0^1, \mathbf{k}_0\}_\alpha$ respectively. $\mathbf{k}_0$ and $\mathbf{k}_1$ are the scattered and incident unit vectors respectively along wave vectors which are constant over a facet element. We now express $|\mathbf{x}_0 - \mathbf{x}| + |\mathbf{x}_1 - \mathbf{x}|$ with $\mathbf{x} \in \Delta_\alpha$ and $\tilde{\mathbf{x}} = \mathbf{x} - \mathbf{x}^\alpha$,

$$\begin{aligned} |\mathbf{x}_0 - \mathbf{x}| + |\mathbf{x}_1 - \mathbf{x}| = &\left[(\mathbf{x}^\alpha - \mathbf{x}_0) \cdot \mathbf{k}_0 + \left(\tilde{\mathbf{x}} - (\tilde{\mathbf{x}} \cdot \mathbf{d}_0^0)\mathbf{d}_0^0 - (\tilde{\mathbf{x}} \cdot \mathbf{d}_0^1)\mathbf{d}_0^1\right) .\mathbf{k}_0 \right] \\ &- \left[(\mathbf{x}^\alpha - \mathbf{x}_1) \cdot \mathbf{k}_1 + \left(\tilde{\mathbf{x}} - (\tilde{\mathbf{x}} \cdot \mathbf{d}_1^0)\mathbf{d}_1^0 - (\tilde{\mathbf{x}} \cdot \mathbf{d}_1^1)\mathbf{d}_1^1\right) \cdot \mathbf{k}_1 \right] \end{aligned} \tag{4.13}$$

We recognize a linear function with regard to vector $\mathbf{x}$. Recalling $\Delta_\alpha = \{\mathbf{x} \mid a.x + b.y + d = z\}$, the phase function can easily be developed,

$$\phi_\alpha(\mathbf{x}, \mathbf{x}_0, \mathbf{x}_1) = 2k \left(-\frac{1}{2}.A.x - \frac{1}{2}.B.y + \frac{1}{2}.D \right) \tag{4.14}$$

with,

$$\begin{aligned} A = &-\left[\left(k_{0,x} - (\mathbf{d}_0^0 \cdot \mathbf{k}_0)d_{0,x}^0 - (\mathbf{d}_0^1 \cdot \mathbf{k}_0)d_{0,x}^1\right) + a\left(k_{0,z} - (\mathbf{d}_0^0 \cdot \mathbf{k}_0)d_{0,z}^0 - (\mathbf{d}_0^1 \cdot \mathbf{k}_0)d_{0,z}^1\right) \right] \\ &+ \left[\left(k_{1,x} - (\mathbf{d}_1^0 \cdot \mathbf{k}_1)d_{1,x}^0 - (\mathbf{d}_1^1 \cdot \mathbf{k}_1)d_{1,x}^1\right) + a\left(k_{1,z} - (\mathbf{d}_1^0 \cdot \mathbf{k}_1)d_{1,z}^0 - (\mathbf{d}_1^1 \cdot \mathbf{k}_1)d_{1,z}^1\right) \right] \\ B = &-\left[\left(k_{0,y} - (\mathbf{d}_0^0 \cdot \mathbf{k}_0)d_{0,y}^0 - (\mathbf{d}_0^1 \cdot \mathbf{k}_0)d_{0,y}^1\right) + b\left(k_{0,z} - (\mathbf{d}_0^0 \cdot \mathbf{k}_0)d_{0,z}^0 - (\mathbf{d}_0^1 \cdot \mathbf{k}_0)d_{0,z}^1\right) \right] \\ &+ \left[\left(k_{1,y} - (\mathbf{d}_1^0 \cdot \mathbf{k}_1)d_{1,y}^0 - (\mathbf{d}_1^1 \cdot \mathbf{k}_1)d_{1,y}^1\right) + b\left(k_{1,z} - (\mathbf{d}_1^0 \cdot \mathbf{k}_1)d_{1,z}^0 - (\mathbf{d}_1^1 \cdot \mathbf{k}_1)d_{1,z}^1\right) \right] \\ D = &\left[(\mathbf{x}^\alpha - \mathbf{x}_0) \cdot \mathbf{k}_0 - \left(\mathbf{x}^\alpha - (\mathbf{x}^\alpha \cdot \mathbf{d}_0^0)\mathbf{d}_0^0 - (\mathbf{x}^\alpha \cdot \mathbf{d}_0^1)\mathbf{d}_0^1\right) \cdot \mathbf{k}_0 \right. \\ &\left. + d\left(k_{0,z} - (\mathbf{d}_0^0 \cdot \mathbf{k}_0)d_{0,z}^0 - (\mathbf{d}_0^1 \cdot \mathbf{k}_0)d_{0,z}^1\right) \right] \\ &- \left[(\mathbf{x}^\alpha - \mathbf{x}_1) \cdot \mathbf{k}_1 - \left(\mathbf{x}^\alpha - (\mathbf{x}^\alpha \cdot \mathbf{d}_1^0)\mathbf{d}_1^0 - (\mathbf{x}^\alpha \cdot \mathbf{d}_1^1)\mathbf{d}_1^1\right) \cdot \mathbf{k}_1 \right. \\ &\left. + d\left(k_{1,z} - (\mathbf{d}_1^0 \cdot \mathbf{k}_1)d_{1,z}^0 - (\mathbf{d}_1^1 \cdot \mathbf{k}_1)d_{1,z}^1\right) \right] \end{aligned} \tag{4.15}$$

Subscripts x, y, z denote the coordinates in the reference Cartesian frame. Equation 4.5 then provides the analytical form of the phase integral term. From a functional point of view, the linear phase approximation amounts to performing a first order series expansions at $\mathbf{x}^\alpha - \mathbf{x}_1$ and $\mathbf{x}^\alpha - \mathbf{x}_0$ respectively. In order

for this approximation to be numerically valid, facet edges should not exceed $\sqrt{\lambda R/2}$ which corresponds to the Fresnel zone radius in planetary radar sounding. Figure 7 highlights the limitations on facet extension. Facet edge lengths are typically $n\sqrt{\lambda R/2}$, as n increases, the quality of the results decreases. In practice, n was set to 0.2 in most of our simulations.

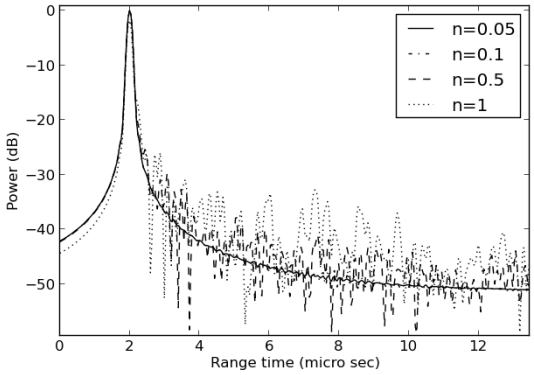

Figure 7: Typical radar responses from flat meshed surfaces with facet edge lengths below $n\sqrt{\lambda H/2}$. Signal distortions can be observed as n increases.

A detailed study of the first order approximation shows Bragg's resonance patterns for structured meshes (see [Nouvel et al., 2004]) when the constraint limit is reached (see Figure 8). These artefacts are due to the first order series expansion approximation in the phase term. Using unstructured meshes allows to avoid Bragg's resonance patterns while using larger mesh when the surface is flat, thus increasing computation efficiency (see Figure 8). The figure shows typical radar response from a regularly sampled flat surface on the left side. The expected reflected surface echo is clearly seen at $30\mu s$. Secondary echoes at 40, 50, 75 and $130\mu s$ corresponds to Bragg's resonance due to the regular mesh. Echo at $40\mu s$ corresponds to border reflection due to the limited extent of the surface in the simulation. On the right side of the figure, typical radar responses from irregularly sampled flat surfaces are displayed with different colors. Similarly, the expected reflected surface echo is clearly seen at $30\mu s$ along with the border reflection at $140\mu s$. Secondary echoes arising later are artefacts much like Bragg's resonance but adding incoherently.
Interestingly, all techniques making use of Huygens' Principle found in the literature naturally relate to the work presented in this section. Fundamentally, their differences arise in the geometry of the facet element used (triangular or square mostly) and on the nature of the quantities associated to each facets used to describe the fields on the surface. In the zero order series expansion case [Jin, 2012; Plettemeier et al., 2009; Zhang et al., 2012], quantities are sets of constant vector (i.e. independent of the position on a facet element) associated to each facet elements, which is fundamentally a numerical integration. Whereas in higher order series expansion cases, quantities are vector fields associated to each facet (i.e. vectors can vary with the position where they are evaluated on a facet element). For instance, in our cases (or [Nouvel et al., 2004] and [Fa et al., 2009]) we have used vector fields with constant directions and linear (or parabolic) phase variations with the position over the facet element. Naturally, the incident and scattered fields quantities are often chosen of the same nature than that of the total facet field which allows scattered fields to be expressed as a function of the incident field. For instance, in our paper we have used local Fresnel's coefficients to express scattered fields. On the other hand, some authors [Ferro et al.,

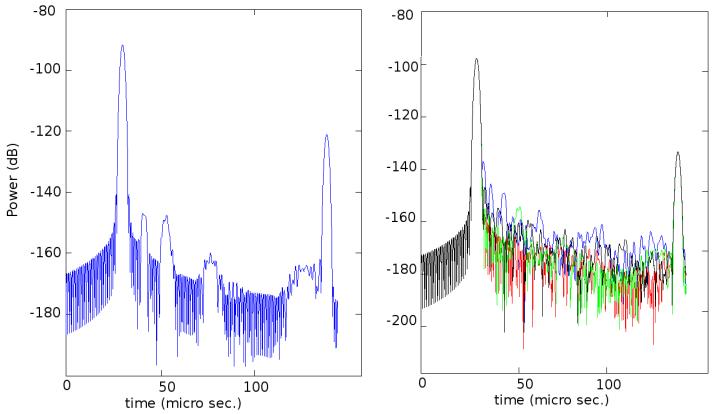

(a) Regularly sampled flat surface (b) Irregularly sampled flat surfaces

Figure 8: Typical radar responses from regularly and irregularly sampled flat surfaces. Regularly sampled surface response displays Bragg resonance patterns unlike responses for irregularly sampled surfaces.

2012; Russo et al., 2008] have used local backscattered coefficients to account for local unknown perturbations in the topography (but statistically characterized). Scattered fields have also been computed using ray tracing methods [Jin, 2012; Zhang et al., 2012] allowing a more global approach and taking also into account subsurface features (this allows coupling between facet elements). However, the fundamental difference does not lie in the computation of surface fields (which are supposed to be known in Huygens' Principle) but rather in the choice of their local facet expressions (i.e. in the nature of the surface quantities).

4.3 IMPLEMENTATION

Huygens' principle can be readily used to compute surface echoes from DEM with an associated surface dielectric model. In our scheme a first step is dedicated to the triangulation of topography data points. This step can be done using Delaunay triangulation for instance (e.g. [Delaunay, 1934]). In order to avoid Bragg's resonance, one might want to resample data. The terrain may contain sharp interfaces between facets on rugged areas which are not necessarily realistic (low resolution of the DEM). To avoid strong diffraction from facet edges, one may perform a smooth interpolation of the surface through a surface subdivision scheme (e.g. [Schroeder et al., 1998]). Further interpolation between DEM data points might be required to match phase integral criterion on facet edge length. We propose here to use Sierpinski subdivision-for the sake of simplicity and efficiency- to match our criterion. Each triangular planar facet obtained after triangulation is subdivided into four homothetic triangular planar facet elements. The subdivision is recursively applied for each triangular facet element until phase integral criterion is matched.

The signal is computed in the frequency domain using the spectrum of the incident electric field. In order to record a given amount of time T, frequency steps should be smaller than $1/T$ as required by Nyquist–Shannon sampling theorem. Hence, the number of frequencies N_f to compute depends on the bandwidth of the signal and on the recording time. It corresponds to $N_f \geq B.T$. For each frequency, the response from a surface area composed of facet elements has to be computed using equation 4.10. The extension of the surface area contributing to the received signal can be derived from the recording time and the emitter/receiver location. Eventually, we can assess the number of facet elementary

responses N to be computed for a single acquisition geometry. Practically, in planetary radar sounding, all these parameters are closely related and computation time does not vary much from one instrument to another. Assuming a flat surface (i.e. surface subdivision does not depend on the surface topography), the minimum number of facet element N for a single acquisition of a given instrument at distance H to the surface can be derived dividing the area *seen* by the radar by the typical surface of a facet element,

$$N = 2.\frac{\pi.c.T.\left(H + \frac{c.T}{4}\right)}{L^2} \tag{4.16}$$

Where L corresponds to facets edge length. Of course, for complex surface geometries, the subdivision may be much higher to accurately describe the surface. In the linear phase approximation, facets edge length correspond to a fraction of λ while in the case of the constant phase approximation facets edge length correspond to a fraction of $\sqrt{\lambda H/2}$. Hence, the number of facets required in the constant phase approximation is approximately H/λ times the number of facets in the linear phase approximation. Considering the facet response in the linear phase approximation is about ten times more computing intensive than that in in the constant phase approximation, the computing time in the linear constant phase approximation is approximately $H/(10 \cdot \lambda)$ times the computing time in the linear phase approximation. Typically, in planetary sounding radar, this corresponds to a hundred times the computing time in the linear phase approximation. Another attractive feature to this approach is its ease to parallelize allowing an efficient use of computing resources. Overall, the technique only depends on the central frequency of the signal through limitations on facet extension (order 2 since it is a surface element). In comparison Finite Difference in Time Domain (FDTD) methods computation efficiency highly depends on the central frequency of the signal (order 4, three space dimensions and one time dimension). Typically, for MARSIS and SHARAD experiments, a single acquisition represents three to ten seconds of computation time with four cores at 1.50GHz. The algorithm proposed is also an improvement to the one in [Nouvel et al., 2004] as it does not suffer from the main shortcoming of squared facets, namely (i) surface discontinuities and (ii) reinterpolation of the surface for each radar location. It further allows bistatic configurations.

To incorporate the characteristics of the transmitting and receiving antennas into the scattering equation we need to modify equations accordingly. This is usually done as a post processing using equation B.24. The code was implemented in C++ using the Eigen library [Guennebaud et al., 2010] and the Vizualisation Tool Kit (VTK) software system [Schroeder et al., 1998].

Data: DEM associated to $\partial\Omega$ with reflection parameters on $\partial\Omega$ for each frequency, radars with their emitted spectrum, antenna gain, location, listening time
Result: Received radar spectra
Generate a triangular mesh from DEM using Delaunay triangulation;
Associate reflection parameters to the mesh;
Reinterpolation and possible surface subdivision scheme (optional);
for l **to** $NumberOfRadars$ **do**
  Select the facets element seen by the radar ($NumberOfPolys$);
  for $n0$ **to** $NumberOfPolys$ **do**
    Sierpinski subdivision ($NumberOfFacets$);
    for $n1$ **to** $NumberOfFacets$ **do**
      Compute geometrical term;
      for i **to** $NumberOfFrequencies$ **do**
        Compute phase integral term;
      end
    end
    Sum over $NumberOfFacets$;
  end
  Sum over $NumberOfPolys$;
  Post treatment if any;
  Save data;
end

Algorithm 1: An implementation for sounding radar experiment computation.

It is usually preferable to store the data without any post treatment. This allows multiple signal treatment algorithm to be performed with a single simulated scattered field.

4.4 EXAMPLES

Using the algorithm described previously, surface radar echoes have been computed for several instruments.
We illustrate results with LRS (see Figure 9) using the Lunar Orbiter Laser Altimeter instrument data (LOLA) with 128 pixels per degree to obtain surface topography. Subsurface permittivity was assumed to be a constant in the area. We furthermore assumed a single dipole antenna with a fixed orientation and used hamming windowing for the spectrum. Data are compressed in range (see [Ono and Oya, 2000; Kobayashi et al., 2002a]). The simulation is able to reconstruct radar signals accurately enough to reproduce the main structures. The real data seems to contain a diffuse signal which was not reproduce by the simulation. It is likely that this signal is due to surface/subsurface diffusion occurring at much smaller scales than the terrain resolution. Indeed, in our model we assumed Fresnel coefficients over each facet which does not account for any local diffusion effect.
We also present results for SHARAD instrument (see Figure 10) using the Mars Orbiter Laser Altimeter instrument data (MOLA) with 128 pixels per degree to obtain surface topography as well as results from an airborne instrument over sandy dunes (see Figure 11) with high resolution digital elevation model. Subsurface permittivity was assumed to be a constant over the areas in both cases. We furthermore assumed a single dipole antenna with a fixed orientation. We applied hamming windowing for visualization. Data are compressed in range. Although we are able to reproduce the main structures, results obtained with SHARAD instrument are clearly not as satisfying as the ones with LRS instru-

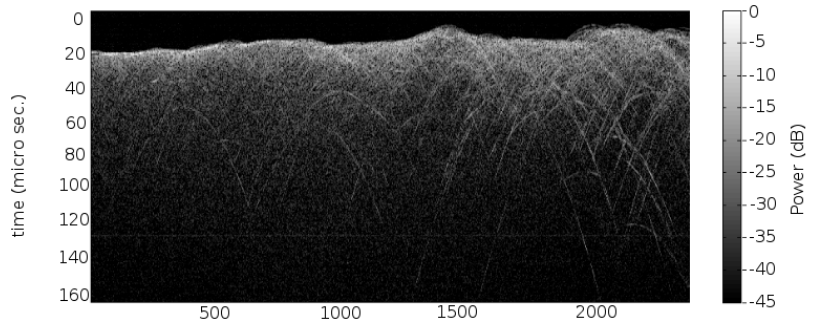

(a) Real data

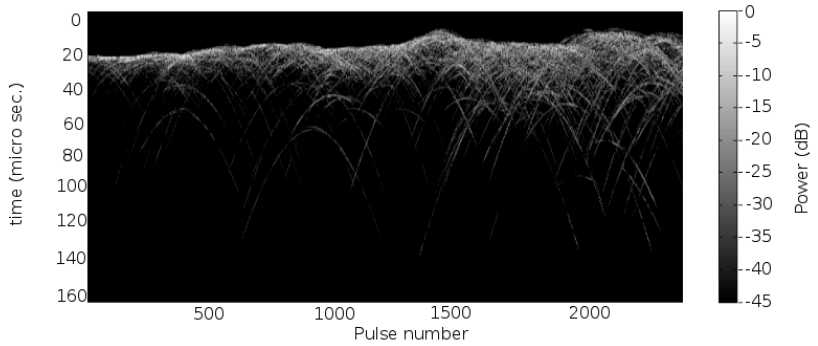

(b) Simulated data

Figure 9: Simulated radar surface echoes for LRS instrument. Color scales are in decibels.

ment. This can be explained by a coarser terrain resolution with regards to the signal wavelength as well as possible atmospheric effects and an overall smaller signal to noise ratio. Terrain resolution becomes the main limitation factor as the central frequency of the radar instrument increases to properly reproduce radar signals.

Results indicate a good match between simulations and observation data. The quality of the outputs depends on the validity of the approximations carried out through the previous sections. The far field approximation is straightforward (e.g. [Kong, 2000]) and will not be discussed here. The main limitation arises in the correctness of the surface description as a set of planar facet elements. In order for this assertion to be valid, the deviation from the true surface to the approximate set of facets should be less than a fraction of the radar wavelength. If not, error in the phase term will yield an incorrect assessment of the scattered field (see figure 8). A correct description of the surface at the wavelength of the probing signal must be used to properly simulate the scattered field. Furthermore, decoupling of facet elements is only valid within sufficiently flat areas. Indeed, if the boundary surface becomes more complex with regard to the topography (for instance high slopes or micro reflectors), multiple reflections will occur affecting the quality of the results (e.g. [Fung and Chan, 1971; Fung et al., 1992]). Practically, second reflections are often being neglected in planetary sounding radar due to acquisition geometries. However, this issue may arise on heavily cratered terrains or when using high frequencies as slopes tend to steepen at smaller terrain scales.

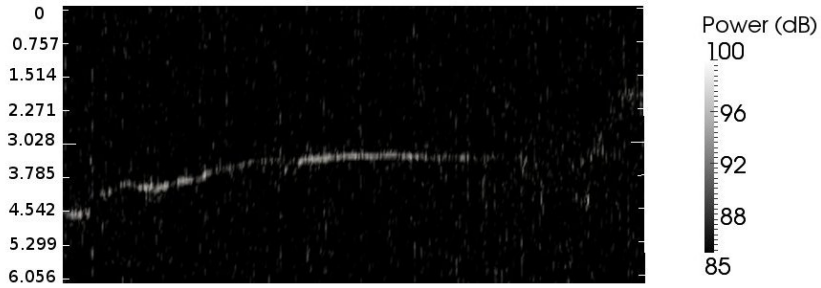

(a) Real data

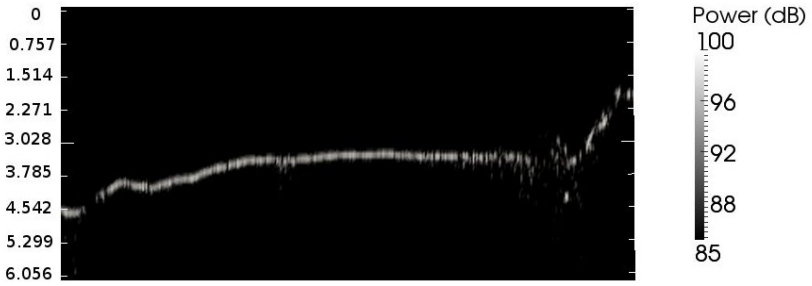

(b) Simulated data

Figure 10: Simulated radar surface echoes for SHARAD instrument (orbit 240301). The central frequency is 20MHz with a 10MHz bandwidth. Color scales are in decibels and time scale is in micro seconds.

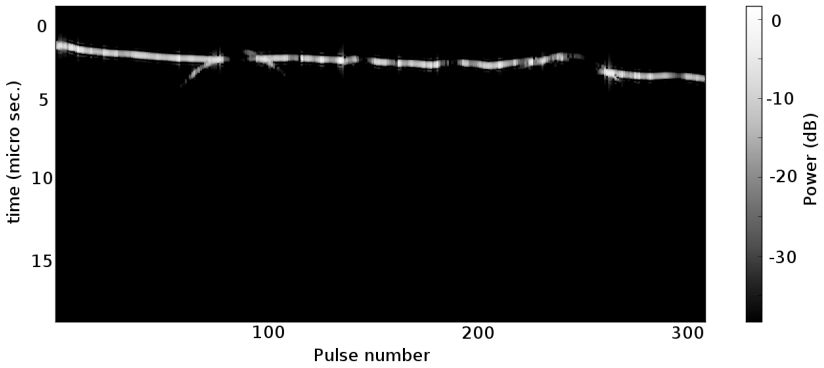

Figure 11: Simulated radar surface echoes for an airborne instrument. The central frequency is 50MHz with a 10MHz bandwidth. The altitude was taken as 1km. Color scales are in decibels.

Part III

AN INVERSE PROBLEM FORMULATION USING HUYGENS-FRESNEL'S PRINCIPLE

Huygens' principle naturally divides the problem in two subproblems with the interior of the volume (usually the upper medium or planetary atmospheric/ionospheric environment) and the exterior of the volume (usually planetary subsurface body). Materials of both media can be target parameters for the planetary sounding radar experiment. This section describes a novel approach to recover surface reflectivity parameters. It also discusses the possibility to use such a formulation to recover additional parameters.

5 RECOVERING REFLECTIVITY PARAMETERS

Back off man, I'm a scientist.

— Dr. Peter Venkman

From now on, we will assume the boundary surface $\partial\Omega$ to conform with the planetary surface, or in a more general sense to physically delimit two non identical media. This work was largely inspired by [Tarantola and Valette, 1982a; Tarantola, 1988, 2005] regarding the inverse problem theory. Following a point of view illustrated in [Tarantola and Valette, 1982b; Tarantola, 2005; Saintenoy and Tarantola, 2001], we postulate that the most general way to describe a *state of information* is to define a probability density over the parameter space. This point can be extensively discussed and has been shown to be inadapted for several problems (e.g. [Shafer, 1976; Dempster, 1967]). The use of imprecise probabilities in the inverse problem formulation would be a definitive improvement (e.g. [Baudrit and Dubois, 2006]) but requires an important work. The notion of state of information is central to formulate the inverse problem. The general inverse problem results in the combination of the observable parameters, the a priori information on model parameters, and the information on the physical correlations between observable parameters and model parameters information. Hence, we attempt at recovering posterior probability densities of reflectivity parameters. Inversion results presented in this work have been performed with synthetic radar data using the algorithm presented in section 4.

5.1 TOWARDS A LINEAR INVERSE PROBLEM

We propose here to describe an algorithm to recover reflectivity coefficients provided these coefficients only depend on the surface $\partial\Omega$ and not on the incident fields. The inversion scheme relies on a least-squares approach. The technique described allows to achieve the inversion of reflectivity parameters process a single step with reasonable computer resources.

Theory and implementation

Although Fresnel's coefficients R^{TE} and R^{TM} are not linear with regard to the incident field (see equation B.37), we can show that these coefficients can be linearized for monostatic set-ups. Carrying series expansions for these coefficients on the tangential component to the surface of the incident wavenumber $k_{\parallel,1}$ around zero, we find that first order coefficients are null for both R^{TE} and R^{TM},

$$R^{TE} = \frac{\mu_2\sqrt{\epsilon_1\mu_1} - \mu_1\sqrt{\epsilon_2\mu_2}}{\mu_2\sqrt{\epsilon_1\mu_1} + \mu_1\sqrt{\epsilon_2\mu_2}} + O\left(k_{\parallel,1}^2\right) \tag{5.1}$$

$$R^{TM} = \frac{\epsilon_2\sqrt{\epsilon_1\mu_1} - \epsilon_1\sqrt{\epsilon_2\mu_2}}{\epsilon_2\sqrt{\epsilon_1\mu_1} + \epsilon_1\sqrt{\epsilon_2\mu_2}} + O\left(k_{\parallel,1}^2\right) \tag{5.2}$$

Practically, angles of incidence in planetary sounding radar are close to zero in most experiment setups (i.e. MARSIS, SHARAD, LRS and RIME). Fresnel's reflection coefficients can thus be considered as independent from the incident field in planetary sounding. These mathematical considerations merely express the concept of bright spots, i.e. for a given position of the radar, only patches of

surface in quasi-geometrical optic reflection conditions contribute to the signal. In the monostatic setup, this requires the incident wave vector to be along the normals on these surface patches. We shall generalize this consideration and assume in this section that reflection parameters R_{TE}^{TE}, R_{TM}^{TE}, R_{TE}^{TM} and R_{TM}^{TM} defined in equations B.45 and B.46 are only frequency dependant. Making use of equations B.45 and B.46 in B.25 we obtain (see section B.4),

$$\begin{aligned}\mathbf{d}(\beta,\omega_0) = \sum_{\alpha\in I}\Bigg[\int_{\omega}\bar{\bar{\mathbf{C}}}^{\beta,\alpha}(\omega,\omega_0).\Bigg[\int_{\partial\Omega'}\bar{\bar{\mathbf{K}}}_e^{\alpha}(\mathbf{x}_0-\mathbf{x}',\omega,\omega_0).\\ \Bigg[\int_{\partial\Omega}\frac{i\,k\,e^{ik\left(\mathbf{x}+\hat{\mathbf{k}}_i\cdot\mathbf{x}_0\right)}}{4\pi x}.\left[\bar{\bar{\mathbf{I}}}-\hat{\mathbf{k}}_\mathbf{i}\hat{\mathbf{k}}_\mathbf{i}\right].2.\left(\hat{\mathbf{n}}\cdot\hat{\mathbf{k}}_i\right).\Big(\hat{\mathbf{q}}_i.\Big(R_{TE}^{TE}.(\hat{\mathbf{e}}_i\cdot\hat{\mathbf{q}}_i)+R_{TM}^{TE}.(\hat{\mathbf{e}}_i\cdot\hat{\mathbf{p}}_i)\Big)\\ -\hat{\mathbf{p}}_i.\Big(R_{TM}^{TM}.(\hat{\mathbf{e}}_i\cdot\hat{\mathbf{p}}_i)+R_{TE}^{TM}.(\hat{\mathbf{e}}_i\cdot\hat{\mathbf{q}}_i)\Big)\Big)d\sigma(\mathbf{x})\Bigg]d\sigma(\mathbf{x}')\Bigg]d\omega\Bigg]\end{aligned} \tag{5.3}$$

The previous equation highlights the linearity of measurements $\mathbf{d}^j$ with regard to the reflection parameters,

$$\begin{aligned}&d^i(\alpha,\omega) =\\ &\int_{\partial\Omega}f_{TE}^{TE,i}(\alpha,\omega,\mathbf{x}).R_{TE}^{TE}(\mathbf{x},\omega)d\sigma(\mathbf{x})\\ &+\int_{\partial\Omega}f_{TM}^{TE,i}(\alpha,\omega,\mathbf{x}).R_{TM}^{TE}(\mathbf{x},\omega)d\sigma(\mathbf{x})\\ &-\int_{\partial\Omega}f_{TE}^{TM,i}(\alpha,\omega,\mathbf{x}).R_{TE}^{TM}(\mathbf{x},\omega)d\sigma(\mathbf{x})\\ &-\int_{\partial\Omega}f_{TM}^{TM,i}(\alpha,\omega,\mathbf{x}).R_{TM}^{TM}(\mathbf{x},\omega)d\sigma(\mathbf{x})\end{aligned} \tag{5.4}$$

$d^i(\alpha,\omega)$ with $i\in\{1,2,...,k\}$ is the component of $\mathbf{d}(\alpha,\omega)\in\mathbb{C}^k$ in the data space and $\alpha\in I$ with $I\subset\mathbb{N}$. We recall that both model space $\mathbb{M}$ and data space $\mathbb{D}$ are assumed to be linear and that least-squares techniques arise (from a probabilistic point of view) when all the *input* probability densities are Gaussian. We assume that all functions under consideration (i.e. data components, forward operators, model parameters, etc.) belong to linear spaces,

$$\mathbf{d}=\mathbf{f}(\mathbf{m})=\mathbf{F}\mathbf{m} \tag{5.5}$$
$$\mathbf{F}=\{f_{TE}^{TE,i},f_{TM}^{TE,i},-f_{TE}^{TM,i},-f_{TM}^{TM,i}\} \tag{5.6}$$
$$\mathbf{m}=\{R_{TE}^{TE},R_{TM}^{TE},R_{TE}^{TM},R_{TM}^{TM}\} \tag{5.7}$$
$$\mathbf{d}=\{\mathbf{d}(\alpha,\omega)\}_{\alpha\in I} \tag{5.8}$$

Where $\mathbf{m}\in\mathbb{M}$ and $\mathbf{d}\in\mathbb{D}$ with $\mathbb{M}$ and $\mathbb{D}$ being the linear model and data space respectively. We let $\mathbf{d}_{obs}$ represent the observed data set and we provide a covariance operator $\mathbf{C}_D$ describing the data uncertainties. Furthermore, we assume the (unknown) model $\mathbf{m}$ is a sample of a known Gaussian probability density whose mean is $\mathbf{m}_{prior}$ and whose covariance matrix is $\mathbf{C}_M$. Hence, the probability densities $\rho_M(\mathbf{m})$ and $\rho_D(\mathbf{d})$ for the prior model density over the model space and for the data uncertainty over the data space respectively can be expressed as,

$$\rho_M(\mathbf{m}) = a_M.\exp\left(-\frac{1}{2}(\mathbf{m}-\mathbf{m}_{prior})^t\mathbf{C}_M^{-1}(\mathbf{m}-\mathbf{m}_{prior})\right) \tag{5.9}$$

$$\rho_D(\mathbf{d}) = a_D.\exp\left(-\frac{1}{2}(\mathbf{d}-\mathbf{d}_{obs})^t\mathbf{C}_D^{-1}(\mathbf{d}-\mathbf{d}_{obs})\right) \tag{5.10}$$

Where $\left(\mathbf{C}_M^{-1}(\mathbf{m}-\mathbf{m}_{prior})\right)^t$ and $\left(\mathbf{C}_D^{-1}(\mathbf{d}-\mathbf{d}_{obs})\right)^t$ are elements of dual model and data spaces respectively and a_M and a_D are a normalization constants. Covariance operators allow to define scalar products over model and data spaces thus providing a notion of distance. The posterior probability density $\sigma_M(\mathbf{m})$ over the model space can then be derived using equations 5.5 and 5.9,

$$\sigma_M(\mathbf{m}) = a_M.\exp\left(-L(\mathbf{m})\right) \tag{5.11}$$

$$\begin{aligned} 2.L(\mathbf{m}) &= \|\mathbf{f}(\mathbf{m})-\mathbf{d}_{obs}\|_D^2 + \|\mathbf{m}-\mathbf{m}_{prior}\|_M^2 \\ &= (\mathbf{f}(\mathbf{m})-\mathbf{d}_{obs})^t\mathbf{C}_D^{-1}(\mathbf{f}(\mathbf{m})-\mathbf{d}_{obs}) + (\mathbf{m}-\mathbf{m}_{prior})^t\mathbf{C}_M^{-1}(\mathbf{m}-\mathbf{m}_{prior}) \end{aligned} \tag{5.12}$$

The best model (in the least-squares sense) is defined by the minimization of the misfit function $L(\mathbf{m})$. This amounts to a minimization of a squared normed function as clearly illustrated in the previous equation. Least-squares techniques are also referred to as l_2-norm minimization techniques. As least-squares techniques are related in terms of probability to Gaussian probability densities, these techniques lack of robustness. In practice the presence of few outliers in the data set is sufficient to introduce a bias in the posterior probability density estimation. However, least-squares remain popular as they lead to easy computation at the cost of a careful understanding of the data set. Since $\mathbf{f}(\mathbf{m}) = \mathbf{Fm}$ (linear forward operator), the posterior probability density $\sigma_M(\mathbf{m})$ is a Gaussian probability density,

$$\sigma_M(\mathbf{m}) = a_M.\exp\left(-\frac{1}{2}(\mathbf{m}-\tilde{\mathbf{m}})^t\tilde{\mathbf{C}}_M^{-1}(\mathbf{m}-\tilde{\mathbf{m}})\right) \tag{5.13}$$

$$\tilde{\mathbf{m}} = \mathbf{m}_{prior} + \mathbf{C}_M\mathbf{F}^t\left(\mathbf{F}\mathbf{C}_M\mathbf{F}^t + \mathbf{C}_D\right)^{-1}\left(\mathbf{d}_{obs} - \mathbf{F}\mathbf{m}_{prior}\right) \tag{5.14}$$

$$\tilde{\mathbf{C}}_M = \mathbf{C}_M - \mathbf{C}_M\mathbf{F}^t\left(\mathbf{F}\mathbf{C}_M\mathbf{F}^t + \mathbf{C}_D\right)^{-1}\mathbf{F}\mathbf{C}_M \tag{5.15}$$

The best model is thus $\tilde{\mathbf{m}}$ in the least-squares sense. However, it does not fully characterize the inverse problem as the solution to the problem must be thought in terms of probability density. The problem can be further simplified if we discard coupling parameters R_{TM}^{TE} and R_{TE}^{TM} and if we set $R = R_{TE}^{TE} = -R_{TM}^{M}$. It amounts to working with Fresnel's coefficients at normal incidence. This assumption is usually quite realistic in planetary sounding radar and will be used from now on,

$$\mathbf{d} = \mathbf{f}(\mathbf{m}) = \mathbf{Fm} \tag{5.16}$$

$$\mathbf{m} = \{\mathbf{R}\} \tag{5.17}$$

$$\|\mathbf{f}(\mathbf{m})-\mathbf{d}_{obs}\|_D^2 + \|\mathbf{m}-\mathbf{m}_{prior}\|_M^2 = \|\mathbf{f}(\mathbf{m})-\mathbf{d}_{obs}\|_D^2 + \|\mathbf{R}-\mathbf{R}_{prior}\|_R^2 \tag{5.18}$$

In the following equations, the symbol $*$ denotes complex conjugate (i.e. $a*$ is

the complex conjugate of a). We now define the duality product $\langle \cdot, \cdot \rangle$ of the parameter set and of the data set respectively,

$$\left\langle \hat{\mathbf{R}}_1, \mathbf{R}_2 \right\rangle = \hat{\mathbf{R}}_1^t \mathbf{R}_2 = \int_B \int_{\partial\Omega} \hat{R}_1^*(\mathbf{x}, \omega).R_2(\mathbf{x}, \omega) d\sigma(\mathbf{x}) d\omega \tag{5.19}$$

$$\left\langle \hat{\mathbf{d}}_1, \mathbf{d}_2 \right\rangle = \sum_{i=1}^{k} \sum_{\alpha \in I} \int_B \hat{d}_1^{*i}(\alpha, \omega).d_2^i(\alpha, \omega) d\omega \tag{5.20}$$

Where quantities with a hat denote elements of the dual spaces. $B \in \mathbb{R}$ denotes the domain on which the pulsation integral has to be carried out. Practically, this corresponds to the bandwidth of the signal. We introduce the weighting operators $\mathbf{W}_D$ and $\mathbf{W}_M$ which are defined as the inverse of the covariance operators $\mathbf{C}_D$ and $\mathbf{C}_M$ respectively. The scalar products $(\cdot, \cdot)$ on both model and data spaces are given by,

$$\begin{gathered}(\mathbf{R}_1, \mathbf{R}_2) = \langle \mathbf{W}_M \mathbf{R}_1, \mathbf{R}_2 \rangle = \\ \int_B d\omega' \int_{\partial\Omega} d\sigma(\mathbf{x}) \int_B d\omega \int_{\partial\Omega} d\sigma(\mathbf{x}') R_1^*(\mathbf{x}, \omega).W_M(\mathbf{x}, \omega; \mathbf{x}', \omega').R_2(\mathbf{x}', \omega')\end{gathered} \tag{5.21}$$

$$\begin{gathered}(\mathbf{d}_1, \mathbf{d}_2) = \langle \mathbf{W}_D \mathbf{d}_1, \mathbf{d}_2 \rangle = \\ \sum_{i=1}^{k} \sum_{\alpha \in I} \int_B d\omega \sum_{j=1}^{k} \sum_{\beta \in I} \int_B d\omega' d_1^{*i}(\alpha, \omega).W_D^{i,j}(\alpha, \omega; \beta, \omega').d_2^j(\beta, \omega')\end{gathered} \tag{5.22}$$

We can rewrite the misfit function L using parameter components explicitly,

$$\begin{aligned}&2.L(\mathbf{m}) = \\ &\sum_{i=1}^{k} \sum_{j=1}^{k} \sum_{\alpha \in I} \sum_{\beta \in I} \int_B d\omega \int_B d\omega' \delta d^{*i}(\alpha, \omega).W_D^{i,j}(\alpha, \omega; \beta, \omega').\delta d^j(\beta, \omega') \\ &+ \int_B d\omega \int_B d\omega' \int_{\partial\Omega} d\sigma(\mathbf{x}) \int_{\partial\Omega} d\sigma(\mathbf{x}') \delta R^*(\mathbf{x}, \omega).W_M(\mathbf{x}, \omega; \mathbf{x}', \omega').\delta R(\mathbf{x}', \omega')\end{aligned} \tag{5.23}$$

Using previous notations,the transpose operator $\mathbf{F}^t$ is defined throughout this manuscript by the following identity (for any $\hat{\mathbf{d}}$ and $\mathbf{m}$),

$$\langle \hat{\mathbf{d}}, \mathbf{F}\mathbf{m} \rangle = \langle \mathbf{F}^t \hat{\mathbf{d}}, \mathbf{m} \rangle \tag{5.24}$$

Practically, we can detail the expression of $\tilde{\mathbf{m}}$ ($*$ denotes the complex conjugate),

$$\begin{gathered}\left[\left[\mathbf{C}_M \mathbf{F}^t \right] \delta \hat{\mathbf{d}} \right] (\mathbf{x}', \omega') = \\ \int_{\partial\Omega} d\sigma(\mathbf{x}) \sum_{\beta \in I} \sum_{i=1}^{k} \int_B d\omega C_M(\sigma(\mathbf{x}), \omega; \sigma(\mathbf{x}'), \omega').\delta \hat{d}^i(\beta, \omega).f^{*i}(\beta, \omega, \mathbf{x})\end{gathered} \tag{5.25}$$

$$\begin{gathered}\left[\left[\mathbf{C}_D + \mathbf{F}\mathbf{C}_M\mathbf{F}^t \right] \delta \hat{\mathbf{d}} \right]^i (\alpha, \omega') = \\ \sum_{j=1}^{k} \sum_{\beta \in I} \int_B d\omega C_D^{i,j}(\beta, \omega; \alpha, \omega').\delta \hat{d}^j(\beta, \omega) + \\ \int_{\partial\Omega} d\sigma(\mathbf{x}') \int_{\partial\Omega} d\sigma(\mathbf{x}) \int_B d\omega \sum_{\beta \in I} \sum_{j=1}^{k} f^i(\alpha, \omega', \mathbf{x}').C_M(\mathbf{x}, \omega; \mathbf{x}', \omega').f^{*j}(\beta, \omega, \mathbf{x}).\delta \hat{d}^j(\beta, \omega)\end{gathered}$$

(5.26)

Note: The equations are written with R but they can be generalized setting $R = \{R_{TE}^{TE}, R_{TM}^{TE}, R_{TE}^{TM}, R_{TM}^{TM}\}$ and using 4×4 matrix notations for covariance and weighting operators as well as vector notations for R.

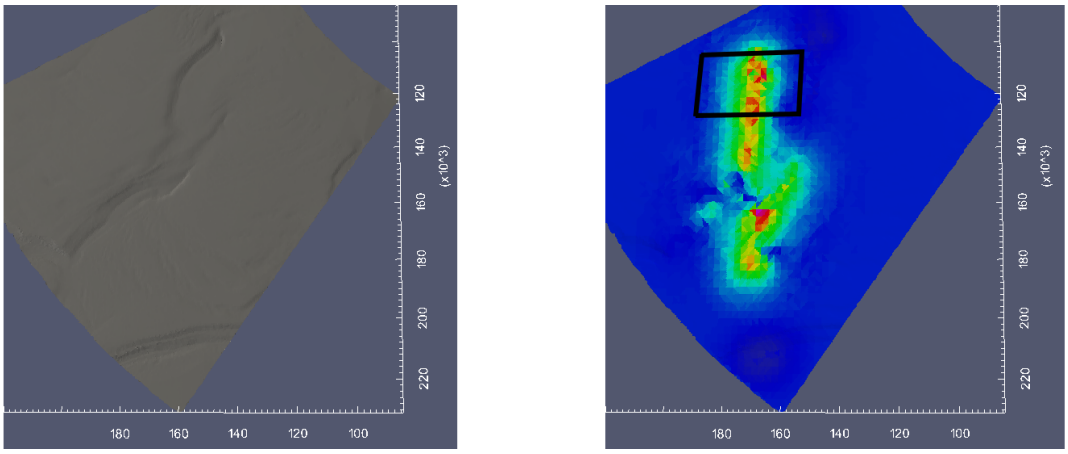

(a) Surface topography

(b) Exemple of reflectivity map

(c) Zoom on the distribution

Figure 12: Example of surface partition. The color scale indicate the parameter values over surface areas. Each surface partition (or surface patch) is assigned a constant parameter value and each surface partition contains several meshes. The number of meshes can vary from one surface partition to another.

Discretizing the parameter and data spaces, the set of equations can be interpreted as matrix systems which can be solved using standard methods of linear algebra. In order to achieve this, we partition $\partial\Omega$ into $N_e \in \mathbb{N}$ elementary surface patches $\partial\Omega_{n=[1,N_e]}$. The partition of $\partial\Omega$ is not linked to the meshing of the surface topography described in section 4 (see figure 12) and can be thus adapted with regard to the size of the problem and to the desired resolution. Surface integrals are rewritten as discrete sums of elements with constant reflectivity parameters over each patch. Furthermore, the band B is discretized as well as data are sampled over a finite number of frequencies N_f,

$$f_n^i(\beta, \omega_k) = \int_{\partial\Omega_n} d\sigma(\mathbf{x}) f^i(\beta, \omega_k, \mathbf{x}) \tag{5.27}$$

$$\left[\mathbf{C}_M\mathbf{F}^t\right]^i(\alpha,\omega_r) = \sum_{n=1}^{N_e}\sum_{\beta\in I}\sum_{i=1}^{k}\sum_{l=1}^{N_f} C_M(\mathbf{x}_n,\omega_l;\mathbf{x}_p,\omega_r).\delta\hat{d}^i(\beta,\omega_l).f_n^{*i}(\beta,\omega_l) \quad (5.28)$$

$$\begin{aligned}\left[\left[\mathbf{C}_D+\mathbf{F}\mathbf{C}_M\mathbf{F}^t\right]\delta\hat{\mathbf{d}}\right]^i(\alpha,\omega_k) = \\ \sum_{j=1}^{k}\sum_{\beta\in I}\sum_{l=1}^{N_f} C_D^{i,j}(\beta,\omega_l;\alpha,\omega_k).\delta\hat{d}^j(\beta,\omega_l)+ \\ \sum_{p=1}^{N_e}\sum_{n=1}^{N_e}\sum_{l=1}^{N_f}\sum_{\beta\in I}\sum_{j=1}^{k} f_p^i(\alpha,\omega_k).C_M(\mathbf{x}_n,\omega_l;\mathbf{x}_p,\omega_k).f_n^{*j}(\beta,\omega_l).\delta\hat{d}^j(\beta,\omega_l)\end{aligned} \quad (5.29)$$

$\mathbf{x}_n$ and $\mathbf{x}_p$ designate central points of surface patches $\partial\Omega_n$ and $\partial\Omega_p$ respectively. Of course, dimensions of constant reflectivity surface patches must be much smaller than the correlation length of the prior covariance function. Practically we have ensured that patches extension were at maximum one fourth of the correlation length. To enhance computation efficiency we have computed the forward problem operator $\mathbf{F}$ prior to the inversion step and to store it to avoid computing it multiple times. Similarly, the covariance matrix should be computed priorly and stored. It is also worth noting that the matrix $\left[\mathbf{F}\mathbf{C}_M\mathbf{F}^t+\mathbf{C}_D\right]$ (see equation 5.29) is a sparse matrix. It is thus desirable to identify – prior to computation – which pulses are coupled. Practically, detecting coupled pulses can be performed through a comparison of $\mathbf{C}_M\mathbf{F}^t$ matrix for each pulse. Should non-null elements of the matrices overlap, pulses are considered to be coupled, otherwise they are not.

Data: Radar measurements in frequency domain (spectra) and prior model (surface topography $\partial\Omega$ with reflection parameters on $\partial\Omega$ for each frequency N_f)
Result: Inversion of surface parameters
Load prior model and generate parameter grid $\mathbf{m}_{prior}$;
Load observation data $\mathbf{d}_{obs}$;
Compute covariance matrix $\mathbf{C}_M$;
Compute direct operator $\mathbf{F} = \{F^i\}_{i\in N_f}$;
Identification of coupled pulses;
for i **to** N_f **do**
  Compute prior data $\mathbf{d}^i = \mathbf{F}^i\mathbf{m}^i_{prior}$;
  Compute residuals $\delta\mathbf{d}^i = \mathbf{d}^i_{obs} - \mathbf{d}^i$;
  Compute matrix $\mathbf{T} = \left[\mathbf{F}^i\mathbf{C}_M\mathbf{F}^{i,t}+\mathbf{C}_D\right]$;
  Solve $\delta\mathbf{d}^i = \mathbf{T}^i\delta\hat{\mathbf{d}}^i$;
  Apply transpose operator and covariance operator $\delta\mathbf{m}^i = \mathbf{C}_M\mathbf{F}^{i,t}\delta\hat{\mathbf{d}}^i$;
  Update model $\tilde{\mathbf{m}}^i = \mathbf{m}^i_{prior} + \delta\mathbf{m}^i$;
end

Algorithm 2: An implementation for the linear inverse problem. Superscripts denote the i^{th} frequency.

From a probabilistic point of view, the linearization proposed in this section might not be fully satisfactory as probability distributions associated to model parameters are not necessarily Gaussian. For instance, when working with Fresnel's coefficients, parameter amplitudes are bounded which is not compatible with Gaussian distributions.

For the sake of completeness, I shall briefly discuss here how the previous set of equations relates to the work described in [Mouginot et al., 2010]. The technique proposed in this paper involves a constant reflectivity for each experiment (or *pulse*) α,

$$R_{TE}^{TE}(\mathbf{x},\omega) = R(\alpha) \tag{5.30}$$
$$R_{TE}^{TM}(\mathbf{x},\omega) = 0 \tag{5.31}$$
$$R_{TM}^{TE}(\mathbf{x},\omega) = 0 \tag{5.32}$$
$$R_{TM}^{TM}(\mathbf{x},\omega) = -R(\alpha) \tag{5.33}$$

R denotes here the scalar value reflectivity parameter constant for each radar measurement. Furthermore, the analysis is conducted within the time domain with the envelop of the signal. Consequently, we rewrite the forward problem,

$$d(\alpha,t) = |R(\alpha)| \cdot \left| \int_{\partial\Omega} \mathfrak{F}\left(f_{TE}^{TE,i}(\alpha,\omega,\mathbf{x}) + f_{TM}^{TM,i}(\alpha,\omega,\mathbf{x}) \right) d\sigma(\mathbf{x}) \right| \tag{5.34}$$

$\mathfrak{F}$ hereby represents the Fourier transform operator of the baseband signal (i.e. signal spectrum centred around zero) and $t \in \mathbb{R}$ the time variable. This approach is much less restrictive than it may appear. Indeed, the quasi geometrical optic conditions for scattered echoes result in a weak coupling of pulse-to-pulse radar acquisitions. Practically, this means pulses *too much distant* from one to another will not have their respective effective footprints overlapping. We define here the effective footprint as the portion of the surface which effectively contributes to the radar echo. Practically, the effective footprint is a set of surface patches in quasi geometrical optic conditions with regard to the radar location. These patches are sometimes referred to as bright spots in the literature (e.g. [Ostrovitianov and Basalov, 1985]). In the case of a planar surface, it corresponds to the Fresnel zone located directly below the spacecraft. The maximum distance from one pulse to another is roughly the diameter of the Fresnel zone radius for common radar orbit geometries (i.e. orbit parallel to the planetary body surface). Hence, when selecting acquisition points sufficiently spaced from one another, acquisitions can be regarded as decoupled with regard to the reflectivity parameter if we assume very little (i.e. smaller than Fresnel zone radius) spatial correlation for the reflectivity. Put differently, two radar positions do not see the same surface patches. This approach yields a very fast inversion process. Overall, the work performed in [Mouginot et al., 2010] is a special case of what is being presented here where the correlation functions $\mathbf{C}_M$ and $\mathbf{C}_D$ are assumed to have null off-diagonal elements.

Results

We shall now discuss some results obtained with the previous algorithm. Inversion results presented in this work have been performed with synthetic radar data using the algorithm presented in section 4. Figure 13 displays results obtained with synthetic radar data (noise free). A single frequency at 15 MHz for each radar measurements on the orbit track (100 acquisition points equally spaced along the orbit track) was used to perform the inversion. The targeted surface was set to have a constant reflectivity of 0.5. The prior model surface topography was the same as the targeted surface (i.e. identical meshing) and the prior reflectivity was set to be constant of the surface at 0.2. The prior standard deviation was set to 0.3 with a 5km correlation length. The posterior standard deviation allows to assess the resolved areas. The resolved areas combine the

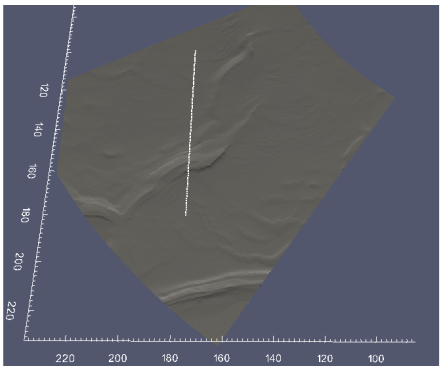

(a) Orbit track

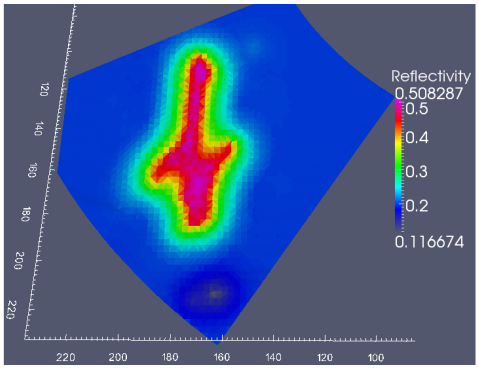

(b) Posterior mean

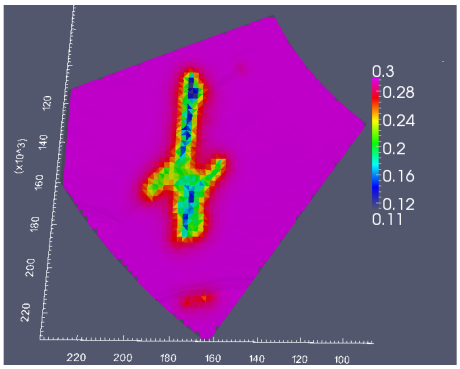

(c) Posterior standard deviation

Figure 13: Linear inversion of surface reflectivity coefficients with a single frequency from an orbit portion (100 acquisition points). The prior reflectivity was set to 0.2 (constant over the surface), the prior standard deviation set to 0.3 and the correlation length was set to 5km. The scales are in kilometers. The target surface has a constant reflectivity of 0.5.

probed areas as well as the correlated areas from the a priori covariance operator $\mathbf{C}_M$. It also provides an estimation of the resulting uncertainties around the *best model*. Practically, the posterior standard deviation displayed is merely the square root of the diagonal elements of the posterior covariance operator given in equation 5.13. With regard to the resolved areas, the *best model* (posterior mean) matches the expected output of the inversion as it recovers the true reflectivity value within the resolved areas.

In order to assess the stability of the algorithm, we have conducted inversion with perturbed surface (see figures 14 and 15) and with uncorrelated noise (see figure 16). Figure 14 highlights the effect of surface topography on surface reflectivity inversion. For this purpose, an inversion was run with the original surface topography (i.e. identical meshing) – which is referred to in figure 14 as high resolution – and a second inversion was run on a modified surface where the topography resolution was decreased, inducing a slightly modified surface shape – which is referred to in figure 14 as high resolution. The targeted surface had a constant reflectivity coefficients set to 0.5. The prior reflectivity model was set to 0.2 (constant over the surface), the prior v set to 0.3 with a 5km correlation length. Ten frequencies in the range 15-25MHz for each radar measurements on the orbit track (100 acquisition points equally spaced along the orbit track) were used to perform the inversion. Results indicate a very good estimation over all resolved areas for the high resolution model and a poor estimation with the low resolution model where the surface topography displays important curvatures. Indeed, in this area the low resolution surface matches poorly the original surface with important discontinuities in the surface normal (diffraction effects),

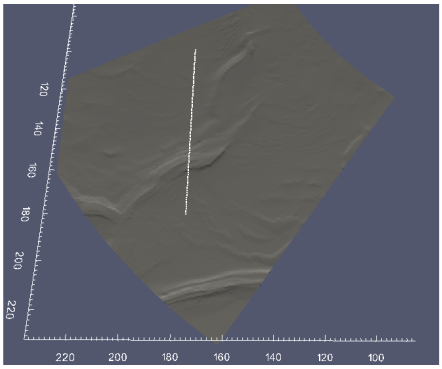

(a) Orbit track

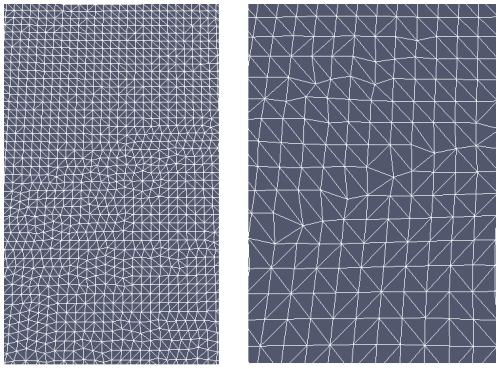

(b) Mesh resolution comparison

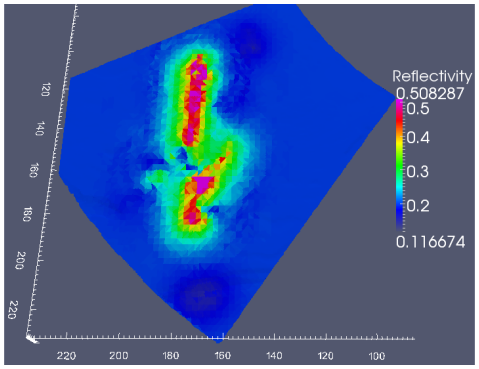

(c) Posterior mean obtained with low resolution surface model

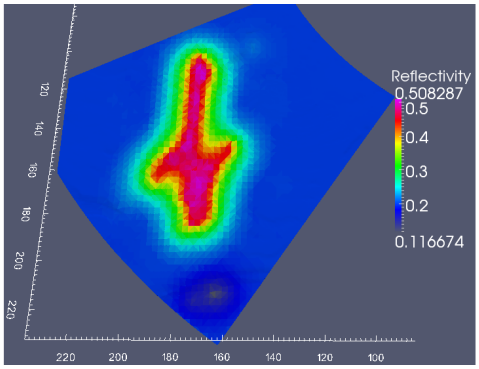

(d) Posterior mean obtained with high resolution surface model

Figure 14: Linear inversion of constant surface reflectivity coefficients set to 0.5 with frequencies in the range 15-25 MHz from an orbit portion (100 acquisition points) with a high resolution surface model and a low resolution surface model. The prior reflectivity was set to 0.2 (constant over the surface), the prior standard deviation set to 0.3 and the correlation length was set to 5km. The scales are in kilometers. Reflectivity data represent posterior means.

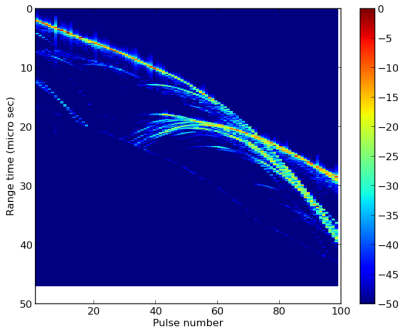

(a) Radar data obtained with low resolution surface model

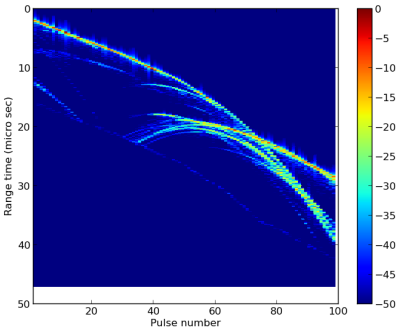

(b) Radar data obtained with high resolution surface model

Figure 15: Radar echo power measurements obtained for the same orbit track with different surface resolutions (see figure 14) and constant surface reflectivity. The color scale is in decibels. The time scale is in micro seconds and the x axis represents the pulse number along the orbit track. The radar band used is 15-25 MHz (SHARAD-like instrument).

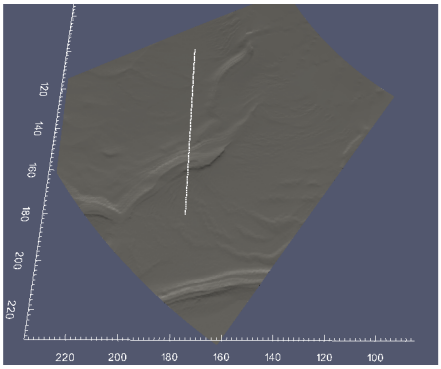

(a) Orbit track

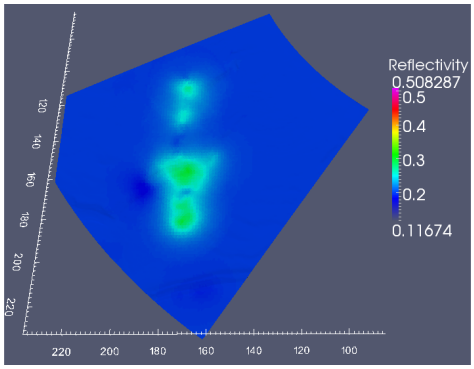

(b) Posterior mean

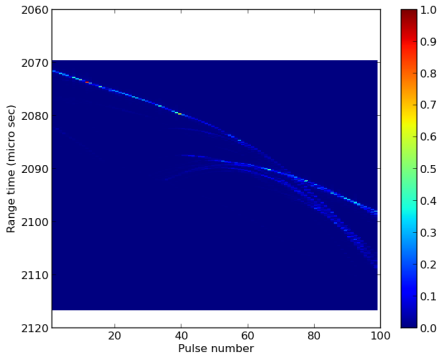

(c) Radar echo (no noise)

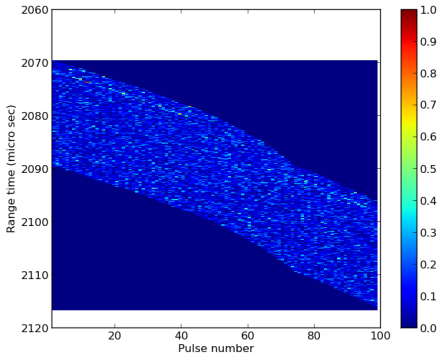

(d) Radar echo (with noise)

Figure 16: Linear inversion of constant surface reflectivity coefficients. The setup used is identical to the one described in figure 14. Noise was added to the observed data with a 10 dB signal-to-noise ratio.

thus radar echoes cannot be reproduced accurately (see figure 15). On the other hand, although the meshing is different over the flatter areas, the reflectivity estimation are still quite accurate for both the high resolution and low resolution. High resolution model allows to recover reflectivity value very much like in figure 13 since the mesh used is the same as the one used to produce the synthetic observed data. Thus figure 14 highlights the sensitivity of the inversion with regard to the quality of the surface description. This sensitivity is one of the main drawback of the approach presented throughout this work and for this reason it is often desirable to jointly inverse the surface topography to properly assess geophysical parameters (see section 6). However, since inaccurate surface description induces complex reflectivity coefficients, it should allow to detect areas where the approximation is not adapted. Figure 16 displays results obtained with synthetic radar data on which an uncorrelated Gaussian noise was added (signal to noise ratio of approximately 10 dB). Ten frequencies in the range 15-25 MHz for each radar measurements on the orbit track (100 acquisition points equally spaced along the orbit track) were used to perform the inversion. The targeted surface was set to have a constant reflectivity of 0.5. The prior model surface topography was the same as the targeted surface (i.e. identical meshing) and the prior reflectivity was set to be constant of the surface at 0.2. The prior standard deviation was set to 0.3 with a 5km correlation length and data uncertainties where matched to the noise level (i.e. high uncertainties on the recorded data). The posterior mean is highly impacted by the noise due to the lack of data with regard to the high level of noise (i.e. lack of information). Although a clear trend appear towards the true reflectivity values, the posterior variances remain

important which induces high posterior uncertainties. Increasing the amount of data over the area would provide a better estimation of the surface reflectivity. This can be done through an increase of the number of frequencies used in the band 15-25 MHz and through an increase of the number of acquisition points along the orbit track. However, one must keep in mind that an additional amount of data will increase the computation time.

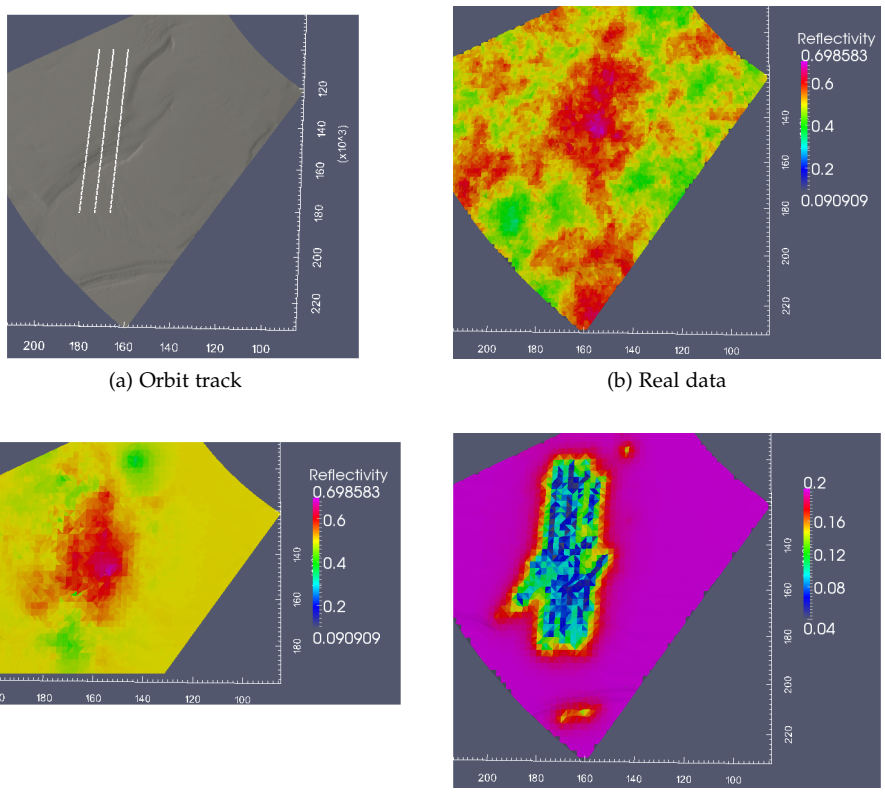

(a) Orbit track

(b) Real data

(c) Posterior mean

(d) Posterior variance

Figure 17: Inversion of surface reflectivity coefficients with a single frequency from an orbit portion (100 acquisition points per orbit track). The prior reflectivity was set to 0.5 (constant over the surface), the prior standard deviation set to 0.2 and the correlation length was set to 5km. The scales are in kilometers.

Figures 17 and 18 provide an insight on the capabilities of surface reflectivity estimation with non constant reflectivity. In both cases, a single frequency at 15 MHz for each radar measurements on the orbit tracks (100 acquisition points equally spaced along each orbit track) was used to perform the inversion. The targeted surface was set to have non-constant reflectivity and was identical in both cases. The prior model surface topography was the same as the targeted surface (i.e. identical meshing) and the prior reflectivity was set to be constant of the surface at 0.5 in both figure 17 and 18. The prior standard deviation was set to 0.2 with a 5km correlation length. Very much like in the case of constant reflectivity targets, the algorithm allows to estimate the reflectivity values in resolved areas provided the surface model matches the real surface. Interestingly, the figures also highlight the possibility to use several orbit tracks over an area to better assess surface properties. The joint inversion of several orbit tracks offer perspectives for high resolution imaging of surface properties. One can

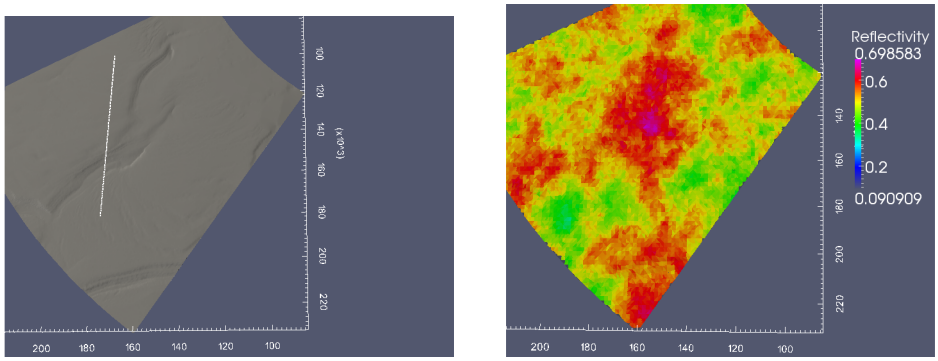

(a) Orbit track (b) Real data

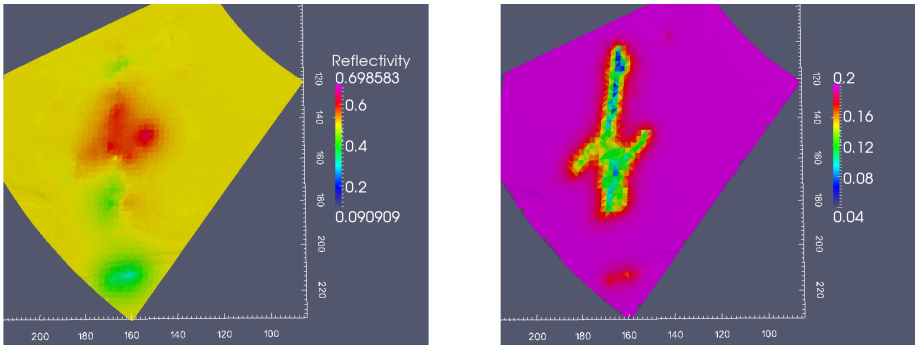

(c) Posterior mean (d) Posterior variance

Figure 18: Inversion of surface reflectivity coefficients with a single frequency from an orbit portion (100 acquisition points). The prior reflectivity was set to 0.5 (constant over the surface), the prior standard deviation set to 0.2 and the correlation length was set to 5km. The scales are in kilometers.

even imagine to use measurements from different radar instruments to conduct surface parameters estimation (for instance MARSIS and SHARAD).

5.2 TACKLING NON-LINEAR REFLECTIVITY PARAMETERS WITH AN ITERATIVE SCHEME

The independence of reflectivity parameters with regard to the incident wave field may be inappropriate and the forward problem cannot be linearized. I detail in this section an optimization scheme (also refer to as *gradient method*) to recover reflectivity parameters through parametrization. The general inverse problem in the least-squares approach dealing with non-linear functional inverse problem is widely discussed in the literature (e.g. [Tarantola, 2005]).

Theory and implementation

Suppose we can express γ_0^E, γ_1^E, γ_0^H and γ_1^H in equations B.35 and B.36 as functions of a limited set of N *unknown* parameters $\mathbf{m} = \{m^l(\mathbf{x}, \omega)\}_{l \in N}$ with $N \in \mathbb{N}$ that characterize local surface properties. $m^l(\mathbf{x}, \omega) \in \mathbb{R}$ denote the local coordinates of $\mathbf{m}$. The previous section is then a special case where $N = 8$ (both real and imaginary parts) and $\mathbf{m} = \{R_{TE}^{TE}, R_{TM}^{TE}, R_{TE}^{TM}, R_{TM}^{TM}\}$,

$$\gamma_0^E = E_i(\mathbf{x}).\Big[\,(\hat{\mathbf{e}}_i \cdot \hat{\mathbf{q}}_i)\,.\left(1 + R_{TE}^{TE}\right) + (\hat{\mathbf{e}}_i \cdot \hat{\mathbf{p}}_i)\,.R_{TM}^{TE}\Big] \tag{5.35}$$

$$\gamma_1^E = E_i(\mathbf{x}).\left(\hat{\mathbf{n}} \cdot \hat{\mathbf{k}}_i\right).\Big[\,(\hat{\mathbf{e}}_i \cdot \hat{\mathbf{p}}_i)\,.\left(1 - R_{TM}^{TM}\right) - (\hat{\mathbf{e}}_i \cdot \hat{\mathbf{q}}_i)\,.R_{TE}^{TM}\Big] \tag{5.36}$$

$$\gamma_0^H = \frac{1}{\eta}.E_i(\mathbf{x}).\Big[\,(\hat{\mathbf{e}}_i \cdot \hat{\mathbf{p}}_i)\,.\left(1 + R_{TM}^{TM}\right) + (\hat{\mathbf{e}}_i \cdot \hat{\mathbf{q}}_i)\,.R_{TE}^{TM}\Big] \tag{5.37}$$

$$\gamma_1^H = -\frac{1}{\eta}.E_i(\mathbf{x}).\left(\hat{\mathbf{n}} \cdot \hat{\mathbf{k}}_i\right).\Big[\,(\hat{\mathbf{e}}_i \cdot \hat{\mathbf{q}}_i)\,.\left(1 - R_{TE}^{TE}\right) - (\hat{\mathbf{e}}_i \cdot \hat{\mathbf{p}}_i)\,.R_{TM}^{TE}\Big] \tag{5.38}$$

In this special case γ_0^E, γ_1^E, γ_0^H and γ_1^H are linear with regard to $\mathbf{m}$. Similarly, using equations B.37 in equations B.43 and B.44 yields,

$$\gamma_0^E = E_i(\mathbf{x}).\Big[\,(\hat{\mathbf{e}}_i \cdot \hat{\mathbf{q}}_i)\,.\left(1 + \frac{1 - p_{1,2}^{TE}}{1 + p_{1,2}^{TE}}\right)\Big] \tag{5.39}$$

$$\gamma_1^E = E_i(\mathbf{x}).\left(\hat{\mathbf{n}} \cdot \hat{\mathbf{k}}_i\right).\Big[\,(\hat{\mathbf{e}}_i \cdot \hat{\mathbf{p}}_i)\,.\left(1 - \frac{1 - p_{1,2}^{TM}}{1 + p_{1,2}^{TM}}\right)\Big] \tag{5.40}$$

$$\gamma_0^H = \frac{1}{\eta}.E_i(\mathbf{x}).\Big[\,(\hat{\mathbf{e}}_i \cdot \hat{\mathbf{p}}_i)\,.\left(1 + \frac{1 - p_{1,2}^{TM}}{1 + p_{1,2}^{TM}}\right)\Big] \tag{5.41}$$

$$\gamma_1^H = -\frac{1}{\eta}.E_i(\mathbf{x}).\left(\hat{\mathbf{n}} \cdot \hat{\mathbf{k}}_i\right).\Big[\,(\hat{\mathbf{e}}_i \cdot \hat{\mathbf{q}}_i)\,.\left(1 - \frac{1 - p_{1,2}^{TE}}{1 + p_{1,2}^{TE}}\right)\Big] \tag{5.42}$$

with,

$$p_{1,2}^{TE} = \frac{\mu_1 k_{\perp,2}}{\mu_2 k_{\perp,1}} \tag{5.43}$$

$$p_{1,2}^{TM} = \frac{\epsilon_1 k_{\perp,2}}{\epsilon_2 k_{\perp,1}} \tag{5.44}$$

$$k_{\parallel,1}^2 + k_{\perp,1}^2 = \omega^2 \mu_1 \epsilon_1 \tag{5.45}$$

$$k_{\parallel,1}^2 + k_{\perp,2}^2 = \omega^2 \mu_2 \epsilon_2 \tag{5.46}$$

Where μ_1 and μ_2 are the upper and lower medium magnetic permeability while ϵ_1 and ϵ_2 are the upper and lower medium electric permittivity respectively. $k_{\parallel,i}$ and $k_{\perp,i}$ with $i = \{1,2\}$ are the components of the wave vector $\mathbf{k}$ in the plane of incidence and normal to the plane of incidence respectively. Setting $N = 2$ and $\mathbf{m} = \{\epsilon_2, \mu_2\}$, we recognize a non-linear example of parametrization of functions γ_0^E, γ_1^E, γ_0^H and γ_1^H. It is usually preferable to work with physical invariant quantities $\log(\epsilon_2/\epsilon_0)$ and $\log(\mu_2/\mu_0)$ as there is no reason that results should change whether we study the inverse of these parameters or linear related parameters.

The non-linear inverse problem does not require to work with linear spaces. For the sake of genericness, we let $\mathfrak{M}$ be the model manifold and $\mathbf{m} = \{m^l\}$ be one of its points whereby $\{m^l\}_{l\in N}$ are the coordinates of the point. We write $\left(\frac{\partial \mathbf{E}_\parallel}{\partial m^l}\right)_{l\in N}$ and $\left(\frac{\partial \mathbf{H}_\parallel}{\partial m^l}\right)_{l\in N}$ Fréchet derivatives tangential fields and $\left(\frac{\partial \mathbf{f}}{\partial m^l}\right)_{l\in N}$ Fréchet derivative of the forward operator $\mathbf{f}(\mathbf{m})$. This requires the derivatives to be defined over $\mathfrak{M}$. Should γ_0^E, γ_1^E, γ_0^H and γ_1^H be $\mathcal{C}^1$ complex functions on $\mathbb{R}^N$, we can write,

$$\delta \mathbf{E}_{\|} = \sum_{j=1}^{N} \left(\frac{\partial \gamma_0^E}{\partial m^j} \delta m_j . \hat{\mathbf{n}} \times \hat{\mathbf{q}}_i + \frac{\partial \gamma_1^E}{\partial m^j} \delta m^j . \hat{\mathbf{q}}_i \right) \tag{5.47}$$

$$\delta \mathbf{H}_{\|} = \sum_{j=1}^{N} \left(\frac{\partial \gamma_0^H}{\partial m^j} \delta m^j . \hat{\mathbf{n}} \times \hat{\mathbf{q}}_i + \frac{\partial \gamma_1^H}{\partial m^j} \delta m^j . \hat{\mathbf{q}}_i \right) \tag{5.48}$$

We provide the manifold with a metric tensor $g_{\alpha\beta} = g(\frac{\partial}{\partial m^\alpha}, \frac{\partial}{\partial m^\beta})$ following [Tarantola, 2005] approach to the problem. Although this calls for the use of differential geometry calculus, we shall simply define the metric as a symmetric isomorphism application from the local tangent spaces to $\mathfrak{M}$ to their duals. It allows to define the notion of distances over the manifold. In short, it defines the lengths of infinitesimal variations in all directions for all the points on $\mathfrak{M}$. Applied to our problem, the inverse of the metric tensor $g^{\alpha\beta}$ allows to build the so-called steepest descent vector s,

$$s^\alpha = -\sum_{\beta=1}^{N} g^{\alpha\beta} \frac{\partial S}{\partial m^\beta} \tag{5.49}$$

Where S is the misfit function to be minimized. A steepest descent algorithm is defined as an iterative algorithm where each increment at step n is carried along the steepest descent direction (e.g. [Tarantola, 2005]),

$$m_{n+1}^\alpha = m_n^\alpha - a_n . s_n = m_n^\alpha - a_n \sum_{\beta=1}^{N} g^{\alpha\beta} \left(\frac{\partial S}{\partial m^\beta} \right)_n \tag{5.50}$$

a_n are positive real valued coefficients which represent the length of the step to be carried out with regard to the metric used. If a_n is *too* small, the convergence is very slow while *very* large a_n will not allow the algorithm to converge. We further define the Hessian $\mathcal{H}$ as the second-order partial derivatives of the misfit function,

$$\mathcal{H}_{\alpha\beta} = \frac{\partial^2 S}{\partial m^\beta \partial m^\alpha} \tag{5.51}$$

The well established Newton method of optimization makes use of the Hessian to provide the manifold $\mathfrak{M}$ with a metric. Indeed, the Hessian can be readily used as a metric on $\mathfrak{M}$ and we write its inverse $\mathcal{W}$ which yields,

$$m_{n+1}^\alpha = m_n^\alpha - a_n \sum_{\beta=1}^{N} \mathcal{W}_n^{\alpha\beta} \left(\frac{\partial S}{\partial m^\beta} \right)_n \tag{5.52}$$

This metric provides an optimum solution as it is equivalent to tracking the quadratic minimum of the misfit function locally. Equation 5.52 can be expressed as,

$$\mathcal{H}_n \left(\mathbf{m}_{n+1} - \mathbf{m}_n \right) = -a_n \left(\frac{\partial S}{\partial \mathbf{m}} \right)_n \tag{5.53}$$

We now recognize the the so-called normal equation used with quasi-Newton methods for instance. Using equation 5.12 we easily obtain,

$$\left(\frac{\partial S}{\partial \mathbf{m}} \right)_n = \left(\frac{\partial \mathbf{f}}{\partial \mathbf{m}} \right)_n^t \mathbf{C}_D^{-1} \left(\mathbf{f}(\mathbf{m}_n) - \mathbf{d}_{obs} \right) + \mathbf{C}_M^{-1} \left(\mathbf{m}_n - \mathbf{m}_{prior} \right) \tag{5.54}$$

We use the covariance function $\mathbf{C}_M$ as a metric on $\mathfrak{M}$ along with the steepest descent algorithm which yields,

$$\mathbf{m}_{n+1} = \mathbf{m}_n - a_n . \left(\mathbf{C}_M \left(\frac{\partial \mathbf{f}}{\partial \mathbf{m}} \right)_n^t \mathbf{C}_D^{-1} \left(\mathbf{f}(\mathbf{m}_n) - \mathbf{d}_{obs} \right) + \left(\mathbf{m}_n - \mathbf{m}_{prior} \right) \right) \tag{5.55}$$

We shall not discuss any further gradient algorithms as it is a vast topic widely covered in the literature (e.g. [Oliver, 1998; Dorn et al., 1999; Virieux and Operto, 2009]). In the frame of this work, we shall use a simple steepest descent algorithm with equation 5.55. We now split the steepest descent algorithm into its basic computations,

$$\mathbf{d}_n = \mathbf{f}(\mathbf{m}_n) \tag{5.56}$$
$$\delta \mathbf{d}_n = \mathbf{d}_n - \mathbf{d}_{obs,n} \tag{5.57}$$
$$\delta \hat{\mathbf{d}}_n = \mathbf{C}_D^{-1} \delta \mathbf{d}_n \tag{5.58}$$
$$\delta \hat{\mathbf{m}}_n = \left(\frac{\partial \mathbf{f}}{\partial \mathbf{m}} \right)_n^t \delta \hat{\mathbf{d}}_n \tag{5.59}$$
$$\delta \mathbf{m}_n = \mathbf{C}_M \delta \hat{\mathbf{m}}_n \tag{5.60}$$
$$\mathbf{m}_{n+1} = \mathbf{m}_n - \nu_n \left(\delta \mathbf{m}_n + \left(\mathbf{m}_n - \mathbf{m}_{prior} \right) \right) \tag{5.61}$$

Each step thus requires the computation of the forward problem $\mathbf{d}_n = \mathbf{f}(\mathbf{m}_n)$ and the computation of the parameters residuals $\delta \hat{\mathbf{m}}_n = \left(\frac{\partial \mathbf{f}}{\partial \mathbf{m}} \right)_n^t \delta \hat{\mathbf{d}}_n$ which both amount for most of the computation time. Additionally the inverse of the covariance function can also be time consuming. We now turn to the characterization of the transpose operator of the Fréchet derivatives. To solve the inverse problem, we need to be able to compute $\left[\left(\frac{\partial \mathbf{f}}{\partial \mathbf{m}} \right)_n^t \delta \hat{\mathbf{d}} \right]$ for arbitrary $\delta \hat{\mathbf{d}}$. From equation 5.24 we obtain,

$$\langle \hat{\mathbf{d}}, \left(\frac{\partial \mathbf{f}}{\partial \mathbf{m}} \right) \mathbf{m} \rangle = \langle \left(\frac{\partial \mathbf{f}}{\partial \mathbf{m}} \right)_n^t \delta \hat{\mathbf{d}}, \mathbf{m} \rangle \tag{5.62}$$

$$\sum_{\beta \in I} \int_B \hat{\mathbf{d}}^t(\beta, \omega_0) . \left[\left(\frac{\partial \mathbf{f}}{\partial \mathbf{m}} \right) \mathbf{m} \right] (\beta, \omega_0) d\omega_0 = \langle \left(\frac{\partial \mathbf{f}}{\partial \mathbf{m}} \right)_n^t \delta \hat{\mathbf{d}}, \mathbf{m} \rangle \tag{5.63}$$

$$\begin{aligned} &\langle \left(\frac{\partial \mathbf{f}}{\partial \mathbf{m}} \right)_n^t \delta \hat{\mathbf{d}}, \mathbf{m} \rangle = \\ &\sum_{\beta \in I} \int_B \hat{\mathbf{d}}^t(\beta, \omega_0) . \sum_{\alpha \in I} \left[\int_B \bar{\bar{\mathbf{C}}}^{\alpha,\beta}(\omega, \omega_0) \cdot \left[\int_{\partial \Omega'} \bar{\bar{\mathbf{K}}}_e^{\alpha}(\mathbf{x}', \omega, \omega_0) \cdot \right. \right. \\ &\left. \left. \left[\int_{\partial \Omega} \left[-i\omega \tilde{\mu}_i \bar{\bar{\mathbf{G}}} \cdot \frac{\partial \mathbf{H}_{\|}}{\partial \mathbf{m}} + \nabla \times \bar{\bar{\mathbf{G}}} \cdot \frac{\partial \mathbf{E}_{\|}}{\partial \mathbf{m}} \right] (\alpha, \mathbf{x}', \mathbf{x}, \omega) \cdot \mathbf{m}(\mathbf{x}, \omega) d\sigma(\mathbf{x}) \right] d\sigma(\mathbf{x}') \right] d\omega \right] d\omega_0 \end{aligned} \tag{5.64}$$

$$\int_B d\omega' \int_{\partial\Omega} d\sigma(\mathbf{x}') \left[\left(\frac{\partial \mathbf{f}}{\partial \mathbf{m}} \right)_n^t \delta\hat{\mathbf{d}} \right]^* (\mathbf{x}', \omega').\mathbf{m}(\mathbf{x}', \omega') =$$
$$\sum_{\beta\in I} \int_B \hat{\mathbf{d}}^t(\beta, \omega_0).\sum_{\alpha\in I} \left[\int_B \bar{\bar{\mathbf{C}}}^{\alpha,\beta}(\omega, \omega_0) \cdot \left[\int_{\partial\Omega'} \bar{\bar{\mathbf{K}}}_e^{\alpha}(\mathbf{x}', \omega, \omega_0) \cdot \right.\right.$$
$$\left.\left[\int_{\partial\Omega} \left[-i\omega\tilde{\mu}_i \bar{\bar{\mathbf{G}}} \cdot \frac{\partial \mathbf{H}_\parallel}{\partial \mathbf{m}} + \nabla \times \bar{\bar{\mathbf{G}}} \cdot \frac{\partial \mathbf{E}_\parallel}{\partial \mathbf{m}} \right] (\alpha, \mathbf{x}', \mathbf{x}, \omega) \cdot \mathbf{m}(\mathbf{x}, \omega) d\sigma(\mathbf{x}) \right] d\sigma(\mathbf{x}') \right] d\omega \right] d\omega_0 \tag{5.65}$$

As the previous equation has to be right for any $\mathbf{m}(x, \omega)$, we obtain,

$$\left[\left(\frac{\partial \mathbf{f}}{\partial \mathbf{m}} \right)_n^t \delta\hat{\mathbf{d}} \right]^* (\mathbf{x}, \omega) =$$
$$\sum_{\beta\in I} \int_B \hat{\mathbf{d}}^t(\beta, \omega_0).\sum_{\alpha\in I} \bar{\bar{\mathbf{C}}}^{\alpha,\beta}(\omega, \omega_0) \cdot \left[\int_{\partial\Omega'} \bar{\bar{\mathbf{K}}}_e^{\alpha}(\mathbf{x}', \omega, \omega_0) \cdot \right. \tag{5.66}$$
$$\left. \left[-i\omega\tilde{\mu}_i \bar{\bar{\mathbf{G}}} \cdot \frac{\partial \mathbf{H}_\parallel}{\partial \mathbf{m}} + \nabla \times \bar{\bar{\mathbf{G}}} \cdot \frac{\partial \mathbf{E}_\parallel}{\partial \mathbf{m}} \right] (\alpha, \mathbf{x}', \mathbf{x}, \omega) d\sigma(\mathbf{x}') \right] d\omega_0$$

In most cases we have chosen Gaussian or exponential correlation functions to describe uncertainties for the sake of simplicity. The choice of coefficients a_n was not thoroughly studied. Indeed, our work focused on the benefit of the approach and we were mostly interested in the thriving perspectives of data inversion in a rigorous frame.

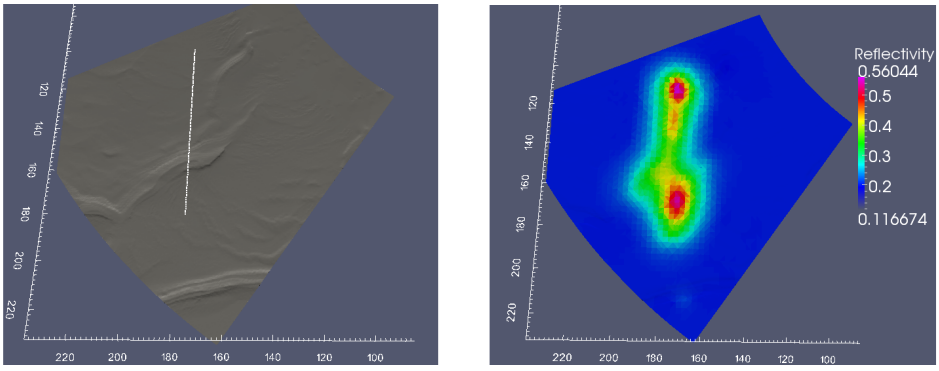

(a) Orbit track (b) Posterior mean

Figure 19: Non-linear inversion. The setup used is identical to the one described in figure 13.

Results

Similarly to the previous section, we have conducted several inversions with identical setups. In other words, we have used the non-linear technique to solve the linear problem presented in the previous section. All the results displayed were obtained with a single step. In order to achieve this, we have roughly fitted

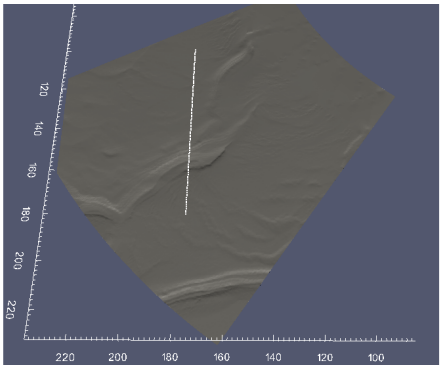

(a) Orbit track

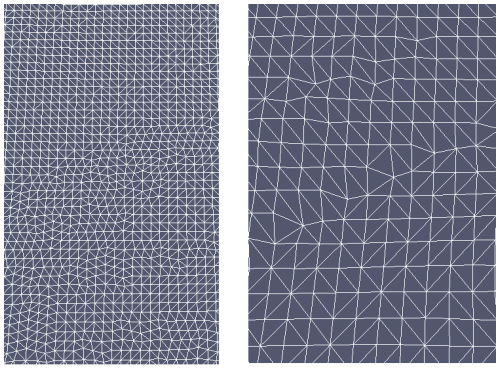

(b) Mesh resolution comparison

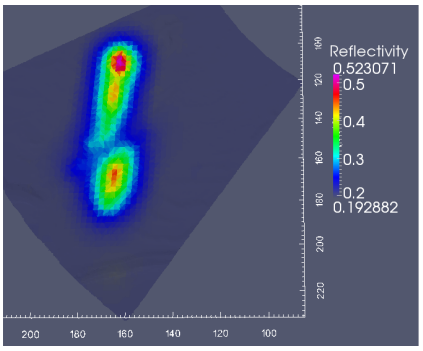

(c) Posterior mean obtained with low resolution surface model

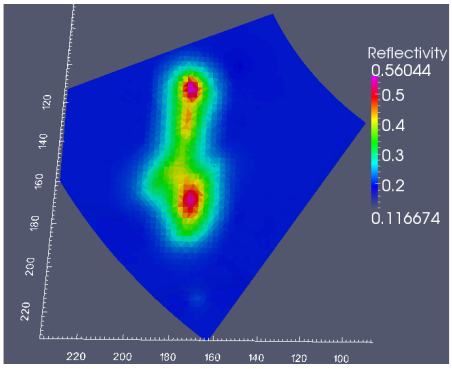

(d) Posterior mean obtained with high resolution surface model

Figure 20: Non-linear inversion. The setup used is identical to the one described in figure 14.

the coefficient a_n in equation 5.55 (in our case a_0) as to obtain a posterior mean close to the expected result. Practically, obtained results are very close to those obtain with the linear approach. The sensitivity to the noise and to the surface remains unchanged with that of the linear technique. These results are to be expected since the non-linear technique – with a quasi-Newton method – yields identical analytical results when the problem is linear. In our case, we have used a simplified algorithm, making use of the covariance operator $\mathbf{C}_M$ as the metric over the model manifold, hence the results are not exactly identical.

5.3 A STATISTICAL PERSPECTIVE

We propose here to develop a Monte-Carlo approach to the inverse problem described previously. Monte-Carlo methods are in essence suitable for a large category of problems where high non-linearity and an important number of local minima may arise. This method is poorly adapted to large scaled problems as a stand-alone but may be necessary to identify global maxima in the posterior probability density which is the reason why we have decided to study it.

Theory and implementation

We provide the parameter manifold $\mathfrak{M}$ with a probability density $\rho_M(\mathbf{m})$ describing the a priori information on the model parameters and the data manifold $\mathfrak{D}$ with a probability density $\rho_D(\mathbf{d})$ describing the a priori information on the data parameters. The combination of the information on these two mani-

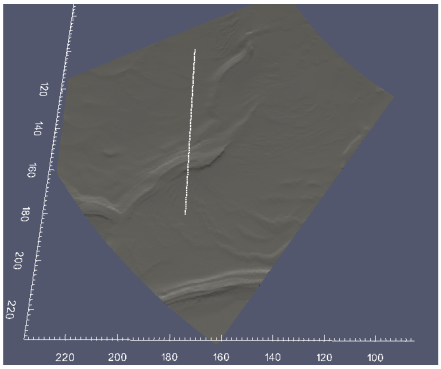

(a) Orbit track

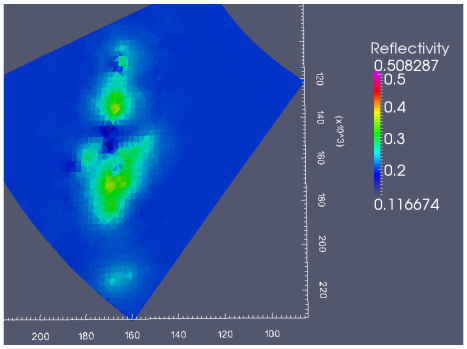

(b) Posterior mean

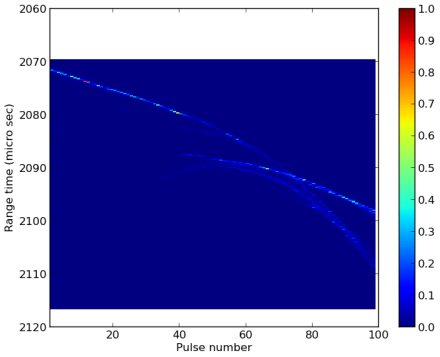

(c) Radar echo (no noise)

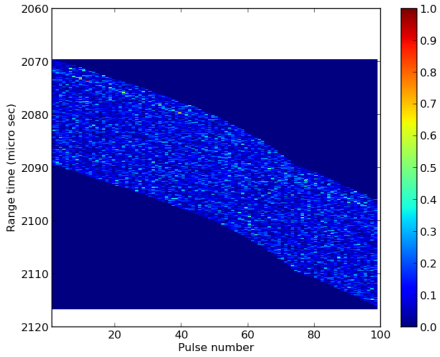

(d) Radar echo (with noise)

Figure 21: Non-linear inversion. The setup used is identical to the one described in figure 16.

folds yields posterior probability density $\sigma_M(\mathbf{m})$ on $\mathfrak{M}$. In our case, the forward problem provides a functional relation between data elements $\mathbf{d}$ on the data manifold and model elements $\mathbf{m}$ on the parameter manifold which we write as $\mathbf{d} = \mathbf{f}(\mathbf{m})$ (see previous sections). The posterior probability density simplifies to,

$$\sigma_M(\mathbf{m}) = a_M.\rho_M(\mathbf{m}).\rho_D(\mathbf{f}(\mathbf{m})) \tag{5.67}$$

We suppose we are able to generate samples of the prior probability density $\rho_M(\mathbf{m})$. Practically, for the examples presented, we have used a direct method based on the Cholesky decomposition of the covariance matrix to generate discrete Gaussian random fields. However this method is poorly adapted to large scale problems as the memory storage of the full covariance matrix increases dramatically with the number of variables. Implementation of algorithms able to generate large random fields will be required in the future if one wants to use Monte-Carlo methods (e.g. [Lang and Potthoff, 2011]). We propose to use the Metropolis-Hastings algorithm (e.g. [Hastings, 1970; Metropolis et al., 1953]) to sample the posterior probability density. The algorithm relies on a random walk – a Markov chain to be precise as each step depends solely on the previous step – which samples the posterior probability density. The walk can be described as followed, suppose we are at a given step i (i.e. at $\mathbf{m}_i$), if $\rho_D(\mathbf{f}(\mathbf{m}_j)) \geq \rho_D(\mathbf{f}(\mathbf{m}_i))$, then we accept the proposed transition to $\mathbf{m}_j$. If $\rho_D(\mathbf{f}(\mathbf{m}_j)) \leq \rho_D(\mathbf{f}(\mathbf{m}_i))$, then we decide randomly to move to $\mathbf{m}_j$, or to stay at $\mathbf{m}_i$, with the following probabil-

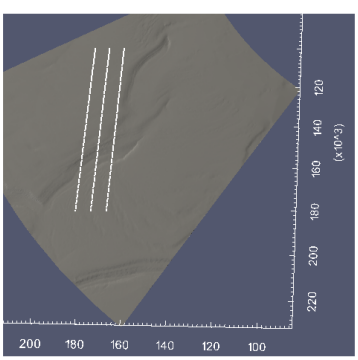

(a) Orbit track

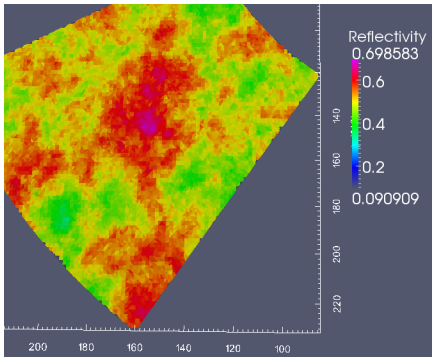

(b) Real data

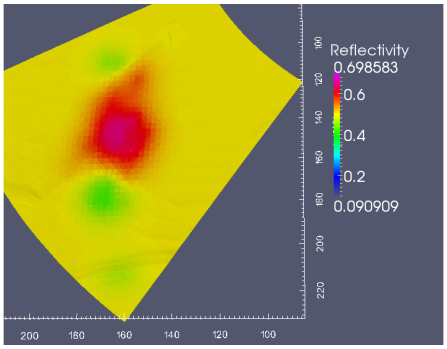

(c) Posterior mean

Figure 22: Non-linear inversion. The setup used is identical to the one described in figure 17.

ity $P_{i,j}$ of accepting the move to $\mathbf{m}_j$: $P_{i,j} = \dfrac{\rho_D(\mathbf{f}(\mathbf{m}_j))}{\rho_D(\mathbf{f}(\mathbf{m}_i))}$. Monte-Carlo algorithms require to be able to compute the forward model fast enough to obtain a representative set of posterior probability density samples.

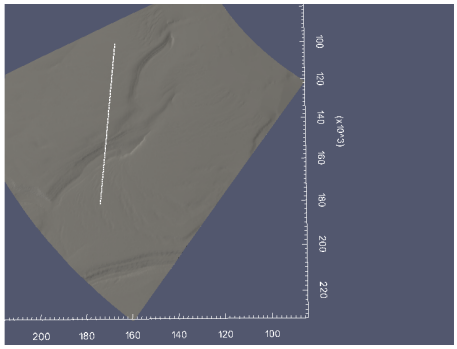

(a) Orbit track

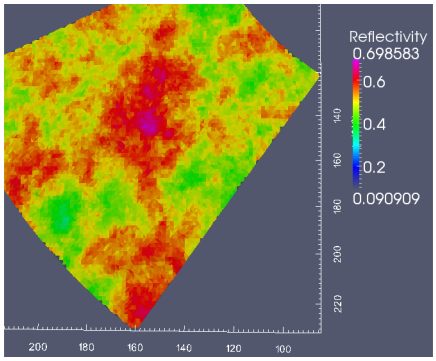

(b) Real data

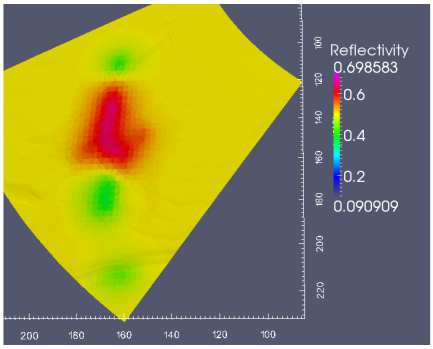

(c) Posterior mean

Figure 23: Non-linear inversion. The setup used is identical to the one described in figure 18.

Data: Radar measurements in frequency domain (spectra) and prior model (surface topography $\partial\Omega$ with reflection parameters on $\partial\Omega$ for each frequency N_f). $NumberOfRuns$ define the number of models to be tested.
Result: Inversion of surface parameters
Load prior model and generate parameter grid $\mathbf{m}_{prior}$;
Load observation data $\mathbf{d}_{obs}$;
Compute covariance matrix $\mathbf{C}_M$;
Compute direct operator $\mathbf{F} = \{F^i\}_{i \in N_f}$;
Generate random reflectivity field $\mathbf{m}_i$;
Compute data $\mathbf{d} = \mathbf{F}\mathbf{m}_{rand}$;
Compute data probability density $\rho_i = \rho_D(\mathbf{d})$;
for $i = 1$ **to** $NumberOfRuns$ **do**
    Generate random reflectivity field $\mathbf{m}_{rand}$;
    Compute data $\mathbf{d} = \mathbf{F}\mathbf{m}_{rand}$;
    Compute data probability density $\rho_{rand} = \rho_D(\mathbf{d})$;
    if $\rho_i > \rho_{rand}$ **then**
        (Update);
        $\rho_i = \rho_{rand}$;
        $m_i = m_k$;
    end
    else
        Generate random number r in [0,1];
        if $r < (\rho_i \, \rho_{rand}$ **then**
            (Update);
            $\rho_i = \rho_{rand}$;
            $m_i = m_k$;
        end
    end
end

Algorithm 3: Algorithm of the Monte-Carlo approach. The set of m_i samples the posterior probability density (i.e. random walk following the posterior probability density).

Note: For our simulations, we use the Mesrenne Twister algorithm to generate uniform pseudorandom numbers (e.g. [Matsumoto and Nishimura, 1998]).

Results

We have conducted two examples to illustrate the Monte Carlo algorithm. Figure 24 displays results obtained with synthetic radar data (noise free). A single frequency at 15 MHz for each radar measurements on the orbit track (100 acquisition points) was used to perform the inversion. The targeted surface was set to have a constant reflectivity of 0.5. The prior model surface topography was the same as the targeted surface (i.e. identical meshing) and the prior reflectivity was set to be constant of the surface at 0.2. The prior standard deviation was set to 0.3 with a 5km correlation length. A set of 2500 random reflectivity maps were used to conduct the inversion. The result shows a convergence towards the true reflectivity value. The posterior standard deviation allows to assess the uncertainties on the posterior mean. The posterior mean converges slowly towards the posterior mean obtained with the linear algorithm. The number of sets used here is not sufficient to conduct a proper inversion but a clear trend is observed. On the other hand, figure 25 displays results obtained from an inversion using a single frequency at 15 MHz for each radar measurements on the orbit tracks (100 acquisition points equally spaced along each orbit track).

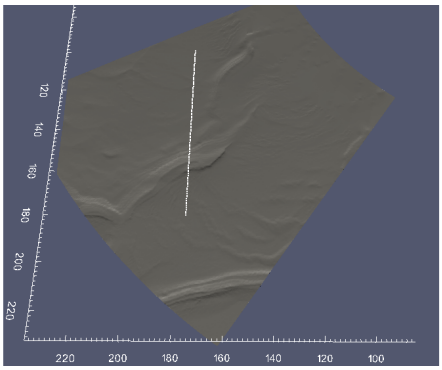

(a) Orbit track

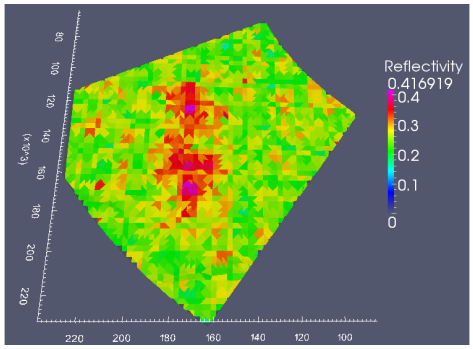

(b) Posterior mean

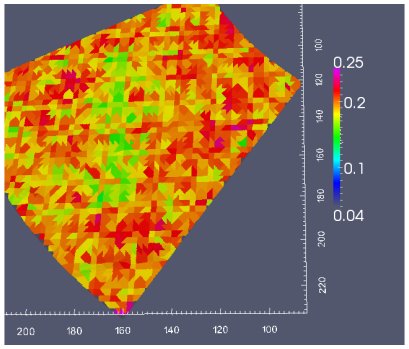

(c) Posterior standard deviation

Figure 24: Monte Carlo inversion. The setup used is identical to the one described in figure 18.

The targeted surface was set to have non-constant reflectivity and was identical. The prior model surface topography was the same as the targeted surface (i.e. identical meshing) and the prior reflectivity was set to be constant of the surface at 0.5. The prior standard deviation was set to 0.2 with a 5km correlation length. A set of 2500 random reflectivity maps were used to conduct the inversion. The posterior mean displays a trend towards the true reflectivity value but the result is not well adapted to recover the true reflectivity values. Overall, the Monte Carlo algorithm presented provides a good approach for a first guess but is not well suited to perform the inversion as a stand-alone.

As an illustration to the techniques presented in this chapter, figure 26 offers a comparison of the *best model* obtained with each technique. The target was a surface with constant reflectivity coefficients. Synthetic radar measurements with no noise were produced along the orbit track (see figure 26). The inversion was conducted using a single frequency for the sake of illustration. The prior reflectivity was set to 0.2 and was set constant over the surface, the prior standard deviation was set to 0.3 with a correlation length of 5km. The results converge towards a constant reflectivity coefficient. The linear inversion displays the best result of course as it is perfectly suited in this case. The non-linear inversion (first-step) result shows a rapid convergence towards the result very much like the Monte Carlo inversion result. Other techniques exist to tackle inverse problem.However, this work should provide a good insight on what can be done to recover surface reflectivity parameters.

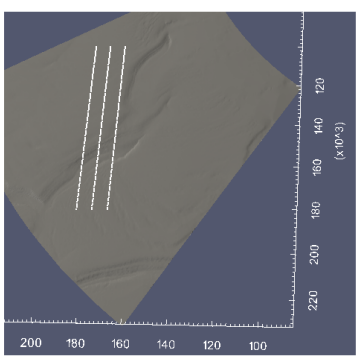

(a) Orbit track

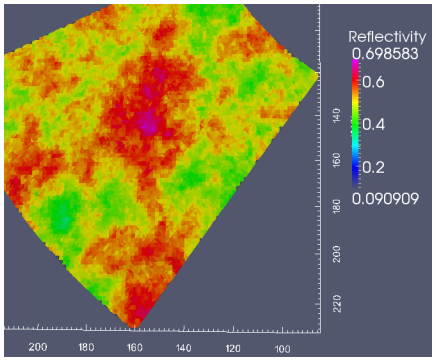

(b) Real data

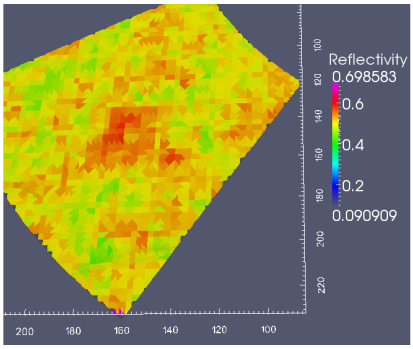

(c) Posterior mean

Figure 25: Monte Carlo inversion. The setup used is identical to the one described in figure 17.

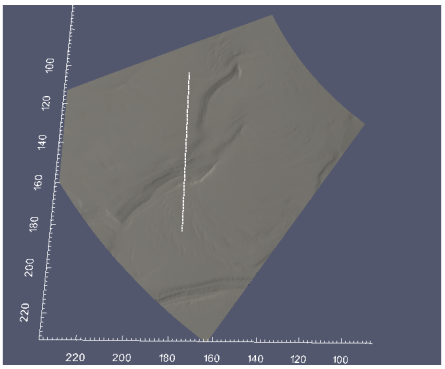

(a) Orbit track

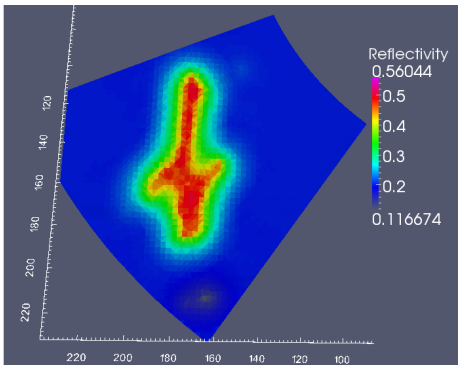

(b) Linear inversion

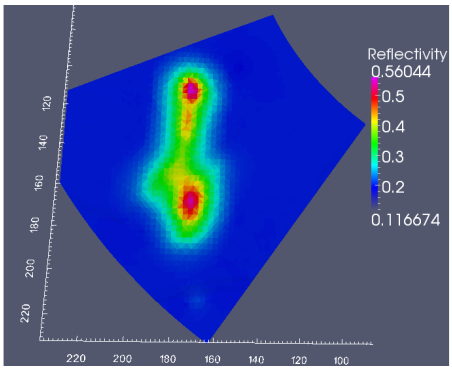

(c) Non linear (first step) inversion

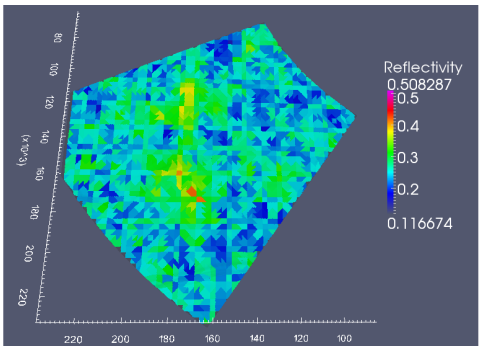

(d) Monte Carlo inversion

Figure 26: Inversion of constant surface reflectivity coefficients set to 0.5 with a single frequency from an orbit portion (100 acquisition points) with different approaches. The prior reflectivity was set to 0.2 (constant over the surface), the prior variance set to 0.3 and the correlation length was set to 5km. The scales are in kilometers.

6 DISCUSSING THE OTHER PARAMETERS

This section discusses the possibility to extend the previous work to additional parameters, namely the material parameter in Ω (the atmospheric environment in planetary sounding radar) and the topography.

6.1 SOUNDING THE UPPER MEDIUM

Electromagnetic fields are distorted when travelling through the ionosphere resulting in a change in the electromagnetic field phase $\Delta\phi$ for each pulsation ω. This frequency dependent phase distortion causes a defocusing of the radar signal, a rotation of the signal phase as well as a time delay with regard to a reference void upper medium. The phase distortion can be expressed as (see [Mouginot et al., 2008]),

$$\Delta\phi(\omega) = \frac{2\omega}{c}\int_{\mathcal{R}}\left(1-\sqrt{\epsilon(\mathbf{x})}\right)dr(\mathbf{x}) \tag{6.1}$$

$$\sqrt{\epsilon(\mathbf{x})} = \sqrt{1-\frac{\omega_p^2(\mathbf{x})}{\omega^2}} \approx 1-\frac{1}{2}\frac{\omega_p^2(\mathbf{x})}{\omega^2}-\frac{1}{8}\left(\frac{\omega_p^2(\mathbf{x})}{\omega^2}\right)^2-\frac{1}{16}\left(\frac{\omega_p^2(\mathbf{x})}{\omega^2}\right)^3 \tag{6.2}$$

$$\omega_p(\mathbf{x}) = 2\pi 8.98\sqrt{N_e(\mathbf{x})} \tag{6.3}$$

Where $\mathcal{R}$ denotes the ray path, c is the speed of light in free space, $\omega_p(\mathbf{x})$ is the local plasma frequency and $N_e(\mathbf{x})$ is the electron density profile of the ionosphere along $\mathcal{R}$. Several studies have been conducted to recover the upper medium material parameters from sounding radar measurements (e.g. [Mouginot et al., 2008; Safaeinili et al., 2007]). In the surface equivalent formulation, upper material properties affect the Green function (by definition) as well as surface electromagnetic fields through the incident fields. If one assumes an anisotropic inhomogeneous medium, recovering material properties turns out to be a complex problem. As material variations in the atmosphere tend to be smooth with slow spatial variations, we can assume local constant parameters (i.e. constant for each acquisition point). In [Mouginot et al., 2008], provided this approximation, a set of parameters $\{p_1, p_2, p_3\}$ is defined, with $p_i = \int_{\mathcal{R}} N_e^i(\mathbf{x})dr(\mathbf{x})$. This parametrization allows to carry out a fast inversion through an extensive parameter space search (only three dimensions per acquisition). The objective is to maximize the amplitude of the signal, although other cost functions can be used at this point. We can reinterpret the algorithm presented in [Mouginot et al., 2008] through a Monte-Carlo approach (see section 5.3) where we can provide prior probability distributions to the parameters $\{p_1, p_2, p_3\}$ and a covariance function describing the data uncertainties. Data can be chosen to be either the full waveform signal or the amplitude of baseband Fourier transformed signals. At this point, it is easy to imagine to perform a joint inversion of reflectivity parameters with upper medium parameters using a Monte-Carlo approach where reflectivity parameters are not frequency dependant to reduce the parameter space size.

6.2 RECONSTRUCTION OF SURFACE OBSTACLE USING FAR FIELD RADAR MEASUREMENTS

I believe it is possible to use sounding radar experiments to help in planetary surface topography reconstruction. The lack of data due to acquisition geometries in planetary sounding radar does not allow the radar to work as a standalone instrument in most cases. However radar data contain valuable information on the surface topography which can be used in topography reconstruction. We shall discuss here different strategies to recover this parameter. We assume the boundary surface $\partial\Omega$ to conform partially with the planetary surface $\partial\Omega_0$ in the following sections such that $\partial\Omega_0 = \partial\Omega + \delta S$. δS is a perturbation to the true surface $\partial\Omega_0$.

Using phase information in reflectivity coefficients

Using the linear approach described in section 5.1, we interpret the module of the reflection parameter as Fresnel coefficient at normal incidence R_f and the phase term as a phase shift due to δS,

$$R(\mathbf{x}) = R_f(\mathbf{x}).e^{2ik\delta S(\mathbf{x})} \tag{6.4}$$

This interpretation is valid as long as δS is sufficiently smooth with large spatial correlation length. Typically, this technique works well for constant offset $\delta S(\mathbf{x})$ (see figure 27). Recovering $\delta S(\mathbf{x})$ from $R(\mathbf{x})$ is straightforward through Fourier transform of $e^{2ik\delta S(\mathbf{x})}$ and identification of the *maximum*. Recovering δS requires sufficient measurements over a frequency band. As we deal with discrete data, this implies that $2\delta S/c$ is within the listening time of each record and that the number of frequencies within the band is sufficient to properly assess δS. Figure 27 illustrates this technique as it shows a joint inversion of a surface constant offset and of the surface reflectivity. The prior surface was shifted from the original surface used to generate observed data. This induces non-null phase terms in the estimated reflectivity parameters. Interpreting phase terms as topography offset in the inversion process, we can reconstruct the original surface. The original reflectivity parameter was set constant, 0.5 over the surface while the prior reflectivity parameters were set to 0.1 with 5km correlation length.

Towards shape reconstruction

An important amount of work has been dedicated to the reconstruction of surface obstacle using far field electromagnetic measurements (e.g. [Bourgeois et al., 2011a,b; Rigling et al., 2005]). In short, the technique presented in the previous section only handles constant δS and is not satisfactory for topography reconstruction in general. We propose a rapid study of a non-linear approach to topography reconstruction from sounding radar measurements. We suppose we are able to parametrize $\partial\Omega$. For instance, we provide a Cartesian frame such that $\partial\Omega(\mathbf{x}) = \{z(x, y)\}$ where x, y and z are coordinates of $\mathbf{x}$ in the Cartesian frame. A similar parametrization can be performed using spherical coordinates. From a mathematical point of view, shape reconstruction in non-linear optimization schemes involves second-order surface differential operator (e.g. [Bourgeois et al., 2011b]). This problem naturally arises when computing Fréchet derivatives of the operator with regard to $\partial\Omega(\mathbf{x})$. An interesting way to proceed would be to use a *facet* description of the surface – very much like in section 4 – where parameters would be the locations of the vertices of all the facets. The second order derivatives thus implicitly vanish with flat facets. This can be thought as imposing prior knowledge on the second order derivatives. Derivatives with

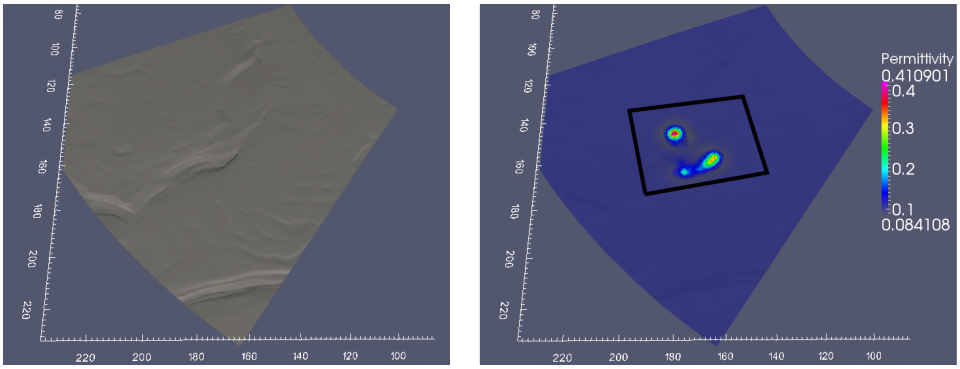

(a) Original surface topography

(b) Inversion result

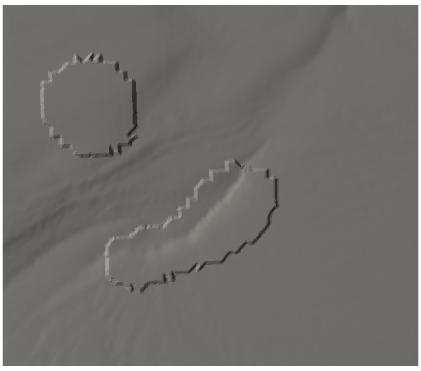

(c) Topography shift

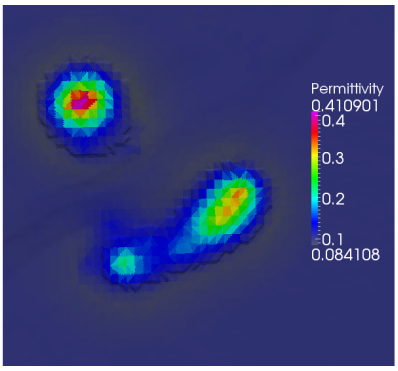

(d) Reflectivity amplitudes

Figure 27: Inversion of complex reflectivity parameters. The prior surface was shifted from the original surface used to generate data space which induces non-null phase terms in the reflectivity parameters. Interpreting phase terms as topography offset in the inversion process, we can reconstruct the original surface. The original reflectivity parameter was constant, 0.5 over the surface while the prior reflectivity parameters were set to 0.1.

regard to the vertices can be readily obtained with equations in section 4. The implementation remains to be done but offers interesting perspective for sounding radar instruments.

One could also imagine Monte-Carlo strategies (see section 5.3) using the forward modelling tool presented in section 4 to tackle the problem. This work remains to be done.

Part IV

DISCUSSIONS

7 CONCLUSION AND PERSPECTIVES

Voodoo Lady: I am one gifted with the Second Sight,
adept at manipulating the forces of nature for the benefit of all who enter my door.
Guybrush Threepwood: You're a fashion consultant?
Voodoo Lady: Well... yes, but that's not what I was referring to. I am a Voodoo Priestess.
Guybrush Threepwood: Neat.
Voodoo Lady: You're an "autumn," by the way.

— The Curse Of Monkey Island

7.1 A QUICK OVERVIEW OF THE MANUSCRIPT

This thesis has been conducted in the frame of the JUICE mission and more specifically was dedicated to the design of the radar sounding instrument RIME. Although the manuscript only mention this context in the introduction, the work was definitively motivated by the hostile environment reported in [Berquin et al., 2012]. The goal of the study was to help in the development of radar sounding instruments through quantitative data analysis. In order to perform this we have developed a code based on Huygens-Fresnel's principle to compute planetary radar surface echoes. We have also shown how the algorithm used could be extend to broader sets of problem where electromagnetic surface fields are known and how it relates to previously developed algorithms. Finally, we have formulated and implemented equations to recover geophysical surface parameters with a probabilistic inverse scheme. The inverse problem formulation took advantage of the colossal amount of work performed in seismic prospecting fields. Results indicate promising perspective for radar data analysis. Since formulations directly link to the physics, they allow joint inversion of different radar sounding experiments and stress the importance of acquisition geometries in planetary sounding radar. As a result, algorithms presented take advantage of the full recorded signal – including the so-called clutter – to properly infer reflectivity parameters. Additional studies were carried out to recover other geophysical parameters such as the surface topography and the total electron content in the ionosphere. To much my supervisor's dismay, I did not have enough time to conduct dielectric inversion on an extensive real data set. However, we can still hope that this work will be carried out in the near future. High resolution terrain elevation models from High Resolution Imaging Science Experiment (HiRISE) and High Resolution Stereo Camera (HRSC) offer exciting prospects for SHARAD data inversion. Proper characterization of instrument uncertainties should also be investigated.

7.2 A FOREWORD ON SUBSURFACE IMAGING

On a darker note, I believe the work presented in this manuscript suffers from the surface formulation which does not allow the study of complex subsurface media. This shortcoming calls for the development of efficient forward modelling tools in planetary sounding radar. Only with such tools can we hope to quantitatively recover subsurface geophysical parameters. The sounding radar experiment onboard *Rosetta* is a great opportunity for the development of such tools (e.g. [Kofman et al., 2007]). A powerful ray tracing code is currently under development for this specific purpose and should offer additional perspectives for all planetary sounding radar experiments. Had we disposed of such a tool,

I believe it would have offered even more thriving opportunities for sounding radar experiments. Surface formulation remains to me however a milestone on the quest to geophysical exploration.

7.3 BEYOND THE MANUSCRIPT

Beyond the scope of this manuscript, it seems there is room for an increased synergy between instruments in future space missions. As briefly explained in section 6, sounding radar data can be used in surface topography reconstruction along with other instruments such as cameras (e.g. JANUS) and laser altimeters (e.g. GALA). More generally, I strongly believe joint inversions should be more common than they are nowadays and theoretical studies would greatly benefit to planetary space exploration (e.g. [Colombo and De Stefano, 2007; Zhdanov et al., 2012]). The JUICE mission could be an interesting opportunity to carry out such studies. It also seems to me that planetary sounding radar should take advantage of the vast amount of work performed on electromagnetic remote sensing in applied mathematics (e.g. [Bourgeois et al., 2011b]) and geophysics (e.g. [Zhdanov et al., 2012]). Important efforts have been made to provide a differential geometry frame of work in computational electromagnetism (e.g. [Warnick, 1997; Desbrun et al., 2005]) which offers exciting perspectives as discussed in appendix C.

Part V

APPENDIX

A

MAXWELL'S EQUATIONS AND THE CONSTITUTIVE RELATIONS

Dana Barrett: You know, you don't act like a scientist.
Dr. Peter Venkman: They're usually pretty stiff.
Dana Barrett: You're more like a game show host.

— Ghostbusters

Sounding radar techniques rely on the interaction of electromagnetic waves with planetary environments and bodies. The physics of these interactions is well-established, very detailed and widely discussed in the literature (e.g. [Kong, 2000; Colin de Verdière, 1996-1997; Lindell, 2005; Warnick et al., 1997]). We shall recall here main equations governing electromagnetic fields in media for the sake of completeness of this manuscript. Considering the problem at hand only *macroscopic phenomena* will be studied (no quantization of electromagnetic waves considered).

For a "modern" formulation of Maxwell's equations and the constitutive relations please refer to appendix C.

I used vectorial formulations which is the most common way to introduce the problem today (although as discussed in appendix C it may not be the most adapted). This section was mostly inspired by [Kong, 2000; Le Gall, 2007]). Electromagnetic wave propagation is governed through *Maxwell's equations*,

$$\nabla \times \mathcal{H} - \frac{\partial}{\partial t}\mathcal{D} = \mathcal{J} \tag{A.1}$$

$$\nabla \times \mathcal{E} + \frac{\partial}{\partial t}\mathcal{B} = 0 \tag{A.2}$$

$$\nabla \cdot \mathcal{J} + \frac{\partial}{\partial t}\rho = 0 \tag{A.3}$$

where $\mathcal{E}, \mathcal{B}, \mathcal{H}, \mathcal{D}, \mathcal{J}$ and ρ denotes functions in $\mathbb{R}^3$ at a space position $x \in \mathbb{R}^3$ and at a time $t \in \mathbb{R}$.

- $\mathcal{E}(x,t) =$ electric field strength (volts/m)
- $\mathcal{H}(x,t) =$ magnetic field strength (amperes/m)
- $\mathcal{B}(x,t) =$ magnetic flux density (webers/m)
- $\mathcal{D}(x,t) =$ electric displacement (coulombs/m^2)
- $\mathcal{J}(x,t) =$ electric current density (amperes/m^2)
- $\rho(x,t) =$ electric charge density (coulombs/m^3)

With the previous equations regarded as fundamental equations, and assuming magnetic monopoles not to exist – as they have not been found to this day – we can additionally write,

$$\nabla \cdot \mathcal{D} = \rho \tag{A.4}$$

$$\nabla \cdot \mathcal{B} = 0 \tag{A.5}$$

Interestingly, the previous sets of equations do not make any reference to material properties. Hence, we need to relate the electromagnetic waves to the

medium with which they are interacting. This is achieved through the *constitutive relations*. The absence of such equations yields a non-constraint problem from a mathematical point of view. In the most general case – when dealing with macroscopic phenomena – constitutive relations can be written as,

$$c\mathcal{D} = \bar{\bar{\mathcal{P}}} \cdot \mathcal{E} + \bar{\bar{\mathcal{L}}} \cdot c\mathcal{B} \tag{A.6}$$

$$\mathcal{H} = \bar{\bar{\mathcal{M}}} \cdot \mathcal{E} + \bar{\bar{\mathcal{Q}}} \cdot c\mathcal{B} \tag{A.7}$$

where $c = 3 \times 10^8$ m/s is the velocity of light in vacuum and $\bar{\bar{\mathcal{P}}}$, $\bar{\bar{\mathcal{L}}}$, $\bar{\bar{\mathcal{M}}}$ and $\bar{\bar{\mathcal{Q}}}$ are all 3×3 dyadic operators. Their elements are called constitutive parameters. Constitutive operators elements may be functions of space and time coordinates, thermodynamical and continuum mechanical variables, or electromagnetic field strengths. The medium can be classified as (i) inhomogeneous if they are functions of space coordinates, (ii) nonstationary if they are function of time, (iii) time-dispersive if they contain time derivatives, (iv) nonlinear if they depend on the electromagnetic field, etc. Operators $\bar{\bar{\mathcal{L}}}$ and $\bar{\bar{\mathcal{M}}}$ allow a coupling between electric and magnetic fields. Should these operators be null, the medium is anisotropic. Furthermore, should $\bar{\bar{\mathcal{P}}} = c\epsilon\bar{\bar{\mathcal{I}}}$ and $\bar{\bar{\mathcal{Q}}} = 1/(c\mu)\bar{\bar{\mathcal{I}}}$, with $\bar{\bar{\mathcal{I}}}$ denoting the unit dyadic operator, the medium is isotropic. ϵ is called the electrical permittivity and μ the magnetic permeability, they are determined by the electrical properties of the medium and magnetic properties of the medium respectively. $\bar{\bar{\epsilon}}$ and $\bar{\bar{\mu}}$ are constitutive operators in the most general case. In free space (void of any matter), we define $\bar{\bar{\epsilon}} = \epsilon_0 \cdot \bar{\bar{\mathcal{I}}}$ and $\bar{\bar{\mu}} = \mu_0 \cdot \bar{\bar{\mathcal{I}}}$ with,

$$\epsilon_0 \approx 8.85 \times 10^{-12} \quad \text{farad/meter} \tag{A.8}$$

$$\mu_0 = 4.\pi \times 10^{-7} \quad \text{henry/meter} \tag{A.9}$$

Interestingly, we can rewrite constitutive relations in a different form to explicitly make use of the electrical permittivity and the magnetic permeability,

$$\mathcal{D} = \bar{\bar{\epsilon}} \cdot \mathcal{E} + \bar{\bar{\xi}} \cdot \mathcal{H} \tag{A.10}$$

$$\mathcal{B} = \bar{\bar{\zeta}} \cdot \mathcal{E} + \bar{\bar{\mu}} \cdot \mathcal{H} \tag{A.11}$$

with,

$$c\bar{\bar{\epsilon}} = \bar{\bar{\mathcal{P}}} - \bar{\bar{\mathcal{L}}} \cdot \bar{\bar{\mathcal{Q}}}^{-1} \cdot \bar{\bar{\mathcal{M}}} \tag{A.12}$$

$$c\bar{\bar{\xi}} = \bar{\bar{\mathcal{L}}} \cdot \bar{\bar{\mathcal{Q}}}^{-1} \tag{A.13}$$

$$c\bar{\bar{\zeta}} = -\bar{\bar{\mathcal{Q}}}^{-1} \cdot \bar{\bar{\mathcal{M}}} \tag{A.14}$$

$$c\bar{\bar{\mu}} = \bar{\bar{\mathcal{Q}}}^{-1} \tag{A.15}$$

For a particular frequency in the steady state, electromagnetic fields are time-harmonic and are known as monochromatic waves or continuous waves. A field varying arbitrarily in time may be – using Fourier analysis – represented as a sum of harmonic fields. For example, the electric field with angular frequency ω is written as,

$$\mathcal{E}(\mathbf{x}, t) = \mathbf{E}(x)e^{-i\omega t} \tag{A.16}$$

The previous expression can be generalized to the other functions. Thus, in the time-harmonic regime, Maxwell's equations become,

$$\nabla \times \mathbf{H} + i\omega\mathbf{D} = \mathbf{J} \tag{A.17}$$
$$\nabla \times \mathbf{E} - i\omega\mathbf{B} = 0 \tag{A.18}$$
$$\nabla \cdot \mathbf{J} - i\omega\rho = 0 \tag{A.19}$$
$$\nabla \cdot \mathbf{D} = \rho \tag{A.20}$$
$$\nabla \cdot \mathbf{B} = 0 \tag{A.21}$$

Under the time-harmonic representation, constitutive elements are, in general, complex. We shall briefly discuss here the physics underlying constitutive elements in the sounding radar frame.

The electric permittivity

From a microscopic point of view, the permittivity characterizes the local redistribution of charges due to the electromagnetic field. In other word, it describes the polarisation of the material. Under an electromagnetic field, local charges change from their equilibrium point through a separation of the charges, to compensate field effects. The polarization phenomenon derives from different physical processes depending on the angular frequency (see figure 1), with different relaxation times. The real part of the permittivity ϵ' controls the celerity of the wave in the medium whereas the imaginary part ϵ'' accounts for material absorption – in addition to conductive losses – as charges local movements dissipate energy. The permittivity is thus written as $\bar{\bar{\epsilon}} = \bar{\bar{\epsilon}}' - i\bar{\bar{\epsilon}}''$.

The electric conductivity

The electric conductivity $\bar{\bar{\sigma}}$ characterizes the displacement capacity of free charges within the medium due to an electric field. Similarly, this constitutive parameter is complex and thus can be written as $\bar{\bar{\sigma}} = \bar{\bar{\sigma}}' - i\bar{\bar{\sigma}}''$ where $\bar{\bar{\sigma}}$ and $\bar{\bar{\sigma}}'$ only contain real components. Rewriting the electric current density $\mathbf{J}$ as the sum of a source term $\mathbf{J}_e$ and a conduction term $\mathbf{J}_c$, we obtain,

$$\mathbf{J} = \mathbf{J}_e + \mathbf{J}_c = \mathbf{J}_e + \bar{\bar{\sigma}}\mathbf{E} \tag{A.22}$$

Although the electric conductivity and electric permittivity derive from different phenomena, their respective contributions cannot be differentiated. In time harmonic representation we use the complex effective permittivity defined as,

$$\bar{\bar{\tilde{\epsilon}}} = \left(\bar{\bar{\epsilon}}' + \frac{\bar{\bar{\sigma}}''}{\omega}\right) - i\left(\bar{\bar{\epsilon}}'' + \frac{\bar{\bar{\sigma}}'}{\omega}\right) = \bar{\bar{\tilde{\epsilon}}}' - i\bar{\bar{\tilde{\epsilon}}}'' \tag{A.23}$$

The complex effective permittivity is often normalized and we thus use the relative permittivity $\bar{\bar{\tilde{\epsilon}}}_r$ defined as $\bar{\bar{\tilde{\epsilon}}}_r = \bar{\bar{\tilde{\epsilon}}}/\epsilon_0$.

The magnetic permeability

The magnetic permeability $\bar{\bar{\mu}}$ describes magnetic induction phenomena locally. Similarly to the electric permittivity, it is a complex operator which we can write

as $\bar{\bar{\mu}} = \bar{\bar{\mu}}' - i\bar{\bar{\mu}}''$. The relative magnetic permeability is defined as $\bar{\bar{\mu}}_r = \bar{\bar{\mu}}/\mu_0$. Practically, materials sounded in planetary sounding radar react very little to magnetic fields, and we will consider in most cases the permeability to be equal to μ_0 (i.e. $\bar{\bar{\mu}}_r = \bar{\bar{\mathcal{I}}}$).

B

DIRECT PROBLEM FORMULATION

Don't point that gun at him,
he's an unpaid intern.

— Steve Zissou

We derive in this section the mathematical formulations from the planetary sounding radar problem. As a foreword I deeply apologize to all the people who will find the mathematics rather weak and incomplete in this manuscript. I did try my best to combine the correctness of the formulations with a somewhat readability and I sincerely hope you will forgive me for doing so.

B.1 ELECTROMAGNETIC WAVE SCATTERING

We shall derive here formulations for the direct problem in planetary radar sounding using equivalence principles. This section is largely inspired by the literature and relies on well-known formulations (e.g. [Kong, 2000; Lakhal, 2006; Warnick, 1997]). The notations used throughout the sections are detailed in appendix A.

Following [Lakhal, 2006], let $\Omega \in \mathbb{R}^3$ be an open set and F be a complex-valued vector field on $\mathbb{R}^3$. We say that F is a regular current field on Ω if F is a continuous current field on Ω and admits a divergence field $\nabla \cdot F$, which is continuous on Ω. We say that F is a regular electromagnetic field on Ω if F is a continuous electromagnetic field on Ω and admits a curl field $\nabla \times F$, which is continuous on Ω.

B.1.1 *The Stratton-Chu formulation*

We give here a general integral result which we shall use to derive a surface boundary formulation. Let Ω be a bounded domain in $\mathbb{R}^3$ with a piecewise *smooth* boundary $\partial\Omega$. For the regular current fields $\{\mathbf{J}_e, \mathbf{J}_m\}$ on Ω, and homogeneous complex electrical permittivity $\tilde{\bar{\epsilon}} = \tilde{\epsilon} \cdot \bar{\bar{\mathbf{I}}}$ and homogeneous complex magnetic permeability $\tilde{\bar{\mu}} = \tilde{\mu} \cdot \bar{\bar{\mathbf{I}}}$, we consider the direct source problem of determining the regular electromagnetic fields $\mathbf{E}$ and $\mathbf{H}$, on Ω, solving,

$$\nabla \times \mathbf{H} + i\omega\tilde{\epsilon}\mathbf{E} = \mathbf{J}_e \tag{B.1}$$
$$\nabla \times \mathbf{E} - i\omega\tilde{\mu}\mathbf{H} = -\mathbf{J}_m \tag{B.2}$$

The Stratton-Chu formulation states that the electromagnetic fields which are solutions to the homogeneous Maxwell's equations inside $\Omega \subset \mathbb{R}^3$, are completely determined from the volume densities of current sources $\{\mathbf{J}_e, \mathbf{J}_m\}$ and

the value of the electromagnetic fields on the boundary $\partial\Omega$ (see [Lakhal, 2006; Araque Quijano and Vecchi, 2010]),

$$\begin{aligned}\mathbf{E}(\mathbf{x}_0) = \int_\Omega \Big[& i\omega\tilde{\mu}\, g(\mathbf{x}_0,\mathbf{x})\, \mathbf{J}_e(\mathbf{x}) + \nabla g(\mathbf{x}_0,\mathbf{x}) \times \mathbf{J}_m(\mathbf{x}) - \\ & i(\omega\tilde{\epsilon})^{-1}\, \nabla g(\mathbf{x}_0,\mathbf{x})\, \nabla\cdot \mathbf{J}_e(\mathbf{x}) \Big] d\mathbf{x} + \\ \int_{\partial\Omega} \Big[& -i\omega\tilde{\mu} \Big[\hat{\mathbf{n}}\times\mathbf{H}\Big](\mathbf{x})\, g(\mathbf{x}_0,\mathbf{x}) - \\ & \Big[\hat{\mathbf{n}}\cdot\mathbf{E}\Big](\mathbf{x})\, \nabla g(\mathbf{x}_0,\mathbf{x}) + \nabla g(\mathbf{x}_0,\mathbf{x}) \times \Big[\hat{\mathbf{n}}\times\mathbf{E}\Big](\mathbf{x}) \Big] d\sigma(\mathbf{x})\end{aligned} \tag{B.3}$$

$$\begin{aligned}\mathbf{H}(\mathbf{x}_0) = \int_\Omega \Big[& i\omega\tilde{\epsilon}\, g(\mathbf{x}_0,\mathbf{x})\, \mathbf{J}_m(\mathbf{x}) - \nabla g(\mathbf{x}_0,\mathbf{x}) \times \mathbf{J}_e(\mathbf{x}) - \\ & i(\omega\tilde{\mu})^{-1}\, \nabla g(\mathbf{x}_0,\mathbf{x})\, \nabla\cdot \mathbf{J}_m(\mathbf{x}) \Big] d\mathbf{x} + \\ \int_{\partial\Omega} \Big[& i\omega\tilde{\epsilon} \Big[\hat{\mathbf{n}}\times\mathbf{E}\Big](\mathbf{x})\, g(\mathbf{x}_0,\mathbf{x}) - \\ & \Big[\hat{\mathbf{n}}\cdot\mathbf{H}\Big](\mathbf{x})\, \nabla g(\mathbf{x}_0,\mathbf{x}) + \nabla g(\mathbf{x}_0,\mathbf{x}) \times \Big[\hat{\mathbf{n}}\times\mathbf{H}\Big](x) \Big] d\sigma(\mathbf{x})\end{aligned} \tag{B.4}$$

with the scalar Green's function g satisfying the Helmholtz equation,

$$\left(\nabla^2 + \omega^2\tilde{\epsilon}\tilde{\mu}\right) g(\mathbf{x}_0,\mathbf{x}) = -\delta(\mathbf{x}-\mathbf{x}_0) \tag{B.5}$$

In all the previous equations, $\hat{\mathbf{n}}$ denotes the normal unit vector to the boundary $\partial\Omega$ directed into the exterior of Ω. For three-dimensional problems, we recall that the scalar Green's function – for isotropic media – is,

$$g(\mathbf{x}_0,\mathbf{x}) = \frac{e^{ik|\mathbf{x}-\mathbf{x}_0|}}{4\pi|\mathbf{x}-\mathbf{x}_0|} \tag{B.6}$$

We have made use of the wavenumber k which we shall define when it makes any sense as $k = \omega\sqrt{\tilde{\mu}\tilde{\epsilon}}$. From now on, we shall use a more compact form of these equations using dyads. This representation allows to make use of the boundary tangential fields alone in the boundary integral,

$$\begin{aligned}\mathbf{E}(\mathbf{x}_0) = \int_\Omega \Big[& i\omega\tilde{\mu}\, \bar{\bar{\mathbf{G}}}(\mathbf{x}_0,\mathbf{x})\cdot\mathbf{J}_e(\mathbf{x}) + \nabla\times\bar{\bar{\mathbf{G}}}(\mathbf{x}_0,\mathbf{x})\cdot\mathbf{J}_m(\mathbf{x}) \Big] d\sigma(\mathbf{x}) - \\ \int_{\partial\Omega} \Big[& i\omega\tilde{\mu}\, \bar{\bar{\mathbf{G}}}(\mathbf{x}_0,\mathbf{x})\cdot\Big[\hat{\mathbf{n}}\times\mathbf{H}\Big](\mathbf{x}) - \nabla\times\bar{\bar{\mathbf{G}}}(\mathbf{x}_0,\mathbf{x})\cdot\Big[\hat{\mathbf{n}}\times\mathbf{E}\Big](\mathbf{x}) \Big] d\sigma(\mathbf{x})\end{aligned} \tag{B.7}$$

$$\begin{aligned}\mathbf{H}(\mathbf{x}_0) = \int_\Omega \Big[& -i\omega\tilde{\epsilon}\, \bar{\bar{\mathbf{G}}}(\mathbf{x}_0,\mathbf{x})\cdot\mathbf{J}_m(\mathbf{x}) + \nabla\times\bar{\bar{\mathbf{G}}}(\mathbf{x}_0,\mathbf{x})\cdot\mathbf{J}_e(\mathbf{x}) \Big] d\sigma(\mathbf{x}) - \\ \int_{\partial\Omega} \Big[& -i\omega\tilde{\epsilon}\, \bar{\bar{\mathbf{G}}}(\mathbf{x}_0,\mathbf{x})\cdot\Big[\hat{\mathbf{n}}\times\mathbf{E}\Big](\mathbf{x}) + \nabla\times\bar{\bar{\mathbf{G}}}(\mathbf{x}_0,\mathbf{x})\cdot\Big[\hat{\mathbf{n}}\times\mathbf{H}\Big](\mathbf{x}) \Big] d\sigma(\mathbf{x})\end{aligned} \tag{B.8}$$

with,

$$\bar{\bar{\mathbf{G}}}(\mathbf{x}_0, \mathbf{x}) = \left[\bar{\bar{\mathbf{I}}} + \frac{1}{\omega^2 \tilde{\epsilon}\tilde{\mu}} \nabla\nabla\right] g(\mathbf{x}_0, \mathbf{x}) \tag{B.9}$$

The previous formulation is purely mathematical, we shall now detail how this formulation can be used in planetary sounding radar with first a volume integral formulation and then its equivalent surface formulation.

A volume integral formulation

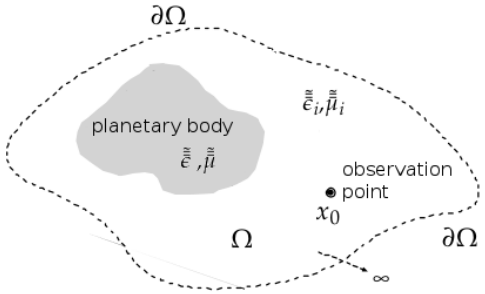

Figure 28: Schematic representation of the geometry of the volume integral formulation where $\{\bar{\bar{\epsilon}}_i, \bar{\bar{\mu}}_i\}$ characterize the atmospheric medium and $\{\bar{\bar{\epsilon}}, \bar{\bar{\mu}}\}$ characterize the planetary body. The observation point represents the radar location.

We define regular current fields $\{\mathbf{J}_{e,i}, \mathbf{J}_{m,i}\}$ on Ω (for instance radar sources) where we define homogeneous complex electrical permittivity $\bar{\bar{\epsilon}}_i = \tilde{\epsilon}_i \cdot \bar{\bar{\mathbf{I}}}$ and homogeneous complex magnetic permeability $\bar{\bar{\mu}}_i = \tilde{\mu}_i \cdot \bar{\bar{\mathbf{I}}}$ (for instance a homogeneous background medium). Let us define regular electromagnetic fields $\mathbf{E}_i$ and $\mathbf{H}_i$ on Ω such that,

$$\nabla \times \mathbf{H}_i + i\omega\tilde{\epsilon}_i \mathbf{E}_i = \mathbf{J}_{e,i} \tag{B.10}$$
$$\nabla \times \mathbf{E}_i - i\omega\tilde{\mu}_i \mathbf{H}_i = -\mathbf{J}_{m,i} \tag{B.11}$$

We consider the direct source problem of determining the regular electromagnetic fields $\mathbf{E}$ and $\mathbf{H}$, on Ω such that the scattered fields express as $\mathbf{E}_s = \mathbf{E} - \mathbf{E}_i$ and $\mathbf{H}_s = \mathbf{H} - \mathbf{H}_i$,

$$\nabla \times \mathbf{H} + i\omega\bar{\bar{\epsilon}} \cdot \mathbf{E} = \mathbf{J}_{e,i} \tag{B.12}$$
$$\nabla \times \mathbf{E} - i\omega\bar{\bar{\mu}} \cdot \mathbf{H} = -\mathbf{J}_{m,i} \tag{B.13}$$

Practically in planetary sounding radar, scattered fields are the radiated fields induced by the planetary body (see figure 28). Using induced electric and magnetic current sources $\mathbf{J}_e$ and $\mathbf{J}_m$ defined by,

$$\mathbf{J}_e = i\omega \left(\bar{\bar{\epsilon}}_i - \bar{\bar{\epsilon}}\right) \cdot \mathbf{E} \tag{B.14}$$
$$\mathbf{J}_m = i\omega \left(\bar{\bar{\mu}}_i - \bar{\bar{\mu}}\right) \cdot \mathbf{H} \tag{B.15}$$

The problem naturally reduces to a direct source problem in a homogeneous medium $\{\tilde{\bar{\epsilon}}_i, \tilde{\bar{\mu}}_i\}$ for the induced sources $\mathbf{J}_e$ and $\mathbf{J}_m$,

$$\nabla \times \mathbf{H}_s + i\omega\tilde{\epsilon}_i \mathbf{E}_s = \mathbf{J}_e \tag{B.16}$$
$$\nabla \times \mathbf{E}_s - i\omega\tilde{\mu}_i \mathbf{H}_s = -\mathbf{J}_m \tag{B.17}$$

Imposing the boundary surface integral term to be null in equations B.3 and B.4, we can write (Stratton-Chu formula),

$$\begin{aligned}\mathbf{E}(\mathbf{x}_0) = \mathbf{E}_i(\mathbf{x}_0) + \int_\Omega \Big[&- \omega^2 \tilde{\mu}_i \, g(\mathbf{x}_0, \mathbf{x}) \Big[\left(\tilde{\bar{\epsilon}}_i - \tilde{\bar{\epsilon}}\right) \cdot \mathbf{E} \Big](\mathbf{x}) + \\ &i\omega \nabla g(\mathbf{x}_0, \mathbf{x}) \times \Big[\left(\tilde{\bar{\mu}}_i - \tilde{\bar{\mu}}\right) \cdot \mathbf{H} \Big](\mathbf{x}) + \\ &\tilde{\epsilon}_i^{-1} \nabla g(\mathbf{x}_0, \mathbf{x}) \, \nabla \cdot \Big[\left(\tilde{\bar{\epsilon}}_i - \tilde{\bar{\epsilon}}\right) \cdot \mathbf{E} \Big](\mathbf{x}) \Big] d\mathbf{x}\end{aligned} \tag{B.18}$$

$$\begin{aligned}\mathbf{H}(\mathbf{x}_0) = \mathbf{H}_i(\mathbf{x}_0) + \int_\Omega \Big[&- \omega^2 \tilde{\epsilon} \, g(\mathbf{x}_0, \mathbf{x}) \Big[\left(\tilde{\bar{\mu}}_i - \tilde{\bar{\mu}}\right) \cdot \mathbf{H} \Big](\mathbf{x}) - \\ &i\omega \nabla g(\mathbf{x}_0, \mathbf{x}) \times \Big[\left(\tilde{\bar{\epsilon}}_i - \tilde{\bar{\epsilon}}_i\right) \cdot \mathbf{E} \Big](\mathbf{x}) + \\ &\tilde{\mu}_i^{-1} \nabla g(\mathbf{x}_0, \mathbf{x}) \, \nabla \cdot \Big[\left(\tilde{\bar{\mu}}_i - \tilde{\bar{\mu}}\right) \cdot \mathbf{H} \Big](\mathbf{x}) \Big] d\mathbf{x}\end{aligned} \tag{B.19}$$

Note: We have avoided tedious discussions on boundary conditions by imposing boundary integrals to be null somehow. We could have also used radiation conditions along with localized sources in Ω and let $\partial\Omega$ go to infinity to obtain a similar result.

This formulation allows to derive electromagnetic fields from the knowledge of the sources and of the permittivity and permeability distributions. In planetary sounding radar and GPR such formulation allows to perform 3D imaging of the planetary body geophysical properties (e.g. [Deming and Devaney, 1997]).

The Huygens-Fresnel's principle

Although the last formulation is widely used in inverse scattering problems, we shall focus on surface integral formulations. If we assume the current sources within Ω in equation B.1 to be due to radar sources, the Stratton-Chu formulation is equivalent to *the Huygens-Fresnel's principle*. The volume integral terms in equations B.3 and B.4 can be interpreted as the incident fields $\{\mathbf{E}_i, \mathbf{H}_i\}$ with $\mathbf{E}_s = \mathbf{E} - \mathbf{E}_i$ and $\mathbf{H}_s = \mathbf{H} - \mathbf{H}_i$ allowing us to write,

Fundamentally, Huygens-Fresnel's principle derives from Stokes generalized theorem.

$$\mathbf{E}_s(\mathbf{x}_0) = \int_{\partial\Omega} \Big[- i\omega\tilde{\mu} \bar{\bar{\mathbf{G}}}(\mathbf{x}_0, \mathbf{x}) \cdot \Big[\hat{\mathbf{n}}_1 \times \mathbf{H}\Big](\mathbf{x}) + \nabla \times \bar{\bar{\mathbf{G}}}(\mathbf{x}_0, \mathbf{x}) \cdot \Big[\hat{\mathbf{n}}_1 \times \mathbf{E}\Big](\mathbf{x}) \Big] d\sigma(\mathbf{x}) \tag{B.20}$$

$$\mathbf{H}_s(\mathbf{x}_0) = \int_{\partial\Omega} \Big[i\omega\tilde{\epsilon} \, \bar{\bar{\mathbf{G}}}(\mathbf{x}_0, \mathbf{x}) \cdot \Big[\hat{\mathbf{n}}_1 \times \mathbf{E}\Big](\mathbf{x}) - \nabla \times \bar{\bar{\mathbf{G}}}(\mathbf{x}_0, \mathbf{x}) \cdot \Big[\hat{\mathbf{n}}_1 \times \mathbf{H}\Big](\mathbf{x}) \Big] d\sigma(\mathbf{x}) \tag{B.21}$$

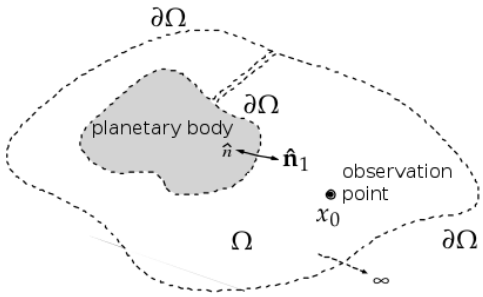

Figure 29: Schematic representation of the geometry for planetary sounding radar when using a surface formulation with a surface conforming locally with the planetary body (i.e. Huygens-Fresnel's principle). The observation point represents the radar location.

$\hat{\mathbf{n}}_1$ is now the normal to the boundary $\partial\Omega$ pointing inward the domain Ω. Additionally, we may write for the sake of simplicity, $\mathbf{E}_{\parallel} = [\hat{\mathbf{n}}_1 \times \mathbf{E}]$ and $\mathbf{H}_{\parallel} = [\hat{\mathbf{n}}_1 \times \mathbf{H}]$. In all the coming sections, we will simply refer to this formulation as the Huygens' principle. This formulation can be generalized to inhomogeneous bianisotropic media (see [Monzon, 1993; Warnick and Arnold, 1997]). The problem described here directly relates to planetary sounding if we assume incident fields to be the radar sources and if we let $\partial\Omega$ conforms locally with the planetary surface body S and $\partial\Omega$ go to infinity otherwise (see figure 29). Using Huygens' principle and further assuming radiation conditions such that fields vanish at infinity, we can write,

$$\mathbf{E}_s(\mathbf{x}_0) = \int_S \Big[-i\omega\tilde{\mu}_i \bar{\bar{\mathbf{G}}}(\mathbf{x}_0, \mathbf{x}) \cdot \mathbf{H}_{\parallel}(\mathbf{x}) + \nabla \times \bar{\bar{\mathbf{G}}}(\mathbf{x}_0, \mathbf{x}) \cdot \mathbf{E}_{\parallel}(\mathbf{x}) \Big] d\sigma(\mathbf{x}) \tag{B.22}$$

$$\mathbf{H}_s(\mathbf{x}_0) = \int_S \Big[i\omega\tilde{\epsilon}_i \bar{\bar{\mathbf{G}}}(\mathbf{x}_0, \mathbf{x}) \cdot \mathbf{E}_{\parallel}(\mathbf{x}) - \nabla \times \bar{\bar{\mathbf{G}}}(\mathbf{x}_0, \mathbf{x}) \cdot \mathbf{H}_{\parallel}(\mathbf{x}) \Big] d\sigma(\mathbf{x}) \tag{B.23}$$

$\{\mathbf{E}_s, \mathbf{H}_s\}$ now represents the electromagnetic field scattered from the planetary surface. This formulation does not explicitly refer to material properties of the planetary body, however the information is contained within tangential fields. The choice of the boundary integral formulation was originally motivated by the limited available forward modelling codes (see section 4) and by the geometry of the problem (a planetary body within its atmospheric environment can be seen as a two media problem in a first approach). It proves to be a powerful formulation as we will see in the coming sections.

We have worked mostly with isotropic homogeneous media but formulations exist for linear bianisotropic inhomogeneous media (see [Monzon, 1993; Warnick and Arnold, 1997]).

Note: Surface formulations do not necessarily require the surface to conform with the planetary body.

B.2 INSTRUMENT CHARACTERISTICS AND ON-BOARD PROCESSING

Practically, in planetary sounding radar, the target region is the planetary body along with the atmosphere and plasma environment (e.g. MARSIS). The data are measured on the subset Γ of $\mathbb{R}^3$, which corresponds in our case to a set of points on different orbits exterior to the planetary body. Let $I \subset \mathbb{N}$ denote the experiment-set with p elements. For each $\alpha \in I$, we are given an operator $\bar{\bar{\mathbf{M}}}^{\alpha}$, called the measurement operator for the α^{th} experiment, which to the state-space elements $\{\mathbf{E}_s^{\alpha}, \mathbf{H}_s^{\alpha}\}_{\alpha \in I}$ associates an element $\mathbf{d}(\alpha, \omega_0) \in \mathbb{C}^k$ from the k-

dimensions data manifold. In most cases, the measurement operators $\bar{\bar{\mathbf{M}}}^{\alpha}$ can be regarded as linear. In sounding radar experiments we shall write,

$$\mathbf{d}(\beta,\omega_0) = \left[\bar{\bar{\mathbf{M}}}\cdot\mathbf{E}_s\right]^{\beta}(\omega_0) = \sum_{\alpha\in I}\int_{\omega}\left[\bar{\bar{\mathbf{C}}}^{\beta,\alpha}(\omega,\omega_0)\cdot\int_{\partial\Omega'}\left[\bar{\bar{\mathbf{K}}}_e^{\alpha}(\mathbf{x}',\omega,\omega_0)\cdot\mathbf{E}_s^{\alpha}(\mathbf{x}',\omega)d\sigma(\mathbf{x}')\right]d\omega\right] \tag{B.24}$$

$\partial\Omega'$ denotes an arbitrary closed surface enclosing the radar antenna whereas superscripts α and β denote radar acquisitions and experiment records respectively. The sum over α is due to the on-board processing. For instance, it may include a pre-summing of over several acquisitions known as the unfocused synthetic aperture processing. $\mathbf{K}_e^{\alpha}$ accounts for the antenna gain (antenna pattern, polarization), $\bar{\bar{\mathbf{C}}}^{\alpha,\beta}$ accounts for on-board processing and for the electronic instrument response. $\mathbf{E}_s^{\alpha}$ is acquisition dependant since tangential fields $\mathbf{E}_{\parallel}$ and $\mathbf{H}_{\parallel}$ depends on incident fields $\mathbf{E}_i^{\alpha}$. $\bar{\bar{\mathbf{K}}}_e^{\alpha}$ depends on the definition of the closed surface $\partial\Omega'$ on which they operate (a unit radius sphere centred on the antenna for instance). Interestingly, we can rewrite the previous equation using only tangential fields on the planetary surface $\partial\Omega$ using B.22 and B.23,

$$\mathbf{d}(\beta,\omega_0) = \sum_{\alpha\in I}\left[\int_{\omega}\bar{\bar{\mathbf{C}}}^{\alpha,\beta}(\omega,\omega_0)\cdot\left[\int_{\partial\Omega'}\bar{\bar{\mathbf{K}}}_e^{\alpha}(\mathbf{x}',\omega,\omega_0)\cdot\left[\int_S\left(-i\omega\tilde{\mu}_i\,\bar{\bar{\mathbf{G}}}(\mathbf{x}',\mathbf{x},\omega)\cdot\mathbf{H}_{\parallel}^{\alpha}(\mathbf{x},\omega)+\nabla\times\bar{\bar{\mathbf{G}}}(\mathbf{x}',\mathbf{x},\omega)\cdot\mathbf{E}_{\parallel}^{\alpha}(\mathbf{x},\omega)\right)d\sigma(\mathbf{x})\right]d\sigma(\mathbf{x}')\right]d\omega\right] \tag{B.25}$$

Note: For a given experiment j, the data element $\mathbf{d}^j$ is such that $\mathbf{d}^j \subset \mathbb{C}^D$ where D is the number of canals of the instruments.

As most radar instruments in planetary sounding radar are linear antennas, we provide a rapid overview of radiated fields. We place a wire antenna along $\hat{\mathbf{z}}$ direction centred on $\mathbf{x}_0$ with a vector current distribution $\mathbf{J}(\mathbf{x})$ along $\hat{\mathbf{z}}$ direction. In the far field approximation, the electric field $\mathbf{E}$ is along $\hat{\theta}$ direction and can be written as (e.g. [Kong, 2000]),

$$\mathbf{E}(\mathbf{x}) = i\omega\mu_i\frac{e^{ik|\mathbf{x}-\mathbf{x}_0|}}{4\pi|\mathbf{x}-\mathbf{x}_0|}f_\theta\hat{\theta} \tag{B.26}$$

Hats denote unit vectors in this context. $\hat{\theta}$ is such that $\hat{\mathbf{z}} = \hat{\mathbf{r}}\cos\theta - \hat{\theta}\sin\theta$ with $\hat{\mathbf{r}} = (\mathbf{x}-\mathbf{x}_0)/|\mathbf{x}-\mathbf{x}_0|$ and $\cos\theta = \hat{\mathbf{z}}\cdot\hat{\mathbf{r}}$. f_θ is the $\hat{\theta}$ component of the vector current moment and is defined as,

$$f_\theta = \int_\Omega \mathbf{J}(\mathbf{x})\cdot\hat{\theta}.e^{-i\hat{\mathbf{k}}\cdot\mathbf{x}}d\mathbf{x} \tag{B.27}$$

For a current distribution $\mathbf{J}(\mathbf{x}) = I_0\sin\left(k(l-|\mathbf{x}\cdot\hat{\mathbf{z}}|)\right)$ with an antenna length $2l$, we obtain,

$$f_\theta = -\sin\theta\frac{2I_0}{k}(1-\cos kl) \tag{B.28}$$

Finally, we may point out that it is equivalent to work in the frequency or time domain when dealing with full waveform data. However, it is also common to conduct radar data analysis with the amplitude of baseband Fourier transformed signals (i.e. removal of the carrier phase of the radar signal).

B.3 HUYGENS-FRESNEL IN THE FAR FIELD APPROXIMATION

In planetary sounding radar, the sources and receivers are usually located several hundred of wavelength away to the surface. We can thus simplify the dyadic Green's functions B.9 using the far field approximation [Kong, 2000],

$$\bar{\bar{\mathbf{G}}}(\mathbf{x}_0, \mathbf{x}) \approx \left[\bar{\bar{\mathbf{I}}} - \hat{\mathbf{k}}_\mathbf{s}\hat{\mathbf{k}}_\mathbf{s}\right] \frac{e^{ik|\mathbf{x}_0 - \mathbf{x}|}}{4\pi|\mathbf{x}_0 - \mathbf{x}|} \tag{B.29}$$

Substituting the previous equation in B.22 we obtain,

$$\mathbf{E}_s(\mathbf{x}_0) = \int_S \left[\bar{\bar{\mathbf{I}}} - \hat{\mathbf{k}}_\mathbf{s}\hat{\mathbf{k}}_\mathbf{s}\right] \left(\eta \mathbf{H}_\parallel(\mathbf{x}) + \hat{\mathbf{k}}_s \times \mathbf{E}_\parallel(\mathbf{x})\right) \frac{e^{ik|\mathbf{x}_0 - \mathbf{x}|}}{4\pi|\mathbf{x}_0 - \mathbf{x}|} d\mathbf{x} \tag{B.30}$$

Where $\hat{\mathbf{k}}_s$ is the unit vector pointing in the scattering direction.

B.4 FIELDS ON THE BOUNDARY SURFACE

Huygens' principle relies on the knowledge of tangential fields on the boundary surface. Practically, fields on the boundary surface are a combination of incident fields and scattered fields. As we have seen in chapter B, heterogeneities within the planetary body are sources of scattering and account for boundary fields. From a mathematical point of view, given a set of known sources in the interior volume Ω, the material acts as functions $\{r_e, r_h\}$ of incident fields $\{\mathbf{E}_i, \mathbf{H}_i\} \in \partial\Omega$,

$$\mathbf{E}_s = r_e\left(\mathbf{E}_i, \mathbf{H}_i\right) \tag{B.31}$$
$$\mathbf{H}_s = r_h\left(\mathbf{E}_i, \mathbf{H}_i\right) \tag{B.32}$$

In the most general case $\{r_e, r_h\}$ depend on the incident field and the material properties and cannot be expressed analytically. Let us define $(\hat{\mathbf{k}}_i, \hat{\mathbf{p}}_i, \hat{\mathbf{q}}_i)$ as a local orthonormal system on Ω with,

$$\hat{\mathbf{q}}_i = \frac{\hat{\mathbf{k}}_i \times \hat{\mathbf{n}}}{|\hat{\mathbf{k}}_i \times \hat{\mathbf{n}}|} \tag{B.33}$$
$$\hat{\mathbf{p}}_i = \hat{\mathbf{q}}_i \times \hat{\mathbf{k}}_i \tag{B.34}$$

Using these notations, we now choose to write tangential fields on the boundary surface – for $\mathbf{x} \in S$ – as,

$$\mathbf{E}_\parallel(\mathbf{x}) = \gamma_0^E . \hat{\mathbf{n}} \times \hat{\mathbf{q}}_i + \gamma_1^E . \hat{\mathbf{q}}_i \tag{B.35}$$

$$\mathbf{H}_\parallel(\mathbf{x}) = \gamma_0^H . \hat{\mathbf{n}} \times \hat{\mathbf{q}}_i + \gamma_1^H . \hat{\mathbf{q}}_i \tag{B.36}$$

In the previous equations, $\hat{\mathbf{n}}$ denotes the normal unit vector pointing into the volume interior Ω (i.e. the atmospheric environment). We have made use here of γ_0^E, γ_1^E, γ_0^H and γ_1^H which are complex functions. They depend on the incident field and the material properties. At this point, we can ask ourselves what the parameters γ_0^E, γ_1^E, γ_0^H and γ_1^H physically represent. As we have previously discussed, these parameters locally relate incident fields to scattered fields. In short, these parameters permit to reconstruct electromagnetic fields on $\partial\Omega$. They are thus functions acting on local fields on $\partial\Omega$ in the time domain (or frequency domain). We shall discuss here three examples to illustrate how these functions may relate to material properties.

Homogeneous media case

When the boundary surface $\partial\Omega$ delimits two homogeneous isotropic non-diffusive media and if we assume large radii of curvatures of the surface with regard to the incident wavelength, then γ_0^E, γ_1^E, γ_0^H and γ_1^H are closely related to local transverse electric and transverse magnetic Fresnel's reflection coefficients. For isotropic media, Fresnel's coefficients read [Kong, 2000; Løseth et al., 2006],

$$R^{TE} = \frac{1 - p_{1,2}^{TE}}{1 + p_{1,2}^{TE}} \tag{B.37}$$

$$R^{TM} = \frac{1 - p_{1,2}^{TM}}{1 + p_{1,2}^{TM}} \tag{B.38}$$

$$p_{1,2}^{TE} = \frac{\mu_1 k_{\perp,2}}{\mu_2 k_{\perp,1}} \tag{B.39}$$

$$p_{1,2}^{TM} = \frac{\epsilon_1 k_{\perp,2}}{\epsilon_2 k_{\perp,1}} \tag{B.40}$$

$$k_{\parallel,1}^2 + k_{\perp,1}^2 = \omega^2 \mu_1 \epsilon_1 \tag{B.41}$$

$$k_{\parallel,1}^2 + k_{\perp,2}^2 = \omega^2 \mu_2 \epsilon_2 \tag{B.42}$$

Where μ_1 and μ_2 are the upper and lower medium magnetic permeability while ϵ_1 and ϵ_2 are the upper and lower medium electric permittivity respectively. $k_{\parallel,i}$ and $k_{\perp,i}$ with $i = \{1,2\}$ are the components of the wave vector $\mathbf{k}$ in the plane of incidence and normal to the plane of incidence respectively. Note that $k_{\parallel,1} = k_{\parallel,2}$ by virtue of phase matching as detailed in [Kong, 2000; Løseth et al., 2006]. A general understanding of Snell-Descartes and Fresnel's laws is provided in the following paper [Dupertuis and Proctor, 1994]. Eventually we can rewrite equations B.35 and B.36,

$$\begin{aligned}\mathbf{E}_\parallel(\mathbf{x}) = & E_i(\mathbf{x}).\Big((\hat{\mathbf{n}} \times \hat{\mathbf{q}}_i) . \Big[(\hat{\mathbf{e}}_i \cdot \hat{\mathbf{q}}_i) . \left(1 + R^{TE}\right) \Big] + \\ & \hat{\mathbf{q}}_i . \left(\hat{\mathbf{n}} \cdot \hat{\mathbf{k}}_i\right) . \Big[(\hat{\mathbf{e}}_i \cdot \hat{\mathbf{p}}_i) . \left(1 - R^{TM}\right) \Big] \Big)\end{aligned} \tag{B.43}$$

$$\begin{aligned}\mathbf{H}_\parallel(\mathbf{x}) = & \frac{1}{\eta} . E_i(\mathbf{x}).\Big((\hat{\mathbf{n}} \times \hat{\mathbf{q}}_i) . \Big[(\hat{\mathbf{e}}_i \cdot \hat{\mathbf{p}}_i) . \left(1 + R^{TM}\right) \Big] \\ & - \hat{\mathbf{q}}_i . \left(\hat{\mathbf{n}} \cdot \hat{\mathbf{k}}_i\right) . \Big[(\hat{\mathbf{e}}_i \cdot \hat{\mathbf{q}}_i) . \left(1 - R^{TE}\right) \Big] \Big)\end{aligned} \tag{B.44}$$

The equations obtained do not take into account multiple reflections that might

occur at the surface. This approximation may be not valid at all, especially when dealing with rugged surface as surface scattering will spatially couple fields over $\partial\Omega$ (e.g. [Fung et al., 1992; Fung and Chan, 1971]).

Scattering by random rough surface case

We assume the exterior medium (as opposed to the interior volume Ω) to be a homogeneous material with a rough interface between the interior and exterior media. If $\partial\Omega$ conforms locally *on the average* with the interface of the two media such as the fluctuation around $\partial\Omega$ can be regarded as random locally (see figure 30), we can write,

$$\begin{aligned} < \mathbf{E}_{\parallel} > (\mathbf{x}) = & E_i(\mathbf{x}).\Big((\hat{\mathbf{n}} \times \hat{\mathbf{q}}_i) . \Big[(\hat{\mathbf{e}}_i \cdot \hat{\mathbf{q}}_i) . \Big(1 + R_{TE}^{TE}\Big) + (\hat{\mathbf{e}}_i \cdot \hat{\mathbf{p}}_i) . R_{TM}^{TE} \Big] + \\ & \hat{\mathbf{q}}_i . \Big(\hat{\mathbf{n}} \cdot \hat{\mathbf{k}}_i\Big) . \Big[(\hat{\mathbf{e}}_i \cdot \hat{\mathbf{p}}_i) . \Big(1 - R_{TM}^{TM}\Big) - (\hat{\mathbf{e}}_i \cdot \hat{\mathbf{q}}_i) . R_{TE}^{TM} \Big] \Big) \end{aligned} \tag{B.45}$$

$$\begin{aligned} < \mathbf{H}_{\parallel} > (\mathbf{x}) = & \frac{1}{\eta} \cdot E_i(\mathbf{x}) \cdot \Big((\hat{\mathbf{n}} \times \hat{\mathbf{q}}_i) \cdot \Big[(\hat{\mathbf{e}}_i \cdot \hat{\mathbf{p}}_i) \cdot \Big(1 + R_{TM}^{TM}\Big) + (\hat{\mathbf{e}}_i \cdot \hat{\mathbf{q}}_i) \cdot R_{TE}^{TM} \Big] \\ & - \hat{\mathbf{q}}_i . \Big(\hat{\mathbf{n}} \cdot \hat{\mathbf{k}}_i\Big) . \Big[(\hat{\mathbf{e}}_i \cdot \hat{\mathbf{q}}_i) . \Big(1 - R_{TE}^{TE}\Big) - (\hat{\mathbf{e}}_i \cdot \hat{\mathbf{p}}_i) . R_{TM}^{TE} \Big] \Big) \end{aligned} \tag{B.46}$$

Figure 30: Random height fluctuations around a reference *smooth* surface. l and σ denote the correlation length and the standard deviation respectively of the height random fluctuation function defined when possible.

We have made use here of reflection parameters R_{TE}^{TE}, R_{TM}^{TE}, R_{TE}^{TM} and R_{TM}^{TM} which are complex coefficients. R_{TM}^{TE} and R_{TE}^{TM} are coupling coefficients that account for changes in the polarization with regard to the incident field due to the surface random fluctuations. $< \mathbf{E}_{\parallel} >$ and $< \mathbf{H}_{\parallel} >$ are local mean quantities on $\partial\Omega$. If random fluctuations are null, equations B.45 andB.46 simplify to equations B.43 andB.44 as $R_{TE}^{TE} = R^{TE}$, $R_{TM}^{TM} = R^{TM}$ and $R_{TM}^{TE} = R_{TE}^{TM} = 0$. Although this formulation may be useful in some cases, it may be preferable to work in the time domain with baseband signal (i.e. removal of the carrier phase of the radar signal) when dealing with random fluctuations. Electromagnetic signals in planetary radar sounding are characterized by a bandwidth centred at a given frequency (the carrier frequency). In terms of signal in time domain, this results roughly in an envelop containing a rapid varying carrier wave. As random fluctuation amplitudes around $\partial\Omega$ reach the carrier wavelength, the wavefront coherency is lost. From the electromagnetic signal point of view in time domain, there will be an addition of multiple random phased signals arriving at the same time. To be correct, time delays of the random phased signals are not identical but are very small in comparison to the time domain width of the envelop. At this point

the phase information is lost (i.e. incoherent signal) and the information of the signal is contained in the amplitude of the signal's envelop (i.e. the baseband signal). Due to the additivity of signal intensities in an incoherent regime, the incoherent scattered electromagnetic signal power P_s can be explicitly expressed in a surface integral form,

$$P_s^q(\mathbf{x}_0,t) = \int_{\partial\Omega} P_i^q\left(\mathbf{x}, t - \frac{|\mathbf{x}-\mathbf{x}_0|}{c}\right).\sigma_q^q + P_i^p\left(\mathbf{x}, t - \frac{|\mathbf{x}-\mathbf{x}_0|}{c}\right).\sigma_p^q d\sigma(\mathbf{x}) \tag{B.47}$$

$$P_s^p(\mathbf{x}_0,t) = \int_{\partial\Omega} P_i^p\left(\mathbf{x}, t - \frac{|\mathbf{x}-\mathbf{x}_0|}{c}\right).\sigma_p^p + P_i^q\left(\mathbf{x}, t - \frac{|\mathbf{x}-\mathbf{x}_0|}{c}\right).\sigma_q^p d\sigma(\mathbf{x}) \tag{B.48}$$

Where P_i denotes the incident electromagnetic signal power, c the velocity in Ω, superscripts the components along $\hat{\mathbf{q}}$ and $\hat{\mathbf{p}}$ and $(\hat{\mathbf{k}}_s, \hat{\mathbf{p}}, \hat{\mathbf{q}})$ is a local orthonormal system on Ω with,

$$\hat{\mathbf{q}} = \frac{\hat{\mathbf{k}}_s \times \hat{\mathbf{n}}}{|\hat{\mathbf{k}}_s \times \hat{\mathbf{n}}|} \tag{B.49}$$

$$\hat{\mathbf{p}} = \hat{\mathbf{q}} \times \hat{\mathbf{k}}_s \tag{B.50}$$

$\sigma_p^p, \sigma_p^p, \sigma_p^p$ and σ_p^p are real functions which depend on the geometry of the problem, on the statistical properties of the fluctuations, on the frequency of the signal and on the material properties. These functions naturally relate to the differential scattering cross sections (e.g. [Kong, 2000; Franceschetti et al., 1999; Fung and Chan, 1971; Løseth et al., 2006]). It is worth noting that this problem arises in planetary sounding radar due to the relatively small bandwidth with regard to the carrier frequency. As the bandwidth extends, the signal width in time domain diminishes and scattered signals arriving with different phases do not interfere anymore.

Scattering by a random exterior medium

We assume the exterior medium (as opposed to the interior volume Ω) to be a homogeneous scattering material and $\partial\Omega$ to conform with the interface of the volume Ω with this medium. This situation is very similar to the previous one as we can express the incoherent scattered electromagnetic signal power P_s in a surface integral form using the same conventions,

$$\begin{aligned} P_s^q(\mathbf{x}_0,t) &= \int_{\partial\Omega} P_i^q\left(\mathbf{x}, t - \frac{|\mathbf{x}-\mathbf{x}_0|}{c}\right).\sigma_q^q + P_i^p\left(\mathbf{x}, t - \frac{|\mathbf{x}-\mathbf{x}_0|}{c}\right).\sigma_p^q d\sigma(\mathbf{x}) \\ P_s^p(\mathbf{x}_0,t) &= \int_{\partial\Omega} P_i^p\left(\mathbf{x}, t - \frac{|\mathbf{x}-\mathbf{x}_0|}{c}\right).\sigma_p^p + P_i^q\left(\mathbf{x}, t - \frac{|\mathbf{x}-\mathbf{x}_0|}{c}\right).\sigma_q^p d\sigma(\mathbf{x}) \end{aligned} \tag{B.51}$$

$\{P_s^q, P_s^p\}$ is now governed through radiative transfer equations (e.g. [Ryzhik et al., 1996; Pierrat, 2007]). $\sigma_p^p, \sigma_p^p, \sigma_p^p$ and σ_p^p are real functions which depend on the geometry of the problem, on the statistical properties of the volume fluctuations, on the frequency of the signal and on the material properties (e.g. [Grimm et al., 2006]).

C

A MODERN FORMULATION OF THE PROBLEM

God help us, we're in the hands of engineers.

— Dr. Ian Malcolm

I have chosen to use differential forms to introduce the equations in this section. The purpose is two fold: (i) it allows a more consistent approach regarding the physics (we are now dealing with quantities to be integrated), (ii) it offers an insight of the different formalisms that exists to formulate Maxwell's equations. Furthermore, this formalism naturally relates to modern physics through differential geometry. This section was mostly inspired by [Matias, 2012; Warnick, 1997]. It seems differential geometry in electromagnetism has become a quite active field (e.g. [Teixeira, 2007; Warnick and Arnold, 1997; Deschamps, 1981; Lindell, 2005]) and offers interesting perspective in computational electromagnetism as detailed in [Desbrun et al., 2005]. On 3-manifold M we define $\Omega_l^k(M)$ as $\binom{k}{l}$-tensors antisymmetric in their k upper indices and l lower indices and $\Omega^k(M)$ more specifically as k-forms on M.

C.1 MAXWELL'S EQUATIONS USING DIFFERENTIAL GEOMETRY

Electromagnetic wave propagation is governed through *Maxwell's equations* (see [Matias, 2012]). On 3-manifold M, they read,

$$d\mathcal{E} = -\frac{\partial \mathcal{B}}{\partial t} \tag{C.1}$$

$$d\mathcal{H} = \frac{\partial \mathcal{D}}{\partial t} + \mathcal{J} \tag{C.2}$$

$$\mathcal{D} = \rho \tag{C.3}$$

$$\mathcal{B} = 0 \tag{C.4}$$

We can simplify the equations previously by working on 4-manifold $N = \mathbb{R} \times M$ such that the additional dimension corresponds to a time coordinate. We define forms $\mathcal{F}, \mathcal{G} \in \Omega^2(N)$ and $j \in \Omega^3(N)$,

$$\mathcal{F} = \mathcal{B} + \mathcal{E} \wedge dt \tag{C.5}$$

$$\mathcal{G} = \mathcal{D} - \mathcal{H} \wedge dt \tag{C.6}$$

$$j = \rho - \mathcal{J} \wedge dt \tag{C.7}$$

Using these forms, we can rewrite Maxwell's equations,

$$d\mathcal{F} = 0 \tag{C.8}$$

$$d\mathcal{G} = j \tag{C.9}$$

Where d is the exterior derivative on N. Formulations on 3-manifold and 4-manifold are equivalent (see [Matias, 2012]) although the latter provides a more elegant and compact result while the former allows convenient analogies with vector formulations. With this formalism, constitutive relations now reads,

$$\kappa : \Omega^2(N) \to \Omega^2(N) \tag{C.10}$$
$$\mathcal{G} = \kappa(\mathcal{F}) \tag{C.11}$$

Constitutive relation κ may be function of space and time coordinates, thermodynamical and continuum mechanical variables, or electromagnetic field strengths. We shall focus on linear media whereby using $\binom{2}{2}$-antisymmetric tensor $\kappa \in \Omega^2_2(N)$ as described in [Matias, 2012]. With coordinates $\{x^i\}_{i=0}^3$ for N, we can write (see [Matias, 2012]),

$$\kappa = \frac{1}{2}\kappa^{ij}_{lm} dx^l \otimes dx^m \otimes \frac{\partial}{\partial x^i} \otimes \frac{\partial}{\partial x^j} \tag{C.12}$$
$$\mathcal{D}_{ij} = \frac{1}{2}\kappa^{rs}_{ij}\mathcal{F}_{rs} \tag{C.13}$$

From here we can try to reformulate the previous equation with forms on M. Using local coordinates (x^0, x^1, x^2, x^3) on $N = \mathbb{R} \times M$ such that x^0 is the coordinate for $\mathbb{R}$ (i.e. time coordinate) and (x^1, x^2, x^3) are coordinates on M and using previous definitions for the forms on M and N, we can write for $i, j = 1, 2, 3$,

$$\mathcal{F}_{i0} = \mathcal{E}_i \tag{C.14}$$
$$\mathcal{F}_{ij} = \mathcal{B}_{ij} \tag{C.15}$$
$$\mathcal{G}_{i0} = -\mathcal{H}_i \tag{C.16}$$
$$\mathcal{G}_{ij} = \mathcal{D}_{ij} \tag{C.17}$$

This allows us to rewrite eq.ref. – for $i, j = 1, 2, 3$ and r, s summed over $1, 2, 3$ – as (see [Matias, 2012]),

$$\mathcal{H}_i = -\kappa^{r0}_{i0}\mathcal{E}_r - \frac{1}{2}\kappa^{rs}_{i0}\mathcal{B}_{rs} \tag{C.18}$$
$$\mathcal{D}_{ij} = \kappa^{r0}_{ij}\mathcal{E}_r + \frac{1}{2}\kappa^{rs}_{ij}\mathcal{B}_{rs} \tag{C.19}$$

This formulation highlights the coupling between electric and magnetic fields occurring through constitutive relation κ. Should κ^{r0}_{i0} and κ^{rs}_{ij} be null, the medium is anisotropic. When dealing with an isotropic non-dispersive medium, constitutive equations further simplify and are equivalent to (see [Matias, 2012]),

$$\mathcal{D} = \epsilon *_0 \mathcal{E} \tag{C.20}$$
$$\mathcal{B} = \mu *_0 \mathcal{H} \tag{C.21}$$

ϵ is the electrical permittivity and μ the magnetic permeability, they are determined by the electrical properties of the medium and magnetic properties of the medium respectively and are real value scalars. $*_0$ is the Hodge star operator induced by the Euclidian metric on $\mathbb{R}^3$. In the next section we shall work with Fourier transformed quantities on 3-manifold M. Maxwell's equations thus read,

$$dE(\omega) = i\omega B(\omega) \tag{C.22}$$
$$dH(\omega) = -i\omega D(\omega) + J(\omega) \tag{C.23}$$
$$D(\omega) = \rho(\omega) \tag{C.24}$$
$$B(\omega) = 0 \tag{C.25}$$

Similarly, constitutive relations for an isotropic non-dispersive medium remain,

$$D = \epsilon *_0 E \tag{C.26}$$
$$B = \mu *_0 H \tag{C.27}$$

C.2 HUYGENS-FRESNEL'S PRINCIPLE

We recall here Huygens-Fresnel's principle as described in [Warnick and Arnold, 1997]. We use the double form Green function $\Gamma(x;x')$ as defined in [Warnick and Arnold, 1996] for a fixed angular frequency ω,

$$E(x') = i\omega \int_\Omega \tilde{\Gamma}(x;x') \wedge J(x) + \int_{\partial\Omega} \tilde{\Gamma}(x;x') \wedge H(x) + *_h d\tilde{\Gamma}(x;x') \wedge E(x) \tag{C.28}$$

Following the discussions in section B, we can rewrite the previous expression,

$$E_s(x') = E(x') - E_i(x') \tag{C.29}$$
$$E_s(x') = \int_{\partial\Omega} \tilde{\Gamma}(x;x') \wedge H(x) + *_h d\tilde{\Gamma}(x;x') \wedge E(x) \tag{C.30}$$

We now assume E and H can be expressed locally on $\partial\Omega$ as,

$$E = r_e(E_i, H_i) \tag{C.31}$$
$$H = r_h(E_i, H_i) \tag{C.32}$$

We assume we can represent the previous mapping $\{r_e, r_h\}$ through four $\binom{1}{1}$-tensors (see equation B.31) such that $r_e = \{r_{ee}, r_{eh}\}$ and $r_h = \{r_{hh}, r_{he}\}$ – for $l = 1,2,3$ summed over $1,2,3$ and $x \in \partial\Omega$,

$$E_\alpha(x) = (r_{ee})^l_\alpha(x)\ (E_i)_l(x) + (r_{eh})^l_\alpha(x)\ (H_i)_l(x) \tag{C.33}$$
$$H_\alpha(x) = (r_{he})^l_\alpha(x)\ (E_i)_l(x) + (r_{hh})^l_\alpha(x)\ (H_i)_l(x) \tag{C.34}$$

At this point we have been able to express with a different formalism the problem discussed in this manuscript. We can now apply inverse problem equations to asses tensors $\{r_{ee}, r_{eh}\}$ and $\{r_h, r_{he}\}$ very much like we have done with vector quantities in section 5. A similar work can be conducted to recover results presented in section 4 (see [Desbrun et al., 2005]) but remains to be done.

Differential geometry is naturally adapted to describe electromagnetic fields. The elegance of the equations using this form and the geometrical interpretations – from a macroscopic point of view – are quite remarkable. Although in

the course of this three years I have mostly used vector formulations, it seems clear today that differential formulation provides a better set-up to work with. I strongly believe that an effort in formulating the problems in differential forms will eventually provide powerful tools in electromagnetism, and thus in planetary sounding radar.

J. Ackley and L. Ahern. The curse of monkey island. LucasArts, 1997.

W. Anderson. The life aquatic with steve zissou. Buena Vista Pictures, 2004.

J. L. Araque Quijano and G. Vecchi. Field and source equivalence in source reconstruction on 3D surfaces. *Progress In Electromagnetics Research*, 103:67–100, 2010.

D. Aykroyd, H. Ramis, and I. Reitman. Ghostbusters. Columbia Pictures, 1984.

C. Baudrit and D. Dubois. Practical representations of incomplete probabilistic knowledge. *Comput. Stat. Data Anal.*, 51(1):86–108, November 2006. ISSN 0167-9473.

Y. Berquin, W. Kofman, A. Herique, G. Alberti, and P. Beck. A study on ganymede's surface topography: Perspectives for radar sounding. *Planetary and Space Science*, (0), 2012.

L. Bourgeois, N. Chaulet, and H. Haddar. On simultaneous identification of a scatterer and its generalized impedance boundary condition. Rapport de recherche RR-7645, INRIA, June 2011a.

L. Bourgeois, N. Chaulet, and H. Haddar. Stable reconstruction of generalized impedance boundary conditions. *Inverse Problems*, 27(9):095002, 2011b.

A. Buffa and Ralf Hiptmair. Galerkin boundary element methods for electromagnetic scattering. In *Lect. Notes Comput. Sci. Eng.*, volume 31, pages 83–124. 2003.

B. Cecconi, S. Hess, A. HÃ©rique, M.R. Santovito, D. Santos-Costa, P. Zarka, G. Alberti, D. Blankenship, J.-L. Bougeret, L. Bruzzone, and W. Kofman. Natural radio emission of jupiter as interferences for radar investigations of the icy satellites of jupiter. *Planetary and Space Science*, 61(1):32 – 45, 2012. ISSN 0032-0633.

Y. Colin de Verdière. Les équations de maxwell. In *Séminaire de théorie spectrale et géométrie*, volume 15, pages 115–125, 1996-1997.

D. Colombo and M. De Stefano. Geophysical modeling via simultaneous joint inversion of seismic, gravity, and electromagnetic data: Application to prestack depth imaging. *The Leading Edge*, 26(3):326–331, March 2007.

I.G. Cumming and F.H.C. Wong. *Digital Processing Of Synthetic Aperture Radar Data: Algorithms And Implementation*. Artech House Remote Sensing Library. Artech House, 2005.

B. N. Delaunay. Sur la sphère vide. *Bulletin of Academy of Sciences of the USSR*, (6):793–800, 1934.

R. W. Deming and A. J. Devaney. Diffraction tomography for multi-monostatic ground penetrating radar imaging. *Inverse Problems*, 13:29–45, 1997.

A. P. Dempster. Upper and lower probabilities induced by a multivalued mapping. *Annals of Mathematical Statistics*, 38:325–339, 1967.

M. Desbrun, E. Kanso, and Y. Tong. Discrete differential forms for computational modeling. In *ACM SIGGRAPH 2005 Courses*, SIGGRAPH '05, New York, NY, USA, 2005. ACM.

G. A. Deschamps. Electromagnetics and differential forms. *Proceedings of the IEEE*, 69:676–696, 1981.

O. Dorn, Bertete-Aguirre, Berryman H., J. G., and G. C. Papanicolaou. A nonlinear inversion method for 3D electromagnetic imaging using adjoint fields. *Inverse Problems*, 15:1523–1558, 1999.

M. A. Dupertuis and M. Proctor. Generalization of complex snell-descartes and fresnel laws. *Journal of Optical Society of America*, 11:1159–1166, 1994.

W. Fa, Q. Li, and Y. Q. Jin. Simulation of radar sounder echo from lunar surface layer and detection of lunar subsurface structure. In *European Planetary Science Congress 2009*, page 12, September 2009.

A. Ferro, A. Pascal, and L. Bruzzone. A novel method for automatic clutter detection in radargrams acquired by orbiting radar sounders. In *Geoscience and Remote Sensing Symposium (IGARSS), 2012 IEEE International*, 2012.

G. Franceschetti, A. Iodice, M. Migliaccio, and D. Riccio. Scattering from natural rough surfaces modeled by fractional brownian motion two-dimensional processes. *IEEE transactions on antennas and propagation*, 47:1405–1415, 1999.

A. K. Fung and H. L. Chan. On the integral for backscattering from a randomly rough surface. *IEEE Proceedings*, 59:1280–1281, 1971.

A. K. Fung, Z. Li, and K. S. Chen. Backscattering from a randomly rough dielectric surface. *Geoscience and Remote Sensing, IEEE Transactions on*, 30(2):356–369, March 1992.

R. E. Grimm, E. Heggy, S. Clifford, C. Dinwiddie, R. McGinnis, and D. Farrell. Absorption and scattering in ground-penetrating radar: Analysis of the Bishop Tuff. *Journal of Geophysical Research (Planets)*, 111:E06S02, June 2006.

Gaël Guennebaud, Benoît Jacob, et al. Eigen v3. http://eigen.tuxfamily.org, 2010.

W. K. Hastings. Monte Carlo sampling methods using Markov chains and their applications. *Biometrika*, 57(1):97–109, April 1970. ISSN 1464-3510.

Y.-Q. Jin. Simulation of Radar Sounder Echoes and Inversion of Lunar Subsurface. *LPI Contributions*, 1685:3003, October 2012.

J.T. Katsikadelis. *Boundary Elements: Theory and Applications: Theory and Applications*. Elsevier Science, 2002. ISBN 9780080528243.

T. Kobayashi, H. Oya, and T. Ono. A-scope analysis of subsurface radar sounding of lunar mare region. *Earth, Planets, and Space*, 54:973–982, October 2002a.

T. Kobayashi, H. Oya, and T. Ono. B-scan analysis of subsurface radar sounding of lunar highland region. *Earth, Planets, and Space*, 54:983–991, October 2002b.

W. Kofman, A. Herique, J.-P. Goutail, T. Hagfors, I. P. Williams, E. Nielsen, J.-P. Barriot, Y. Barbin, C. Elachi, P. Edenhofer, A.-C. Levasseur-Regourd, D. Plettemeier, G. Picardi, R. Seu, and V. Svedhem. The Comet Nucleus Sounding Experiment by Radiowave Transmission (CONSERT): A Short Description of the Instrument and of the Commissioning Stages. *Space Sci. Rev.*, 128:413–432, February 2007.

A. Kong, J. *Electromagnetic Wave Theory*. EMW, 2000.

A. Lakhal. *Resolution of Inverse Scattering Problems for the full three-dimensional Maxwell-Equations in Inhomogeneous Media using the Approximate Inverse*. PhD thesis, Mathematischen-Naturwissenschaftlichen Fakultaten a der Universitat des Saarlandes, 2006.

A. Lang and J. Potthoff. Fast simulation of gaussian random fields. *Monte Carlo Meth. and Appl.*, 17(3):195–214, 2011.

A. Le Gall. *Sondage des sous-sols planétaires par radar à pénétration de sol: étude et modélisation des performances de l'instrument TAPIR*. PhD thesis, Université Pierre et Marie Curie, 2007.

V. Lindell, I. Electromagnetic wave equation in differential-form representation. *Progress In Electromagnetics Research*, 54, 2005.

G. Linehan. The it crowd. 2007.

LO Løseth, H. M. Pedersen, B. Ursin, L. Amundsen, and S. Ellingsrud. Low-frequency electromagnetic fields in applied geophysics: Waves or diffusion? *Geophysics*, 71(4):W29–W40, 2006.

F. D. Matias. Determination of an electromagnetic medium from the fresnel surface. *Journal of Physics A: Mathematical and Theoretical*, 45(40):405203, 2012.

M. Matsumoto and T. Nishimura. Mersenne twister: A 623-dimensionally equidistributed uniform pseudo-random number generator. *ACM Trans. Model. Comput. Simul.*, 8(1):3–30, January 1998. ISSN 1049-3301.

N. Metropolis, A. W. Rosenbluth, M. N. Rosenbluth, A. H. Teller, and E. Teller. Equation of State Calculations by Fast Computing Machines. *The Journal of Chemical Physics*, 21(6):1087–1092, 1953.

C. Monzon, J. On surface integral representations: Validity of huygens' principle and the equivalence principle in inhomogeneous bianisotropic media. *IEEE Transactions on Microwave Theory and Techniques*, 41(11):1995–2000, 1993.

J. Mouginot, W. Kofman, A. Safaeinili, and A. Herique. Correction of the ionospheric distortion on the MARSIS surface sounding echoes. *Planetary and Space Science*, 56:917–926, May 2008.

J. Mouginot, A. Pommerol, W. Kofman, P. Beck, B. Schmitt, A. Herique, C. Grima, A. Safaeinili, and J. J. Plaut. The 3-5 MHz global reflectivity map of Mars by MARSIS/Mars Express: Implications for the current inventory of subsurface H_2O. *Icarus*, 210:612–625, December 2010.

J.-F. Nouvel, A. Herique, W. Kofman, and A. Safaeinili. Radar signal simulation: Surface modeling with the Facet Method. *Radio Science*, 39:RS1013, February 2004.

D. S. Oliver. Calculation of the inverse of the covariance. *Mathematical Geology*, 30:911–933, 1998.

T. Ono and H. Oya. Lunar Radar Sounder (LRS) experiment on-board the SELENE spacecraft. *Earth, Planets, and Space*, 52:629–637, September 2000.

T. Ono, A. Kumamoto, Y. Kasahara, Y. Yamaguchi, A. Yamaji, T. Kobayashi, S. Oshigami, H. Nakagawa, Y. Goto, K. Hashimoto, Y. Omura, T. Imachi, H. Matsumoto, and H. Oya. The Lunar Radar Sounder (LRS) Onboard the KAGUYA (SELENE) Spacecraft. *Space Sci. Rev.*, 154:145–192, July 2010.

R.V. Ostrovitianov and F.A. Basalov. *Statistical theory of extended radar targets: a translation from the Russian of Statisticheskaya teoriya radiolokatsii protyazhennyz [sic] tselei.* Artech House, 1985.

G. Picardi, D. Biccari, R. Seu, L. Marinangeli, W. T. K. Johnson, R. L. Jordan, J. Plaut, A. Safaenili, D. A. Gurnett, G. G. Ori, R. Orosei, D. Calabrese, and E. Zampolini. Performance and surface scattering models for the Mars Advanced Radar for Subsurface and Ionosphere Sounding (MARSIS). *Planetary and Space Science*, 52:149–156, January 2004.

R. Pierrat. *Propagation et émission du rayonnement en milieu diffusant. Application a l'imagerie des milieux complexes.* PhD thesis, Ecole Centrale Paris, 2007.

J. J. Plaut, A. Safaeinili, J. W. Holt, R. J. Phillips, J. W. Head, R. Seu, N. E. Putzig, and A. Frigeri. Radar evidence for ice in lobate debris aprons in the mid-northern latitudes of Mars. *Geophys. Res. Lett.*, 36:L02203, January 2009.

D. Plettemeier, R. Hahnel, S. Hegler, A. Safaeinili, J. Plaut, B. Gaskell, R. Orosei, A. Cicchetti, and G. Picardi. Numerical computation of radar echoes measured by marsis during phobos flybys. In *Radar Conference, IEEE*, 2009.

R. K. Raney, H. Runge, R. Bamler, G. Cumming, I., and F. H. Wong. Precision sar processing using chirp scaling. *IEEE transactions on deoscience and remote sensing*, 32:786–799, 1994.

B D. Rigling, O. L. Moses, and Senior Member. Three-dimensional surface reconstruction from multistatic sar images. In *EURASIP Journal on Advances in Signal Processing*, pages 1159–1171, 2005.

F. Russo, M. Cutigni, R. Orosei, C. Taddei, R. Seu, D. Biccari, E. Giacomoni, O. Fuga, and E. Flamini. An incoherent simulator for the sharad experiment. In *Radar Conference, 2008 IEEE*, 2008.

L. Ryzhik, G. Papanicolaou, and J. B. Keller. Transport equations for elastic and other waves in random media. *Wave Motion*, 24:327–370, 1996.

A. Safaeinili, W. Kofman, J. Mouginot, Y. Gim, A. Herique, A. B. Ivanov, J. J. Plaut, and G. Picardi. Estimation of the total electron content of the Martian ionosphere using radar sounder surface echoes. *Geophys. Res. Lett.*, 34:L23204, December 2007.

A. Saintenoy, J.-M. Friedt, A. D. Booth, F. Tolle, E. Bernard, D. Laffly, C. Marlin, and M. Griselin. Deriving ice thickness, glacier volume and bedrock morphology of the Austre Lov\'enbreen (Svalbard) using Ground-penetrating Radar. *ArXiv e-prints*, June 2013.

A. C. Saintenoy and A. Tarantola. Ground-penetrating radar: Analysis of point diffractors for modeling and inversion. *Geophysics*, 66:540, 2001.

W. Schroeder, K. M. Martin, and W. E. Lorensen. *The visualization toolkit (2nd ed.): an object-oriented approach to 3D graphics*. Prentice-Hall, Inc., Upper Saddle River, NJ, USA, 1998.

R. Seu, D. Biccari, R. Orosei, L. V. Lorenzoni, R. J. Phillips, L. Marinangeli, G. Picardi, A. Masdea, and E. Zampolini. SHARAD: The MRO 2005 shallow radar. *Planetary and Space Science*, 52:157–166, January 2004.

R. Seu, R. J. Phillips, G. Alberti, D. Biccari, F. Bonaventura, M. Bortone, D. Calabrese, B. A. Campbell, M. Cartacci, L. M. Carter, C. Catallo, A. Croce, R. Croci, M. Cutigni, A. Di Placido, S. Dinardo, C. Federico, E. Flamini, F. Fois, A. Frigeri, O. Fuga, E. Giacomoni, Y. Gim, M. Guelfi, J. W. Holt, W. Kofman, C. J. Leuschen, L. Marinangeli, P. Marras, A. Masdea, S. Mattei, R. Mecozzi, S. M. Milkovich, A. Morlupi, J. Mouginot, R. Orosei, C. Papa, T. Paternò, P. Persi del Marmo, E. Pettinelli, G. Pica, G. Picardi, J. J. Plaut, M. Provenziani, N. E. Putzig, F. Russo, A. Safaeinili, G. Salzillo, M. R. Santovito, S. E. Smrekar, B. Tattarletti, and D. Vicari. Accumulation and Erosion of Mars' South Polar Layered Deposits. *Science*, 317:1715–, September 2007.

G. Shafer. *A mathematical theory of evidence*. Princeton university press, 1976.

S. Spielberg. Jurassic park. Universal Pictures Studio, 1993.

A. Tarantola. Theoretical background for the inversion of seismic waveforms including elasticity and attenuation. *Pure and Applied Geophysics*, 128:365–399, March 1988.

A. Tarantola. *Inverse problem theory and methods for model parameter estimation*. SIAM, 2005.

A. Tarantola and B. Valette. Generalized Nonlinear Inverse Problems Solved Using the Least Squares Criterion (Paper 1R1855). *Reviews of Geophysics and Space Physics*, 20:219, May 1982a.

A. Tarantola and B. Valette. Inverse Problems = Quest for Information. *Journal of Geophysics*, 50:159–170, 1982b.

F. L. Teixeira. Differential form approach to the analysis of the electromagnetic cloaking and masking, 2007.

J. P. Vergne. Le téléphone sonne toujours deux fois. 1985.

J. Virieux and S. Operto. An overview of full-waveform inversion in exploration geophysics. *GEOPHYSICS*, 74(6):WCC1–WCC26, November 2009.

K. F. Warnick, R. H. Selfridge, and D. V. Arnold. Teaching electromagnetic field theory using differential forms. *IEEE Trans. on Educ.*, 40(1):53–68, February 1997.

K.F. Warnick. *A Differential Forms Approach to Electromagnetics in Anisotropic Media*. Brigham Young University. Department of Electrical and Computer Engineering., 1997.

K.F. Warnick and D. Arnold. Green forms for anisotropic inhomogeneous media. *Journal of Electromagnetic Waves and Applications*, 11(8):1145–1164, 1997.

K.F. Warnick and D.V. Arnold. Electromagnetic green functions using differential forms. *Journal of Electromagnetic Waves and Applications*, 10(3):427–438, 1996.

Y. Zhang, P. Zhang, S. Cui, X. Zhang, and G. Fang. Imaging of martian surface and subsurface with high-frequency radar sounder. In *Geoscience and Remote Sensing Symposium*, 2012.

M. Zhdanov, A. Gribenko, G. Wilson, and C. Funk. 3d joint inversion of geophysical data with gramian constraints: A case study from the carrapateena iocg deposit, south australia. *The Leading Edge*, 31:1382–1388, 2012.